University of Southampton

Faculty of Environmental and Life Sciences

Ocean and Earth Science

Reconstructing Antarctic Winter Sea-ice Extent during Marine Isotope Stage 5e

by

Matthew Chadwick

ORCID ID 0000-0002-3861-4564

Thesis for the degree of Doctor of Philosophy

September 2021

University of Southampton

Abstract

Faculty of Environmental and Life Sciences

Ocean and Earth Science

Doctor of Philosophy

Reconstructing Antarctic Winter Sea-ice Extent during Marine Isotope Stage 5e

by

Matthew Chadwick

Environmental conditions during Marine Isotope Stage (MIS) 5e (130-116 ka) represent an important 'process analogue' for understanding the climatic responses to present and future anthropogenic warming. Our understanding of the response of Antarctic sea ice to global warming is particularly limited due to the short length of the observational record. Therefore, reconstructing Antarctic winter sea-ice extent (WSIE) and Southern Ocean sea-surface temperatures (SSTs) during MIS 5e provides insights into the temporal and spatial patterns of sea ice and SST change under a warmer than present climate.

This thesis presents new MIS 5e proxy records from a set of marine sediment cores located south of the Antarctic Polar Front, between 55 and 70 ^{o}S, alongside an analysis of published Southern Ocean records. The MIS 5e diatom species assemblages in these new cores are used to reconstruct and investigate changes in WSIE and SSTs between the three Southern Ocean sectors. The new proxy reconstructions of MIS 5e WSIE and SSTs are also compared to state-of-the-art climate model outputs.

There was high variability in both WSIE and SSTs in the Atlantic and Indian sectors during MIS 5e, compared to the largely stable conditions found in the Pacific sector. All three Southern Ocean sectors reached their minimum WSIE during MIS 5e concurrently, within chronological uncertainties, both with each other and with the peak atmospheric temperature in the EPICA Dome C ice core record. The high variability in the Atlantic sector records is attributed to high glacial meltwater flux into the Weddell Sea whereas the high variability in the Indian sector likely resulted from large latitudinal migrations of the Antarctic Circumpolar Current occurring on a millennial-scale. The different variability and sensitivity of Antarctic WSIE and SSTs between the three Southern Ocean sectors may have significant implications for the Southern Hemisphere climate system under future warming.

The latest climate models are currently unable to recreate the MIS 5e WSIE and SSTs seen in these new proxy records, with colder SSTs and a greater WSIE in the models than the proxy records. Inclusion of Northern Hemisphere Heinrich 11 meltwater forcing into model runs reduces the discrepancy with proxy values, but longer duration (~3-4 ka) model runs, with Heinrich 11 meltwater forcing included, are required to fully test whether state-of-the-art climate models can match Southern Ocean MIS 5e WSIE and SSTs reconstructed from proxy records.

Table of Contents

List of Accompanying Materials

Chadwick M. 2020. Southern Ocean surface sediment diatom abundances [Data set]. *Mendeley Data*. https://doi.org/10.17632/2tnxcww6c8.1

Chadwick M. 2022. Age-model tiepoints for cores DSDP 594, MD88-770, MD02-2488, MD84-551, ODP site 1094, SO136-003, PS1768-8, PS2102-2 and MD97-2120 [Data set]. *Mendeley Data*. https://doi.org/10.17632/9x86z33vzm.2

Chadwick M. & Allen C.S. 2021a. Marine Isotope Stage 5e diatom assemblages in marine sediment core ANTA91-8 (-70.78 degN, 172.83 degE, Cruise ANTA91) - VERSION 2 [Data set]. *NERC EDS UK Polar Data Centre*. https://doi.org/10.5285/BDA782A6-E89A-41A6-8791-F28001BC5D11

Chadwick M. & Allen C.S. 2021b. Marine Isotope Stage 5e diatom assemblages in marine sediment core ELT17-9 (-63.08 degN, -135.12 degE, Cruise ELT17) [Data set]. *UK Polar Data Centre, Natural Environment Research Council, UK Research & Innovation.* https://doi.org/10.5285/05DB2C67-99F0-4556-86BF-58B0E84F4CD7

Chadwick M. & Allen C.S. 2021c. Marine Isotope Stage 5e diatom assemblages in marine sediment core MD03-2603 (-64.28 degN, 139.38 degE, Cruise MD130) [Data set]. *UK Polar Data Centre, Natural Environment Research Council, UK Research & Innovation.* https://doi.org/10.5285/410F4E27-3214-466F-9DE3-E19848D8C5C2

Chadwick M. & Allen C.S. 2021d. Marine Isotope Stage 5e diatom assemblages in marine sediment core NBP9802-04 (-64.20 degN, -170.08 degE, Cruise PA9802) [Data set]. *UK Polar Data Centre, Natural Environment Research Council, UK Research & Innovation*. https://doi.org/10.5285/6106DABC-51AF-41C5-866C-CE8C9E401FD9

Chadwick M. & Allen C.S. 2021e. Marine Isotope Stage 5e diatom assemblages in marine sediment core PC509 (-68.31 degN, -86.03 degE, Cruise JR179) [Data set]. *UK Polar Data Centre, Natural Environment Research Council, UK Research & Innovation.* https://doi.org/10.5285/324137D3-CFC5-4CF6-A360-1A293A3E9ED6

Chadwick M. & Allen C.S. 2021f. Marine Isotope Stage 5e diatom assemblages in marine sediment core TPC287 (-60.31 degN, -36.65 degE, Cruise JR48) [Data set]. *UK Polar Data Centre, Natural Environment Research Council, UK Research & Innovation.* https://doi.org/10.5285/F8F7BBF7-BD86-45E5-BF22-F7FC327C94BF

Chadwick M. & Allen C.S. 2021g. Marine Isotope Stage 5e diatom assemblages in marine sediment core TPC288 (-59.14 degN, -37.96 degE, Cruise JR48) [Data set]. *UK Polar Data Centre, Natural Environment Research Council, UK Research & Innovation.* https://doi.org/10.5285/A1A6A674-823E-46F9-B345-6635A0E04220

Chadwick M. & Allen C.S. 2021h. Marine Isotope Stage 5e diatom assemblages in marine sediment core TPC290 (-55.55 degN, -45.02 degE, Cruise JR48) [Data set]. *UK Polar Data Centre, Natural Environment Research Council, UK Research & Innovation.* https://doi.org/10.5285/D7C00BEA-659A-426E-942F-821F6517C449

Chadwick M. & Allen C.S. 2021i. Marine Isotope Stage 5e diatom assemblages in marine sediment core U1361A (-64.41 degN, 143.89 degE, IODP Exp. 318) [Data set]. *UK Polar Data Centre, Natural Environment Research Council, UK Research & Innovation.* https://doi.org/10.5285/FE815073-28EE-462D-BEE3-09E0DA2F3866

Chadwick M., Allen C.S. & Crosta X. 2021. MAT estimates of MIS 5e September sea-ice concentrations and summer SSTs [Data set]. *PANGAEA*. https://doi.pangaea.de/10.1594/PANGAEA.936573

Research Thesis: Declaration of Authorship

Print name: MATTHEW CHADWICK

Title of thesis: Reconstructing Antarctic Winter Sea-ice Extent during Marine Isotope Stage 5e

I declare that this thesis and the work presented in it are my own and has been generated by me as the result of my own original research.

I confirm that:

1. This work was done wholly or mainly while in candidature for a research degree at this University;
2. Where any part of this thesis has previously been submitted for a degree or any other qualification at this University or any other institution, this has been clearly stated;
3. Where I have consulted the published work of others, this is always clearly attributed;
4. Where I have quoted from the work of others, the source is always given. With the exception of such quotations, this thesis is entirely my own work;
5. I have acknowledged all main sources of help;
6. Where the thesis is based on work done by myself jointly with others, I have made clear exactly what was done by others and what I have contributed myself;
7. Parts of this work have been published as:

Chadwick M., Allen C.S., Sime L.C. & Hillenbrand C.-D. 2020. Analysing the timing of peak warming and minimum winter sea-ice extent in the Southern Ocean during MIS 5e. *Quaternary Science Reviews*, **229:** 106134.

Chadwick M., Allen C.S., Sime L.C., Crosta X. & Hillenbrand C.-D. 2022. How does the Southern Ocean palaeoenvironment during Marine Isotope Stage 5e compare to the modern? *Marine Micropaleontology*, **170:** 102066.

Chadwick M., Allen C.S., Sime L.C., Crosta X. & Hillenbrand C.-D. 2022. Reconstructing Antarctic winter sea-ice extent during Marine Isotope Stage 5e. *Climate of the Past*, **18:** 129-146.

Chadwick M., Sime L.C., Allen C.S., Guarino M.-V. & Oliver K.I.C. 2022. Model-data comparison of Antarctic winter sea-ice extent and Southern Ocean sea-surface temperatures during Marine Isotope Stage 5e. *Earth and Planetary Science Letters*, **in review**.

Signature: .....Date:….3/3/22.....

Acknowledgements

First and foremost, I want to thank my supervisory team (Claire Allen, Louise Sime, Vittoria Guarino and Kevin Oliver) for all their support and advice, with special thanks to Claire for her continued kindness and enthusiasm throughout the last four years, as well as her extreme patience with my numerous questions and emails. I would also like to thank Xavier Crosta for providing me with the sediment samples for core MD03-2603, running the diatom transfer function on my samples, and providing valuable and constructive feedback on multiple manuscripts. I also thank Claus-Dieter Hillenbrand for his helpful comments and feedback on several of my manuscript drafts and for helping in the selection, splitting and sampling of core PC509.

I would like to thank Hilary Blagbrough, Mark Evans and Victoria Alcock for their help with lab work and core sampling at BAS, and Vittoria Guarino, Sentia Goursaud and Irene Malmierca Vallet for their help in running the HadGEM3 model simulations and accessing/formatting the data from both the HadGEM3 and HadCM3 simulations. My thanks to the British Ocean Sediment Core Research Facility (BOSCORF) for supplying the sediment samples for core TPC287, the Larmont-Doherty Earth Observatory core repository for providing the sediment samples for core NBP9802-04 (IGSN – DSR0003YW), the International Ocean Discovery Program (IODP) for providing the sample material for core U1361A, the Oregon State University Marine and Geology Repository for providing the sediment samples for core ELT17-9 and the Sorting Centre of MNA-Trieste (Italy) for providing the sediment samples for core ANTA91-8.

Last, but definitely not least, I want to thank the BAS student community (including Ali Teague), my family, friends, and Helen for all their moral support, and the regular provision of cake, throughout my PhD. As, in the words of Winnie the Pooh, “A hug is always the right size”.

Definitions and Abbreviations

AABW ..... Antarctic Bottom Water

AAIW ..... Antarctic Intermediate Water

ACC ..... Antarctic Circumpolar Current

AMOC ..... Atlantic Meridional Overturning Circulation

AP ..... Antarctic Peninsula

AS ..... Amundsen Sea

Atlantic sector ..... The Atlantic sector of the Southern Ocean between 70 ^{o}W and 20 ^{o}E

AZ ..... Antarctic Zone

BS ..... Bellingshausen Sea

CDW ..... Circumpolar Deep Water

CLIVASH-2k ..... Climate variability in Antarctica and the Southern Hemisphere in the last 2000 years

CMIP ..... Coupled Model Intercomparison Project

C-SIDE ..... Cycles of Sea-Ice Dynamics in the Earth system

CSIRO ..... Commonwealth Scientific and Industrial Research Organisation

DSDP ..... Deep Sea Drilling Program

EDC3 ..... A chronology for the EPICA Dome C ice core from East Antarctica based on snow accumulation and mechanical flow modelling with tuning from a set of independent age markers (Parrenin et al. 2007).

EPICA ..... European Project for Ice Coring in Antarctica

FCC ..... *Fragilariopsis curta* and *Fragilariopsis cylindrus*

GAM ..... Generalised Additive Method

HadCM3 ..... Hadley Centre Coupled Model version 3

HadGEM3 ..... Hadley Centre Global Environment Model version 3

HadISST1 ..... Hadley Centre Global Sea Ice and Sea Surface Temperature dataset

H11 ..... Heinrich 11

H11(1600)_HC ..... Average model output for years 1500-1600 of a HadCM3 simulation run with H11 meltwater forcing included.

H11(250)_HC ..... Average model output for years 150-250 of a HadCM3 simulation run with H11 meltwater forcing included.

H11(250)_HG ..... Average model output for years 150-250 of a HadGEM3 simulation run with H11 meltwater forcing included.

IKM..... Imbrie & Kipp Method

Indian sector ..... The Indian sector of the Southern Ocean between 20 and 150 ^{o}E

IODP ..... Integrated Ocean Drilling Program / International Ocean Discovery Program

IPCC..... Intergovernmental Panel on Climate Change

ITGC..... International Thwaites Glacier Collaboration

JFM..... January, February and March

ka ..... A thousand years ago

LCO..... Last Common Occurrence

LIG_HG ..... Model output from the standard MIS 5e HadGEM3 simulation run.

LOD ..... Last Occurrence Datum

LR04 ..... A 5.3 Ma global stack of benthic foraminifera $\delta^{18}O$ oxygen isotope records with a chronology based on tuning to an insolation forced model of global ice volume (Lisiecki & Raymo 2005).

MAT ..... Modern Analog Technique

MIS..... Marine Isotope Stage

MS..... Magnetic susceptibility

Na_{ss}..... Sea-salt sodium

NADW ..... North Atlantic Deep Water

ODP ..... Ocean Drilling Program

Pacific sector..... The Pacific sector of the Southern Ocean between 150 ^{o}E and 70 ^{o}W

PAGES ..... Past Global Changes

PF ..... Antarctic Polar Front

PFZ..... Polar Frontal Zone

PI ..... Pre-industrial

PMIP..... Paleoclimate Modelling Intercomparison Project

RMSEP ..... Root Mean Square Error of Prediction

rs. ..... Indicates the resting spores of a diatom species/genus.

sACCF ..... Southern ACC Front

SAF ..... Subantarctic Front

SAMW ..... Subantarctic Mode Water

SAZ ..... Subantarctic Zone

SBdy..... Southern boundary of the ACC

SIC ..... Sea-ice concentration

SO ..... Southern Ocean

SPECMAP..... Chronology for the marine $\delta^{18}O$ record based on tuning global planktonic foraminifera $\delta^{18}O$ records to variations in orbital obliquity and precession (Imbrie et al. 1984).

spp..... Indicates a grouping of any/all species within a diatom genus.

SSIE..... Summer sea-ice extent

SST..... Sea-surface temperature

SSST ..... Summer sea-surface temperature

STF..... Subtropical Front

$U^{K'}_{37}$ ..... Unsaturation ratio for the C_{37} alkenone.

WAIS..... West Antarctic Ice Sheet

WBD ..... Wet bulk density

WSI ..... Winter sea ice

WSIE ..... Winter sea-ice extent

$\delta^{18}O$ ..... Standard isotope notation for the difference between the $^{18}O/^{16}O$ ratio in a sample of interest, relative to an established standard.

Chapter 1 Introduction and Background

1.1 Antarctica and the Southern Ocean

In the present day, polar regions are warming twice as fast as the global average (IPCC 2019) and, due to their greater sensitivity to radiative forcing, act to amplify the impacts of warming through ocean and cryosphere feedbacks (Vaughan et al. 2013). High latitudes are, therefore, particularly important regions for studying and understanding the dynamics of global climate. The Southern Ocean (SO) comprises the southern-most basins of the Atlantic, Indian and Pacific Oceans (Figure 1.1) and is an important region for propagation of climate anomalies via the global overturning ocean circulation and the exchange of heat and carbon between ocean basins.

The principal aim of this thesis is to provide a reconstruction of the last interglacial (130-116 ka BP) as an analogue for the SO under the climate predicted for 2100. This first chapter presents an overview of the SO region, the background for the principal methodologies of this study, the broad rationale for this work and a brief description of the following thesis chapters.

1.1.1 Modern cryosphere

Antarctica and the SO are dominated by the vast extent of ice sheets and winter sea ice, both of which play a critical role in the global climate system through albedo-radiation feedbacks (Hall 2004). Antarctic land ice is dominated by the West Antarctic and East Antarctic ice sheets (~30 x 10^6 km^3) (Figure 1.1), which discharge into the SO through ice shelves and marine terminating glaciers. The West Antarctic Ice Sheet (WAIS) is expected to be particularly vulnerable to substantial ice mass loss and possible collapse under warmer climates (Pollard & DeConto 2009) due to the marine ice-sheet instability triggered by its retrograde bed slope and the large basal extent that is grounded below sea-level (Schoof 2007, Pattyn 2018, Morlighem et al. 2020). Unstable grounding line retreat is already observed in WAIS glaciers that outflow into the Amundsen Sea (Favier et al. 2014, Milillo et al. 2019). Concerns over the future stability of the WAIS and particularly the Thwaites Glacier (Scambos et al. 2017), which outflows into the Amundsen Sea, are consequently the focus of multiple recent international research collaborations (e.g. ITGC, IODP Exp. 379).

Modern Antarctic sea ice covers a large part of the SO during austral winter, with a peak extent of ~18 x 10^6 km^2 in September and a summer sea-ice extent of only ~4 x 10^6 km^2 in February-March (Parkinson 2019), largely limited to the continental embayments of the Weddell and Ross Seas (Figure 1.1). The vast extent of Antarctic winter sea ice and its large seasonal variations (~14 x 10^6 km^2) impacts on multiple processes and feedbacks within the SO. Sea ice affects oceanographic

circulation through both freezing and melting. Brine rejection during the freezing of sea ice leads to the formation of dense and bottom waters (Chapter 1.1.2) and the melting of sea ice releases freshwater which influences buoyancy fluxes and the production of mode and intermediate waters (Abernathey et al. 2016, Rintoul 2018).

Sea-ice cover also regulates heat and gas exchange between the SO and atmosphere, through both surface stratification (Goosse & Zunz 2014) and as a physical barrier (Rysgaard et al. 2011). Sea ice also acts as a physical barrier to buffer against wave action and stabilise marine terminating ice shelves from calving (Massom et al. 2018). Antarctic sea ice has multiple direct and indirect influences on the SO marine ecosystem (Massom & Stammerjohn 2010) including the high primary productivity of phytoplankton within the sea-ice meltwater zone (Kahru et al. 2016), which in turn supports higher trophic levels. There are also many species of megafauna (e.g. Emperor Penguins) that depend on sea-ice environments for their survival (Forcada & Trathan 2009).

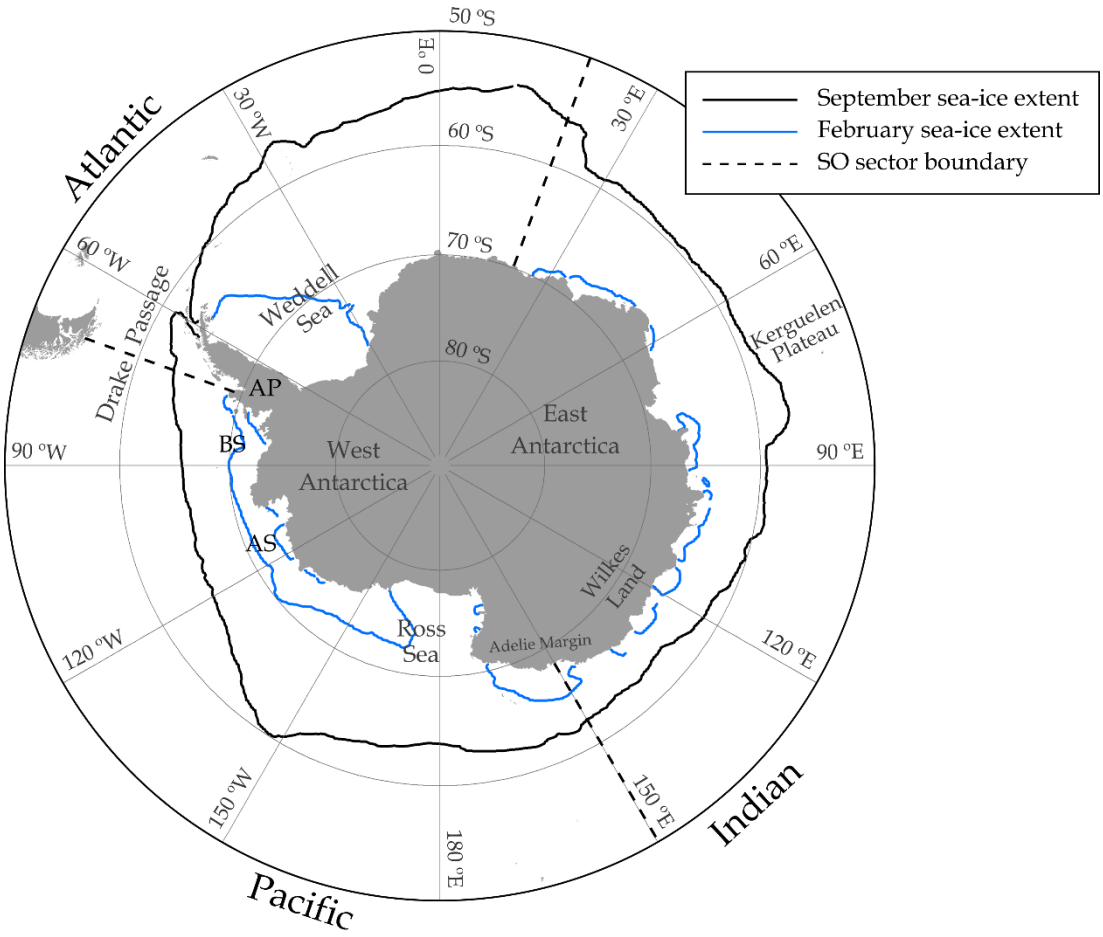

Figure 1.1 Map of Antarctica and the Southern Ocean (SO) with the mean modern (1981-2010) September (black line) and February (blue line) sea-ice extents. The boundaries of the three SO sectors (Atlantic sector: 70 °W – 20 °E; Indian sector: 20 – 150 °E; Pacific sector: 150 °E – 70 °W) are marked with black dashed lines and key regions of the map are labelled. The modern sea-ice extent data is from Fetterer et al. (2017). AP – Antarctic Peninsula; AS – Amundsen Sea; BS – Bellingshausen Sea.

1.1.2 Modern oceanography

Global oceanic circulation is driven by a combination of density gradients, winds and tides, with the density differences between water masses established by the distribution of heat and salinity (Rahmstorf 2002, Carter et al. 2008). The SO is an important region for global ocean circulation because it links the Atlantic, Indian and Pacific Ocean basins and is a source region for mode-, intermediate- and bottom-water masses (Rintoul 2018). The dominant oceanographic feature of the SO is the clockwise flowing Antarctic Circumpolar Current (ACC), which is largely driven by westerly winds and forms a continuous belt separating subtropical waters to the north from Antarctic waters to the south (Orsi et al. 1995).

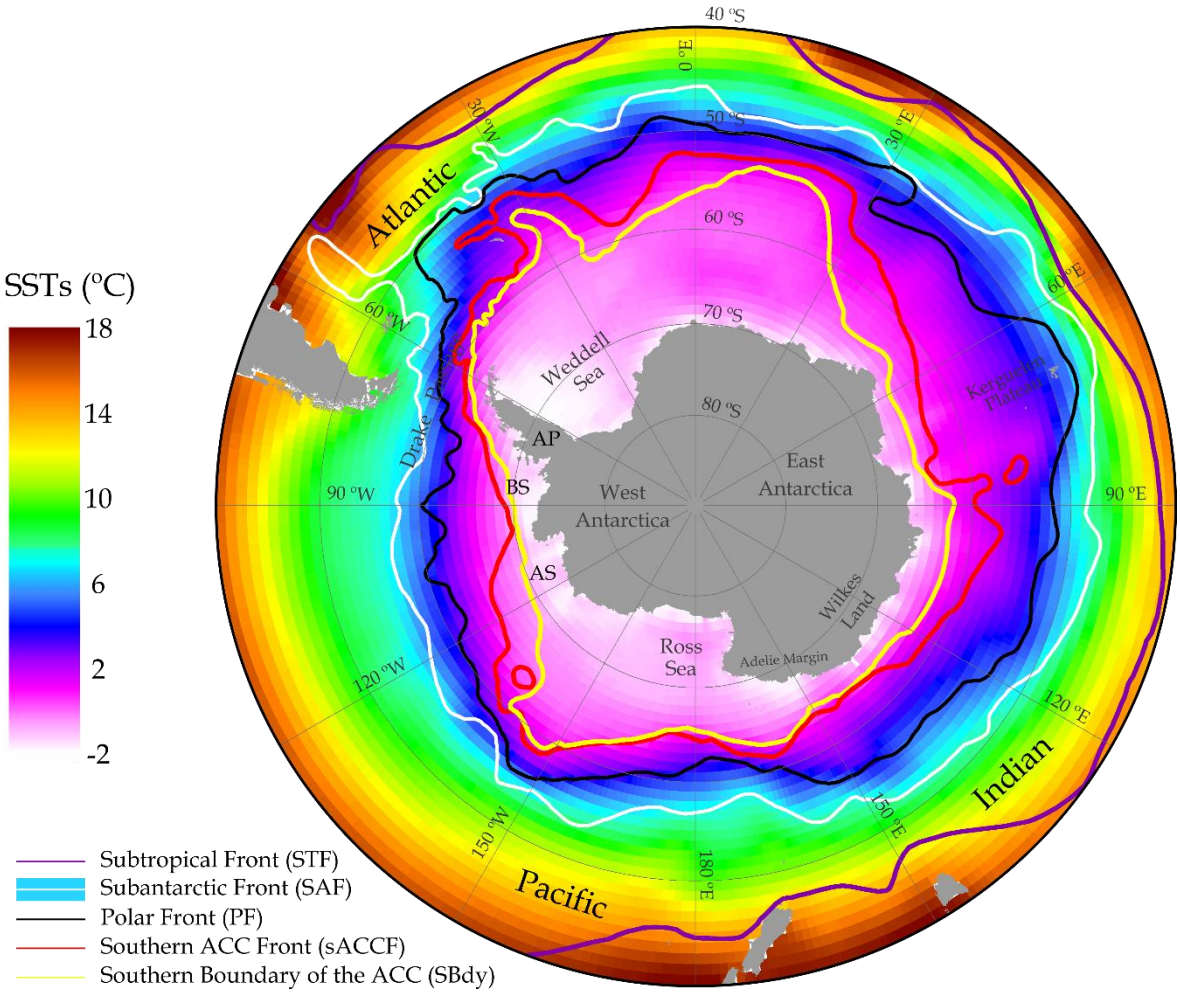

Figure 1.2 Map of modern (1981-2010) Southern Ocean mean annual SSTs (COBE-SST2 dataset provided by the NOAA PSL, Boulder, Colorado, USA (https://psl.noaa.gov/)) with the modern position of the five ACC fronts: the Subtropical Front (STF), the Subantarctic Front (SAF), the Polar Front (PF), the Southern ACC Front (sACCF) and the Southern Boundary of the ACC (SBdy). The positions of the STF, SAF, sACCF and SBdy are from Orsi et al. (1995) and the position of the PF is from Trathan et al. (2000).

The ACC is characterised by five fronts (Figure 1.2), marked by steep horizontal density gradients associated with specific sea-surface temperatures (SSTs) and salinities (Orsi et al. 1995, Dong et al. 2006, Sokolov & Rintoul 2009). These fronts, from north to south, are: the Subtropical Front (STF), the Subantarctic Front (SAF), the Polar Front (PF), the Southern ACC Front (sACCF) and the Southern Boundary of the ACC (SBdy). The modern position of fronts can be determined by a variety of methods such as longitudinal SST gradients (Moore et al. 1999, Dong et al. 2006), hydrographic sections (Orsi et al. 1995, Belkin & Gordon 1996), sea surface height (Sokolov & Rintoul 2009), or through a combination of these methods. The different methods used in these studies at different times result in frontal positions not being fully consistent, as different 'frontal filaments' may have been mapped. In some regions of the SO, bathymetric features such as the Kerguelen Plateau and Drake Passage (Figure 1.1) act to 'pin' fronts and reduce the amount of intra- and inter-annual variability in their position (Kim & Orsi 2014).

South of the SBdy there is a westward-flowing counter-current, the Antarctic Coastal Current, and the opposing Ekman transport of the ACC and Antarctic Coastal Currents produces an area of divergence around the SBdy (Figure 1.3). This divergence promotes the upwelling of Circumpolar Deep Water (CDW) and transformation into less dense surface waters (Sloyan & Rintoul 2001). CDW is the largest SO water mass and is composed of an upper and lower branch (Santoso et al. 2006). The upper branch of CDW is characterised by deep waters recirculated from the Indian and Pacific Ocean basins, whereas the lower branch of CDW is dominated by the high salinity signature of North Atlantic Deep Water (NADW) (Sloyan & Rintoul 2001). As Antarctic surface waters flow north of the PF they sink beneath warmer Subantarctic surface waters to produce Antarctic Intermediate Waters (AAIW) (Figure 1.3) which overlie the CDW (Carter et al. 2008). Further north, between the SAF and STF, winter cooling of surface waters forms Subantarctic Mode Waters (SAMW) (Rintoul et al. 2001).

Around the Antarctic continental margin, dense shelf waters and CDW transported poleward from the divergence, contribute to the production of dense Antarctic Bottom Water (AABW) and modified CDW, respectively (Orsi et al. 1999). AABW forms in multiple regions around Antarctica, resulting in a range of physical properties reflective of the source waters, and sinks beneath the upwelling CDW (Orsi et al. 1999). The circulation of AABW is strongly influenced and restricted by bathymetry, which also causes turbulent mixing with the overlying CDW (Ferrari et al. 2014).

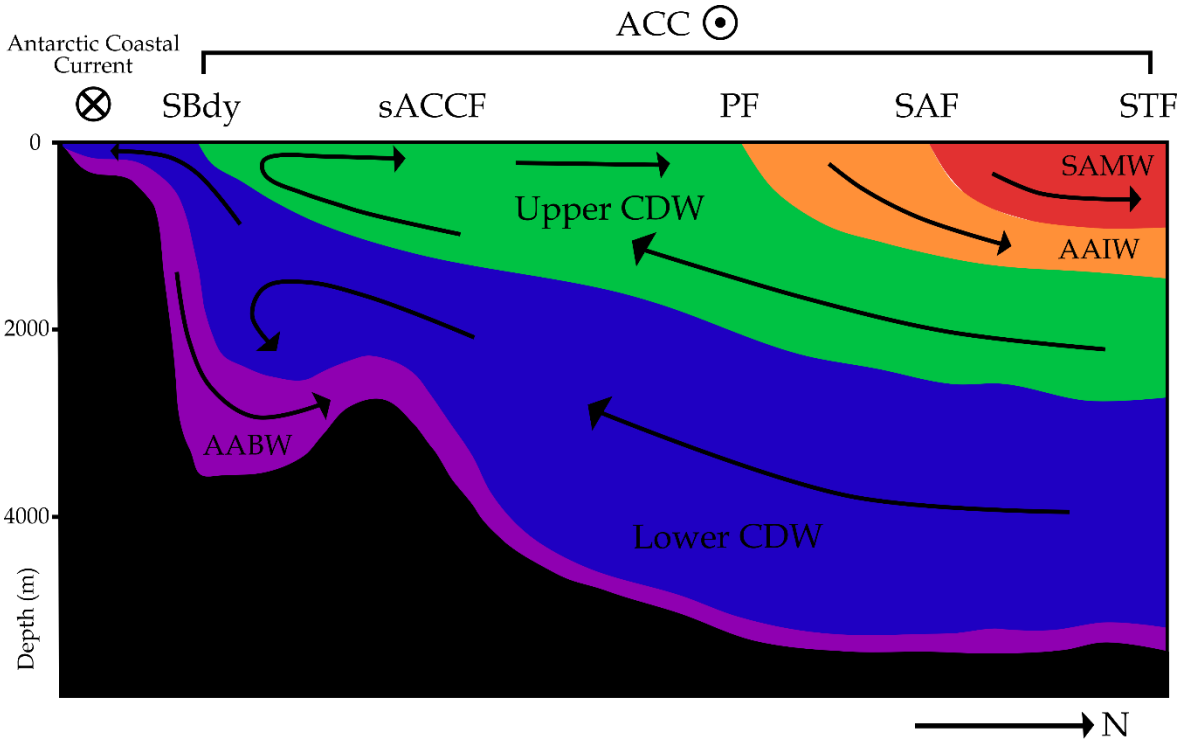

Figure 1.3 Schematic cross section of major SO water masses in the Atlantic sector (adapted from Carter et al. (2008)) and general position of ACC fronts. ACC fronts are: the Subtropical Front (STF), the Subantarctic Front (SAF), the Polar Front (PF), the Southern ACC Front (sACCF) and the Southern Boundary of the ACC (SBdy). Water masses are: Subantarctic Mode Water (SAMW), Antarctic Intermediate Water (AAIW), Upper and Lower Circumpolar Deep Water (CDW) and Antarctic Bottom Water (AABW).

1.1.3 The satellite era

Over the last 40 years, in contrast to the Arctic, there has been a slight positive trend in Antarctic sea-ice extent (Parkinson 2019). Although the overall trend since 1979 is still positive, since 2014 there has been a rapid recent decline in Antarctic sea-ice extent including two years with the lowest annual sea-ice extent in the observational record (Parkinson 2019). Within this overall trend there is substantial spatial heterogeneity, with sea-ice reductions in the Bellingshausen and Amundsen Seas concurrent with increases in the outer Weddell Sea and Ross Sea sectors (Stammerjohn et al. 2008b, King 2014, Hobbs et al. 2016). There is similar spatial heterogeneity in trends of SO surface, deep and bottom water temperatures (Maheshwari et al. 2013, Schmidtko et al. 2014) and Antarctic ice sheet mass balance, with the greatest ice mass losses from the WAIS and Antarctic Peninsula (Shepherd et al. 2018, Rignot et al. 2019). Alongside the interannual variability in Antarctic sea-ice trends (Parkinson 2019) there is also seasonal variability, with the Amundsen Sea showing a large decrease in summer and autumn sea-ice concentrations but a coinciding increase in winter and spring sea-ice concentrations (Hobbs et al. 2016). Model simulations are unable to replicate the observed sea-ice changes without an unrealistically reduced regional warming trend

(Rosenblum & Eisenman 2017). These difficulties indicate that models are not yet capable of accurately simulating the complexities of the climate dynamics which drive current SST and sea-ice extent changes in the SO (King 2014, Hobbs et al. 2016, Purich et al. 2016). Reconstructing the SO conditions during past warm periods provides the evidence against which to test our ability to understand and therefore predict the impacts of future warming.

1.2 Marine Isotope Stage (MIS) 5e

Throughout at least the last 800 ka, Earth's climate has been dominated by glacial-interglacial cycles with glacial periods marked by extensive Northern Hemisphere ice sheets and global temperatures up to 7 °C colder than present (Tierney et al. 2020). This climatic cyclicity is evident in records of atmospheric CO_2 concentrations, the oxygen isotopic composition ($\delta^{18}O$) of benthic foraminifera, which primarily responds to deep ocean temperatures and global ice volume, and reconstructed Antarctic air temperatures (Figure 1.4). The saw-tooth pattern of the records in Figure 1.4 highlights the non-linear behaviour of the Earth's climate with gradual glacial inceptions and rapid terminations. Shackleton & Opdyke (1973) defined MIS 1-22 based on the foraminifera $\delta^{18}O$ record preserved in marine sediments, with odd numbered stages representing interglacial periods and even numbers representing glacial periods. Marine isotope stages can be further divided into substages using the nomenclature of Railsback et al. (2015). Within the last 800 ka there are three interglacial substages with exceptionally warm air and sea SSTs – MIS 5e, 9e and 11c (Berger et al. 2016), of which MIS 5e is the most recent.

Studying past warm periods can help guide our understanding of the impact of predicted future climate change. MIS 5e (130-116 ka (Lisiecki & Raymo 2005)) marks the peak of the last interglacial when SSTs and global mean annual atmospheric temperatures peaked at around 0.8 °C warmer than present (Otto-Bliesner et al. 2013, Capron et al. 2014, Fischer et al. 2018) and global sea levels were ~6-9 m higher than now (Kopp et al. 2009, Dutton et al. 2015). Proxy reconstructions of mean annual SSTs in middle to low latitudes (between 51 °S and 51 °N) peaked at just 0.5 ± 0.3 °C warmer than pre-industrial (PI) during MIS 5e (Hoffman et al. 2017), whereas model results suggest that summer SSTs in the SO peaked at 1.8 ± 0.8 °C warmer than PI (Capron et al. 2017), indicating strong polar amplification during MIS 5e. However, unlike future anthropogenic warming caused by rising greenhouse gas concentrations, MIS 5e peak temperatures were driven primarily by orbital forcing (Yin & Berger 2015), with atmospheric CO_2 concentrations of ~280 ppm (equivalent to PI) during MIS 5e (Bereiter et al. 2015) compared with the ~400-900 ppm predicted by 2100 (IPCC 2014). Given the different forcing mechanism, MIS 5e cannot be considered a 'direct' or 'true' analogue for anthropogenic warming but is still an important 'process analogue' for investigating and

understanding the climatic mechanisms and natural feedbacks likely to be active under future warmer conditions (Stone et al. 2016).

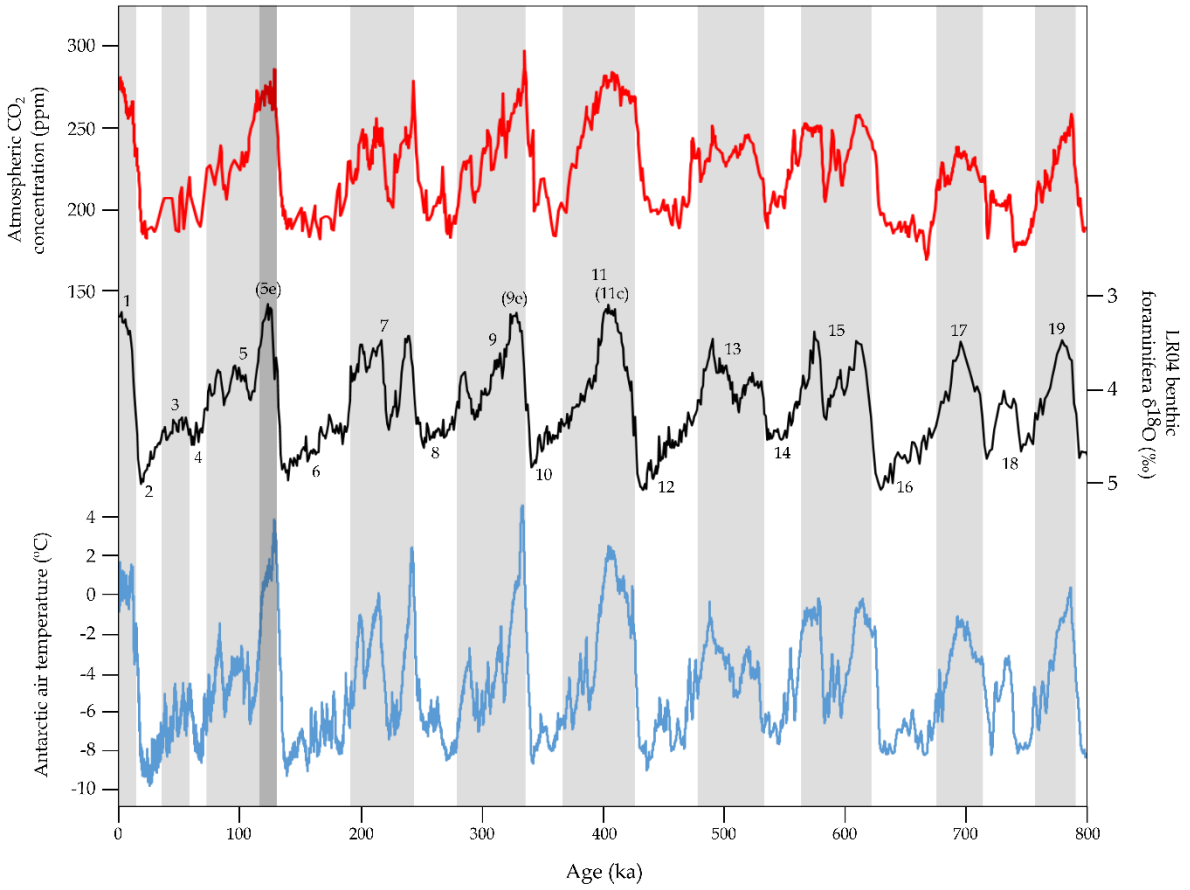

Figure 1.4 Glacial-interglacial cyclicity throughout the last 800 ka in the atmospheric CO_2 concentrations from the EPICA Dome C Antarctic ice core (red line) (Bazin et al. 2013a), the LR04 benthic foraminifera $\delta^{18}O$ record (black line) (Lisiecki & Raymo 2005) and the reconstructed Antarctic air temperatures from five Antarctic ice cores (blue line) (Parrenin et al. 2013a). MIS stages are numbered on the LR04 benthic stack with the three exceptionally warm interglacial substages (5e, 9e and 11c) also marked. Odd numbered MIS stages (interglacials) are indicated by grey shading with MIS 5e marked as a darker shading.

1.3 Diatom proxy

Diatoms are a group of phototrophic algae which are prevalent in the upper water column of the SO. Diatoms preserved in marine sediments have been used for over 40 years as a way of reconstructing past changes in Antarctic sea-ice extent and SSTs (Armand & Leventer 2010, Thomas et al. 2019) due to the close relationship between their distribution patterns and the surface water environmental conditions (Zielinski & Gersonde 1997, Armand et al. 2005, Crosta et al. 2005, Romero et al. 2005, Esper et al. 2010). Diatom distribution in the SO is primarily driven by the availability of light and nutrients (Deppeler & Davidson 2017), with iron and silica considered to be the main limiting nutrients (Boyd et al. 2001, Hiscock et al. 2003). Both light and nutrient supply to

the SO vary seasonally and thus produce a seasonal response in diatom abundance with the largest blooms during the austral spring (Abbott et al. 2000, Hiscock et al. 2003). This is particularly true for the marginal ice zone where spring melt back of the winter sea ice produces a buoyant, nutrient rich surface layer ideal for diatom growth (Figure 1.5; Taylor et al. (2013)).

Early works used surface sediment lithology to map the winter sea-ice extent (WSIE), with diatom oozes to the north of the modern sea-ice edge and pelagic clays and diatomaceous muds under sea-ice covered water (DeFelice 1979b, Burckle et al. 1982). Using these surface lithofacies as a guide, past large scale sea-ice changes (e.g. glacial-interglacial cycles) were identified in the sediment record (DeFelice 1979a). The lithological approach was further developed by relating the biogenic opal content of the sediment to WSIE under the assumption that the bulk of sediment-forming diatoms live in open ocean conditions between the winter sea-ice edge and the SAF (Burckle & Cirilli 1987, Burckle & Mortlock 1998). The strong anti-coherence between biogenic opal content in modern sediments and the overlying annual average sea-ice concentration can be extended back through the sediment record (Burckle & Mortlock 1998). However, sea-ice concentrations reconstructed in this way have a sizable error of ~30 % (Burckle & Mortlock 1998) and have the further limitation that low biogenic opal content could be due to temperature and nutrient constraints on diatom productivity, unrelated to sea-ice cover (Neori & Holm-Hansen 1982, Chase et al. 2015).

Diatom species assemblages (Figures 1.5 & 1.6) preserved in marine sediments provide a more precise method for reconstructing past sea-ice extent and duration. Almost two thirds of the biota in modern sea ice are diatoms (Garrison et al. 1986) but many of these species are too weakly silicified to be preserved in the sediment (Leventer 1998). However, Gersonde & Zielinski (2000) analysed the transfer of the more robustly silicified sea-ice diatoms *Fragilariopsis curta* and *F. cylindrus* (FCC) (Figure 1.6) from the water column to surface sediments to determine a qualitative measure of past WSIE and summer sea-ice extent (SSIE). They showed that a combined FCC relative abundances >3 % in marine sediments is a qualitative threshold for the mean WSIE (Gersonde & Zielinski 2000, Gersonde et al. 2003), with a mean sea-ice concentration of 50-80 % (Gersonde et al. 2005). A FCC threshold of >1 % is considered to mark the maximum WSIE (mean sea-ice concentration <20 %) (Gersonde et al. 2003, Gersonde et al. 2005). Reconstructions of SSIE are limited by the low biogenic opal export, poor preservation and high opal dissolution in regions covered by sea-ice for long periods of the year (Gersonde & Zielinski 2000). However, the cold water species (summer SSTs <-1 ^{o}C) *F. obliquecostata* is associated with perennial sea ice and is robustly silicified enough to be preserved in marine sediments (Zielinski & Gersonde 1997, Gersonde & Zielinski 2000). Similar to the FCC proxy, a *F. obliquecostata* relative abundance threshold >3 % is an indicator of the mean SSIE (Gersonde & Zielinski 2000).

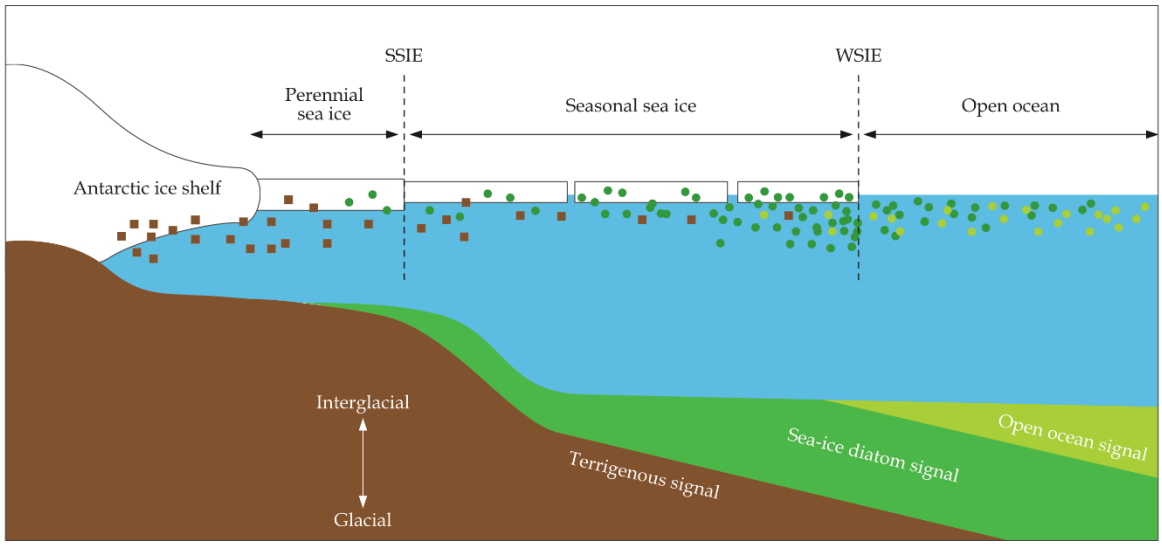

Figure 1.5 Schematic cross section indicating the varying abundance of terrigenous material, sea-ice diatoms and open ocean diatoms in the SO, relative to sea-ice cover. The downcore variation in the dominant signal is shown for a glacial to interglacial transition.

The FCC proxy cannot be applied to poorly preserved sediments where selective dissolution could alter the relative abundances, with the small size of *F. cylindrus* valves making it particularly susceptible to preferential dissolution. Warnock et al. (2015) showed that the expansion and conjoining of areolae in valves of *F. kerguelensis* (Figure 1.6), a dominant species in Pleistocene to modern SO diatom assemblages, could be used as a measure of dissolution. This allows for sediment samples with high dissolution to be identified and either discarded from analyses or treated with caution when used to make environmental inferences. Furthermore, because the FCC signal preserved in sediments is produced during the spring/summer melt back of winter sea ice, it cannot be used as a measure of sea-ice duration (e.g. months per year).

Multiple studies have used inverse statistical models to reconstruct quantitative estimates of both past sea-ice concentration and duration through diatom assemblage transfer functions (Crosta et al. 1998, Esper & Gersonde 2014a, Ferry et al. 2015b), with the most popular models being the Imbrie and Kipp Method (IKM) (Imbrie & Kipp 1971) and the Modern Analog Technique (MAT) (Hutson 1980). The IKM is an application of principal component analysis whereby the modern diatom species matrix from surface sediments is condensed down onto a few principal components which are then used to produce a multiple linear regression comparing diatom assemblages to sea-ice parameters (Esper & Gersonde 2014a, Ferry et al. 2015b). This regression can then be applied to fossil diatom assemblages to extract past sea-ice conditions (Esper & Gersonde 2014a). The MAT compares a fossil diatom assemblage to a calibration dataset of modern surface sediment assemblages and selects the modern samples that are most similar to the fossil sample (Crosta et al. 1998). The sea-ice conditions for these modern analogs are averaged to produce an estimate of

the past sea-ice conditions when the fossil sample was deposited. Ferry et al. (2015b) present a different statistical technique, the Generalised Additive Model (GAM), which only uses diatom species with a statistically significant association, and established ecological link, to sea-ice conditions. The GAM also uses a smoothed function, rather than the linear approach of the IKM, as a predictor, which is beneficial given the dominance of bimodal and monotonic responses of diatom species abundance to winter sea-ice concentration (Ferry et al. 2015b).

The MAT is limited by its requirement for large modern reference datasets and non-analog conditions where the abundances of taxa in fossil samples exceed their abundances in modern surface sediments or where extinct taxa dominate the fossil assemblage (Esper & Gersonde 2014a). Spatial autocorrelation can also bias the sea-ice reconstructions from the MAT (Guiot & de Vernal 2011). However, unlike the IKM or the GAM, the MAT can be directly applied to past diatom assemblages without smoothing data through multiple regression or principal component analysis (Crosta et al. 1998).

As with the FCC proxy, all three statistical transfer functions rely on good preservation of the fossil diatom assemblages and the assumption that the ecology of SO diatom species was the same in the past as it is in the present. All the diatom proxies discussed here are calibrated against modern surface sediments which are assumed to directly reflect the sea-ice conditions at the SO surface. Diatom sinking speeds and average rates of deep sea sedimentation indicate that the surface sediment is likely an integrated signal of up to 500 years (Miklasz & Denny 2010) but biased towards the present. The lateral transport of diatoms between the upper water column and deposition in the sediment can also bias palaeoenvironmental reconstructions, as can be seen in sediment cores from the Amundsen Sea where the preserved diatom assemblages are indicative of more northerly environmental conditions (Konfirst et al. 2012). Dominance of robustly silicified diatom species and a high degree of valve fragmentation likely indicate a more allochtonous assemblage (Beyens & Denys 1982). The mixture of coarse and finely silicified species present in a preserved assemblage, alongside the degree of dissolution and fragmentation should therefore be carefully considered before the application of a statistical transfer function (Zielinski 1993, Warnock et al. 2015, Benz et al. 2016).

Figure 1.6 (next page) Light microscope images of the key diatom species/genera referred to throughout the thesis. *Actinocyclus actinochilus* (**A**), *Azpeitia tabularis* (**B**), *Chaetoceros* resting spores (**C**, **D**), *Eucampia antarctica* cold variety (**I –** terminal valve, **K** – intercalary valve), *Fragilariopsis curta* (**G**, **R**), *Fragilariopsis cylindrus* (**E**, **F**, **H**), *Fragilariopsis kerguelensis* (**J**, **L**), *Rhizosolenia antennata* f. *semispina* (**N**, **Q**), *Thalassiosira lentiginosa* (**P**) and *Thalassiothrix* spp. (**O**).

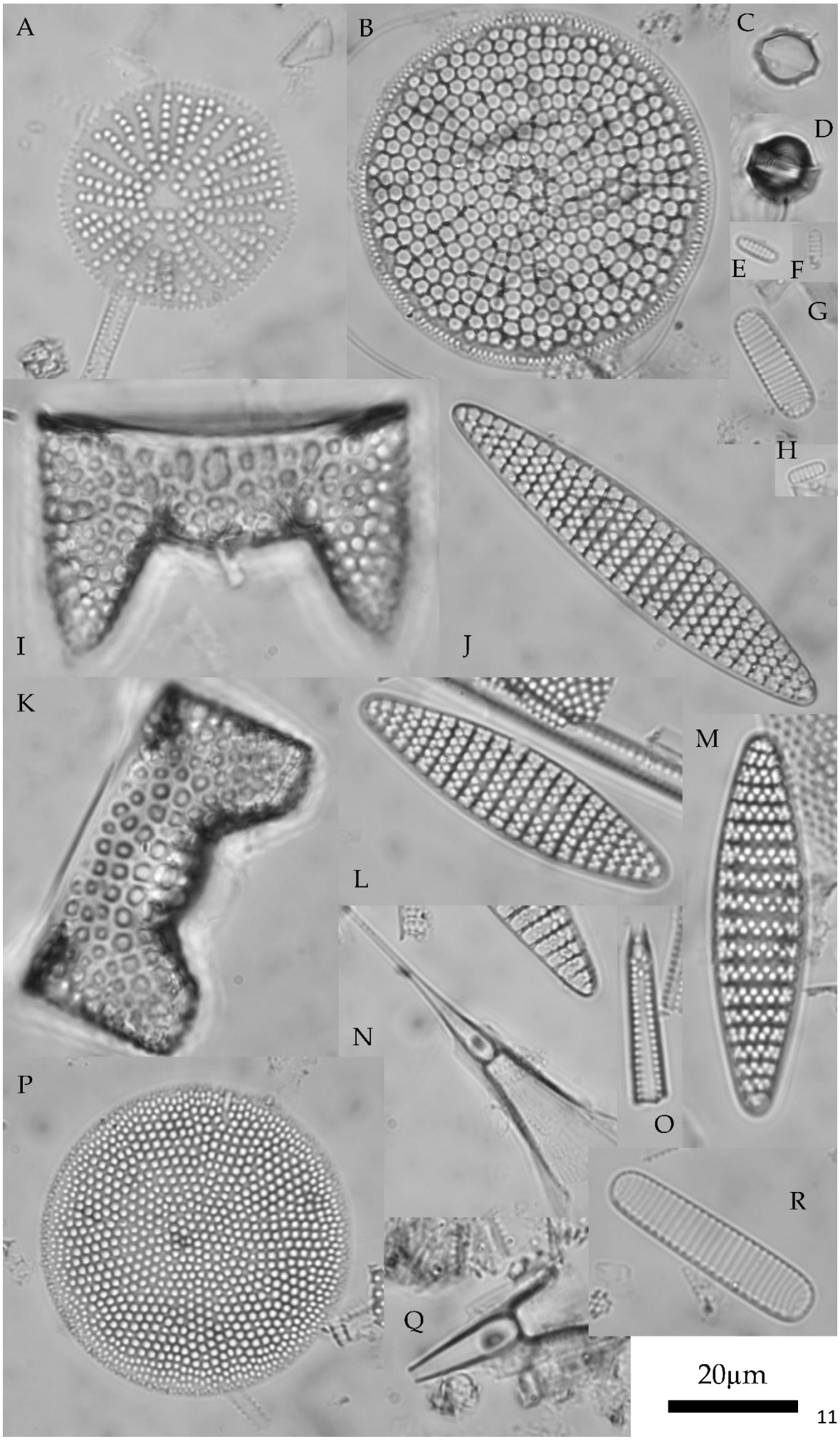
A
B
C
D
E
F
G
H
I
J
K
L
M
N
O
P
Q
R
20µm

1.4 Previous work

Previous studies of Antarctic and SO climate during MIS 5e have focused on model simulations, some with the addition of a limited number of Antarctic ice core and marine sediment proxy records (Otto-Bliesner et al. 2013, Bakker et al. 2014, Capron et al. 2014, Holloway et al. 2016, Stone et al. 2016, Capron et al. 2017, Holloway et al. 2017, Holloway et al. 2018). These studies contain few (Capron et al. 2014, Holloway et al. 2017), or no (Turney & Jones 2010, Hoffman et al. 2017, Turney et al. 2020b), marine records south of 55 ^{o}S and are therefore unable to capture the MIS 5e environmental conditions in the Antarctic Zone (south of the PF). WSIE during MIS 5e was estimated to be roughly half its current extent from model-data comparisons of the stable water isotopes in Antarctic ice cores (Holloway et al. 2016, Holloway et al. 2017) but there are almost no published MIS 5e sea-ice records from marine sediment cores located south of the modern mean WSIE (see Chapter 2). More southerly marine sediment records are therefore clearly required to better constrain the WSIE during MIS 5e or corroborate model simulations.

Due to the uncertainties in the chronologies of SO proxy records (Govin et al. 2015), previous studies have either averaged SSTs across MIS 5e (Cortese et al. 2013, Turney et al. 2020b) or assumed that peak SSTs in the SO and peak atmospheric temperatures in Antarctic ice cores occurred synchronously (Otto-Bliesner et al. 2013, Capron et al. 2014, Hoffman et al. 2017). The minimum WSIE during MIS 5e is also assumed to be synchronous throughout the SO and coeval with the 128 ka peak in Antarctic atmospheric temperatures recorded in ice cores (Holloway et al. 2017). Given the high spatial and temporal heterogeneity in both SSTs and WSIE trends in the modern SO (Chapter 1.1.3) this assumed synchronicity should be examined with care.

1.5 Thesis outline

The main aims of this thesis are:

- To reconstruct the SO palaeoenvironment during MIS 5e.
- To investigate the spatial and temporal patterns of SST and WSIE variations during MIS 5e.
- To compare model and proxy reconstructions of MIS 5e WSIE.

To address these aims the remainder of the thesis is divided up into the following 5 chapters:

Chapter 2 presents a synthesis of all published SO (south of 40 ^{o}S) marine sediment records of SSTs and FCC abundances during MIS 5e. All records are aligned onto the same chronology in order to compare timings between cores and SO sectors. The timings of MIS 5e peak SSTs and minimum WSIE are compared between SO sectors and the SSTs are used to reconstruct the positions of ACC

fronts during MIS 5e. SSTs, WSIE and ACC frontal positions during MIS 5e are discussed in the wider context of the SO palaeoenvironment.

Chapter 3 presents new MIS 5e diatom species assemblages from a series of SO marine sediment cores and compares them with the modern diatom assemblages in surface sediments. This comparison focuses on several key diatom species/genera and the palaeoenvironmental implications of their relative abundances during MIS 5e. Differences between the MIS 5e conditions in the three SO sectors are considered alongside the evidence for variations in glacial meltwater and iceberg fluxes.

Chapter 4 focuses on the diatom proxy reconstructions of SO WSIE during MIS 5e. New FCC abundances and MAT transfer function results are presented for a series of SO marine sediment cores. Results from the two proxy techniques are compared and used in collaboration to interrogate changes in WSIE between SO sectors throughout MIS 5e. SST reconstructions using the MAT are also presented for MIS 5e and compared with the timings of WSIE variations.

Chapter 5 compares the MAT transfer function data from the previous chapter to the latest HadGEM3 and HadCM3 model simulations for MIS 5e. Model simulation results are presented for both a standard MIS 5e run and runs with enhanced North Atlantic Heinrich 11 meltwater forcing included. Both SST and winter sea-ice concentration proxy data is compared with the model simulations for MIS 5e.

Chapter 6 is the concluding chapter and draws together the findings of the four previous data chapters. A synthesis of the spatial and temporal variations in MIS 5e WSIE is presented alongside a discussion of future work that would complement and develop these findings.

Chapter 2 Analysing the Timing of Peak Warming and Minimum Winter Sea-ice Extent in the Southern Ocean during MIS 5e

2.1 Introduction

The work presented in this chapter is published in: Chadwick M., Allen C.S., Sime L.C. & Hillenbrand C.-D. 2020. Analysing the timing of peak warming and minimum winter sea-ice extent in the Southern Ocean during MIS 5e. *Quaternary Science Reviews*, **229:** 106134.

In this chapter I have compiled published data for MIS 5e sea-surface temperatures (SSTs) and winter sea-ice extent (WSIE) from marine sediment cores records distributed between 40 ^{o}S and 65 ^{o}S. This compilation is used to investigate whether the timing of peak SSTs, and the minimum WSIE (simply referred to as the "sea-ice minimum" in this chapter), occurs synchronously throughout the Southern Ocean (SO), and within the three SO sectors, during MIS 5e. The SSTs are also used as a basis to reconstruct the positions of the main Antarctic Circumpolar Current (ACC) fronts during the period of peak MIS 5e warmth.

Specifically, I aim to determine whether:

- Peak SSTs during MIS 5e occur at the same time in each SO sector and coincide with the peak warming in Antarctic ice cores.
- Peak SSTs are coincident with minimum WSIE during MIS 5e.
- An increase in Southern Hemisphere July insolation during MIS 5e accounts for the SST warming and reduction in WSIE.

2.2 Modern oceanography

As discussed in Chapter 1.1.2, the oceanography of the SO is dominated by the ACC, which is made up of five fronts. For this chapter I will focus only on the fronts that separate distinct surface water masses: the Subtropical Front (STF), the Subantarctic Front (SAF) and the Polar Front (PF). In the modern SO the position of these fronts can be determined using a variety of methods (e.g. longitudinal SST gradients, hydrographic sections, sea surface height) (Orsi et al. 1995, Moore et al. 1999, Dong et al. 2006, Sokolov & Rintoul 2009), but during MIS 5e, only SSTs are available to identify the ACC front locations.

The most northerly front is the STF, which marks the northern boundary of both the ACC and Subantarctic surface waters. The STF is marked by surface water changes of 4-5 °C across the front with waters to the north generally being warmer than 14 °C (Sikes et al. 2002). The modern STF is located at ~41 °S in the Atlantic and Indian sectors of the SO and on average at 39 °S in the Pacific sector (Figure 2.1). To the south of the STF is the SAF, which is marked by SSTs greater than ~6-8 °C (Meinen et al. 2003). The SAF is currently located at an average latitude of 45 °S, 48 °C and 57 °S in the Atlantic, Indian and Pacific sectors, respectively (Figure 2.1). The most southerly ACC front considered in this chapter is the PF, which, in general corresponds to SSTs of ~2-3 °C (Dong et al. 2006). The PF is currently located at ~50 °S in the Atlantic sector, ~55 °S at 100 °E in the Indian sector and ~60 °S at 170 °W in the Pacific sector (Figure 2.1). The region south of the PF is called the Antarctic Zone, the region between the PF and SAF is the Polar Frontal Zone, and the region between the SAF and STF is the Subantarctic Zone (Orsi et al. 1995).

2.3 Core sites

This chapter presents 32 published records from 28 sediment cores across the SO (Figure 2.1) with 17 records providing ages for MIS 5e peak summer SSTs and 15 records providing ages for peak annual SSTs (Table 2.1). All SO marine sediment cores south of 40 °S, for which both a chronology and SST are published (as of January 2020), are included, with some records having been included in multiple previous publications, e.g. when various SST proxies were analysed on the same core, such as ODP Leg 177 Site 1094 (Bianchi & Gersonde 2002, Hayes et al. 2014). For each site, the MIS 5e summer and annual SSTs (jointly referred to as SSTs in this chapter, c.f. Waelbroeck et al. (2009)) are compared with corresponding modern summer or annual SSTs so that MIS 5e SST anomalies are standardised across all records. Of the 28 core sites, 10 are located in the Atlantic sector, 7 in the Indian sector and 11 in the Pacific sector (Figure 2.1). There are 11 published MIS 5e sea-ice records from 10 of the 28 sediment cores (Figure 2.1b). The methods for reconstructing past SSTs and establishing age models vary between cores (Table 2.1) but the sea-ice minimum consistently utilises the Gersonde & Zielinski (2000) FCC proxy for the presence of winter sea ice (detailed in Chapter 1.3). Accordingly, the age of the MIS 5e sea-ice minimum is reported here as the interval when the FCC abundance reached its minimum. Several of the core sites also have published transfer function estimates of MIS 5e sea ice, but to ensure consistent comparison only the FCC records are considered in this chapter. Table 2.1 contains the details for each of the studied cores, with geographical location, modern SST, sea-ice concentration, and core location in respect to frontal positions, as well as the methodological details for the age models and proxies used for the MIS 5e SST reconstructions, including the data source references. Sample resolution for the interval spanning MIS 5e is also given.

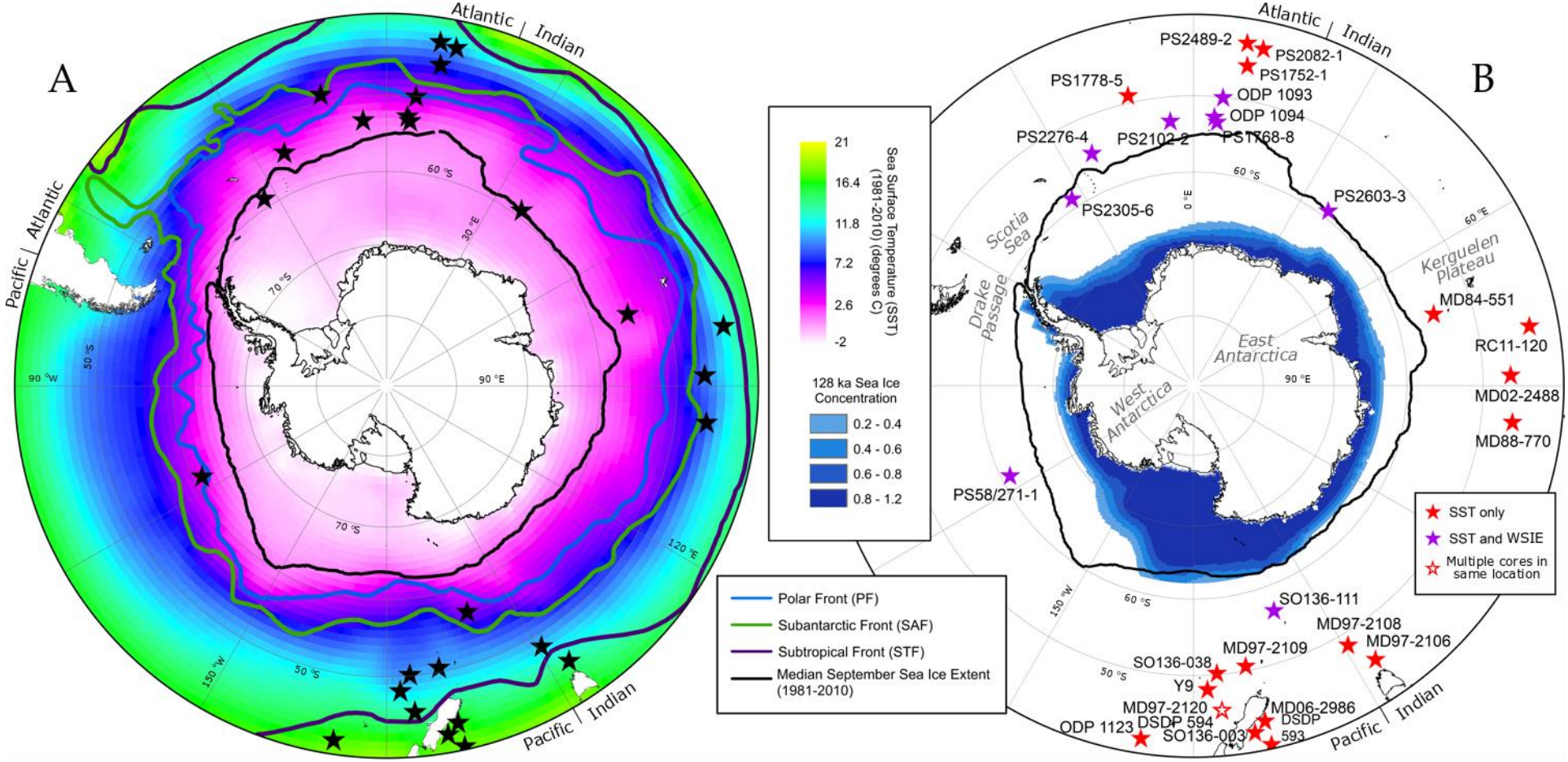

Figure 2.1 **A:** Map of modern (1981-2010) mean annual SSTs and median September sea-ice extent with Antarctic frontal positions. Black stars mark the positions of published core records used in this study. The positions of the STF and SAF are from Orsi et al. (1995) and that of the PF is from Trathan et al. (2000) **B:** Map comparing modern median September sea-ice extent with modelled September sea-ice concentrations for 128 ka (Holloway et al. 2017). The core sites marked by red stars have published SSTs only, the sites marked by purple stars have published SSTs and sea-ice records. The red star with a white centre marks the position of neighbouring cores sites MD97-2120 and DSDP Site 594.

Core	Latitude (°S), Longitude (°E)	Oceanographic position	Modern SST (°C) (*summer SST)	Modern sea ice	Chronology for MIS 5e	SST proxy for MIS 5e	Sample resolution (ka)
Atlantic sector							
PS2489-2	42.87, 8.97	SAZ	10* (Becquey & Gersonde 2003)	1	SPECMAP ages (Becquey & Gersonde 2003) converted onto LR04	Planktonic foraminifera transfer function (Becquey & Gersonde 2003)	1.2-3
PS2082-1	43.22, 11.74	SAZ	11.08* (Waelbroeck et al. 2009)	1	SPECMAP ages (Brathauer & Abelmann 1999) converted onto LR04	Radiolarian transfer function (Brathauer 1996)	5
PS1752-1	45.62, 9.60	SAZ	8* (Brathauer 1996)	1	*C. davisiana* stratigraphy (Brathauer 1996) converted onto LR04	Radiolarian transfer function (Brathauer 1996)	10-22
PS1778-5	49.01, -12.70	PFZ	4.38* (Waelbroeck et al. 2009)	1	SPECMAP ages (Brathauer & Abelmann 1999) converted onto LR04	Radiolarian transfer function (Brathauer & Abelmann 1999)	1.2-5
ODP 1093	49.98, 5.87	AZ	3.6* (Schneider Mor et al. 2012)	1	EDC3 ages (Schneider Mor et al. 2012) converted onto LR04	Diatom transfer function (Schneider Mor et al. 2012)	1
PS1768-8	52.59, 4.48	AZ	2.5* (Waelbroeck et al. 2009)	1	Correlating planktonic (*N. pachyderma*$_{(sin)}$) $\delta^{18}O$ (Mulitza et al. 1999) with LR04 (this study)	Diatom transfer function (Zielinski et al. 1998)	1-4
PS2102-2	53.07, -4.99	AZ	2.84* (Waelbroeck et al. 2009)	1	Correlating planktonic (*N. pachyderma*$_{(sin)}$) $\delta^{18}O$ (Niebler 1995) with LR04 (this study)	Diatom transfer function (Bianchi & Gersonde 2002)	0.6-3
ODP 1094	53.18, 5.13	AZ	2.2* (Capron et al. 2014)	2	EDC3 ages (Schneider Mor et al. 2012) converted onto LR04	Diatom transfer function (Bianchi & Gersonde 2002, Schneider Mor et al. 2012)	0.07-1.4 1

Core	Latitude (°S), Longitude (°E)	Oceanographic position	Modern SST (°C) (*summer SST)	Modern sea ice	Chronology for MIS 5e	SST proxy for MIS 5e	Sample resolution (ka)
					Correlating planktonic (*N. pachyderma*$_{(sin)}$) $\delta^{18}O$ (Kanfoush et al. 2002) with LR04 (this study)		
PS2276-4	54.64, -23.57	AZ	1.71* (Waelbroeck et al. 2009)	3	Diatom biofluctuation zones (Bianchi & Gersonde 2002)	Diatom transfer function (Bianchi & Gersonde 2002)	0.8-1.6
PS2305-6	58.72, -33.04	AZ	0.78* (Waelbroeck et al. 2009)	3	Diatom biofluctuation zones (Bianchi & Gersonde 2002)	Diatom transfer function (Bianchi & Gersonde 2002)	0.5-4.1
Indian sector							
RC11-120	43.52, 79.87	SAZ	11.43* (Waelbroeck et al. 2009)	1	SPECMAP ages (Martinson et al. 1987) converted onto LR04	Radiolarian transfer function (Hays et al. 1976)	1.3-2.5
MD97-2106	45.15, 146.29	N of STF	12.58 (Cortese et al. 2013)	1	Correlating benthic $\delta^{18}O$ with LR04 (Cortese et al. 2013)	Planktonic foraminifera transfer function (Cortese et al. 2013)	1.2-1.6
MD88-770	46.02, 96.45	SAZ	8.1* (Govin et al. 2009)	1	Correlating benthic (*C. wuellerstorfi, M. barleeanum* & *E. exigua*) $\delta^{18}O$ (Labeyrie et al. 1996) with LR04 (this study)	Planktonic foraminifera transfer function (Barrows et al. 2007)	0.1-0.5
MD02-2488	46.48, 88.02	SAZ	9.1* (Govin et al. 2009)	1	Correlating benthic (*C. kullenbergi*) $\delta^{18}O$ (Govin et al. 2009) with LR04 (this study)	Planktonic foraminifera transfer function (Govin et al. 2009)	1-2

Core	Latitude (°S), Longitude (°N)	Oceanographic position	Modern SST (°C) (*summer SST)	Modern sea ice	Chronology for MIS 5e	SST proxy for MIS 5e	Sample resolution (ka)
MD97-2108	48.5, 149.11	SAZ	9.49 (Cortese et al. 2013)	1	Correlating benthic $\delta^{18}O$ with LR04 (Cortese et al. 2013)	Planktonic foraminifera transfer function (Cortese et al. 2013)	2.8-2.9
MD84-551	55, 73.33	AZ	2.49* (Waelbroeck et al. 2009)	1	Correlating planktonic (*N. pachyderma$_{(sin)}$*) $\delta^{18}O$ (Pichon et al. 1992) with LR04 (this study)	Diatom transfer function (Pichon et al. 1992)	0.3-0.7
PS2603-3	58.99, 37.63	AZ	1.82* (Waelbroeck et al. 2009)	2	Diatom biofluctuation zones (Bianchi & Gersonde 2002)	Diatom transfer function (Bianchi & Gersonde 2002)	0.9-1.9
Pacific sector							
DSDP 593	40.51, 167.67	N of STF	15.61 (Cortese et al. 2013)	1	Correlating benthic $\delta^{18}O$ with LR04 (Cortese et al. 2013)	Planktonic foraminifera transfer function (Cortese et al. 2013)	3.2-9.7
ODP 1123	41.79, -171.5	N of STF	14.94 (Cortese et al. 2013)	1	Correlating benthic $\delta^{18}O$ with LR04 (Cortese et al. 2013)	Planktonic foraminifera transfer function (Cortese et al. 2013)	2.4-3.1
SO136-003	42.3, 169.88	N of STF	15.4 (Pelejero et al. 2006) 15.55 (Cortese et al. 2013)	1	Converting SPECMAP ages (Pelejero et al. 2006) onto LR04 Correlating planktonic (*G. bulloides*) $\delta^{18}O$ (Barrows et al. 2007) with LR04 (this study) Correlating benthic $\delta^{18}O$ with LR04 (Cortese et al. 2013)	Alkenone based U^{K}_{37} (Pelejero et al. 2006) Planktonic foraminifera transfer functions (Barrows et al. 2007) Planktonic foraminifera transfer function (Cortese et al. 2013)	0.5-3 0.5-4 0.8-4.4

Core	Latitude (°S), Longitude (°E)	Oceanographic position	Modern SST (°C) (*summer SST)	Modern sea ice	Chronology for MIS 5e	SST proxy for MIS 5e	Sample resolution (ka)
MD06-2986	43.45, 167.9	N of STF	14.93 (Cortese et al. 2013)	1	Correlating benthic $\delta^{18}O$ with LR04 (Cortese et al. 2013)	Planktonic foraminifera transfer function (Cortese et al. 2013)	1.8-3.9
DSDP 594	45.52, 174.95	SAZ	10.41 (Cortese et al. 2013)	1	Correlating benthic $\delta^{18}O$ with LR04 (Cortese et al. 2013) Correlating benthic (*Uvigerina* sp.) $\delta^{18}O$ (Nelson et al. 1993) with LR04 (this study)	Planktonic foraminifera transfer function (Cortese et al. 2013) Planktonic foraminifera transfer functions (Barrows et al. 2007)	0.1-2.1 0.5-1.6
MD97-2120	45.54, 175.93	SAZ	11.8 (Pahnke et al. 2003)	1	Correlating planktonic (*G. bulloides*) $\delta^{18}O$ (Pahnke et al. 2003) to LR04 (this study)	Mg/Ca composition of *Gg. bulloides* (Pahnke et al. 2003)	0.5-1
Y9	48.24, 177.34	SAZ	8.82 (Cortese et al. 2013)	1	Correlating benthic $\delta^{18}O$ with LR04 (Cortese et al. 2013)	Planktonic foraminifera transfer function (Cortese et al. 2013)	1.9-2.7
SO136-038	50.22, 175.31	SAZ	8 (Cortese et al. 2013)	1	Correlating benthic $\delta^{18}O$ with LR04 (Cortese et al. 2013)	Planktonic foraminifera transfer function (Cortese et al. 2013)	5.6-5.7
MD97-2109	50.63, 169.38	SAZ	9.05 (Cortese et al. 2013)	1	Correlating benthic $\delta^{18}O$ with LR04 (Cortese et al. 2013)	Planktonic foraminifera transfer function (Cortese et al. 2013)	1.9-2.9
SO136-111	56.67, 160.23	PFZ	5.54* (Waelbroeck et al. 2009)	1	SPECMAP ages (Crosta et al. 2004) converted onto LR04	Diatom transfer function (Crosta et al. 2004)	0.5-1.7

Core	Latitude (°S), Longitude (°E)	Oceanographic position	Modern SST (°C) (*summer SST)	Modern sea ice	Chronology for MIS 5e	SST proxy for MIS 5e	Sample resolution (ka)
PS58/271-1	61.24, -116.05	PFZ	3.05* (Waelbroeck et al. 2009)	1	EDC3 ages (Benz et al. 2016) converted onto LR04	Diatom transfer function (Esper & Gersonde 2014b)	0.1-0.2

Table 2.1 Details for the cores analysed as part of this study. Cores are ordered by latitude within the three SO sectors (Atlantic-Indian-Pacific). The position of the cores relative to the modern SO fronts is given along with the modern SST (asterisks indicate summer SST rather than mean annual SST) and the present sea-ice conditions. For the sea-ice conditions: 1 – core is located north of the maximum WSIE (FCC <1 %), 2 – core is located north of the mean and south of the maximum WSIE (FCC = 1-3 %), 3 – core is located at or south of the mean WSIE (FCC >3 %). The chronological method applied to a core and the proxy method used to determine MIS 5e SSTs together with the sample resolution and the source data references are given. AZ: Antarctic Zone, PFZ: Polar Frontal Zone, SAZ: Subantarctic Zone.

2.4 Age models

An important consideration for the published records is the robustness of their age models and the comparability between records. The publications in Table 2.1 span nearly 30 years and thus use a range of chronologies. In order to improve the robustness of my comparison, I calibrated the age models of the records, where possible, to the LR04 benthic foraminifera $\delta^{18}O$ stack (Lisiecki & Raymo 2005). The majority of the 32 core records were either originally published on the LR04 chronology (10 records) or could be converted directly from the SPECMAP chronology (6 records) or EDC3 time-scale for the EPICA Dome C ice core in East Antarctica (3 records) (Table 2.1). Records published on the SPECMAP and EDC3 age scales were translated onto the LR04 chronology using the conversion tables in Lisiecki & Raymo (2005) and Parrenin et al. (2013b), respectively.

Nine of the records (DSDP Site 594, MD88-770, MD02-2488, MD84-551, ODP Site 1094, SO136-003, PS1768-8, PS2102-2 and MD97-2120) were converted onto the LR04 chronology by tying the $\delta^{18}O$ data for each core to the LR04 stack (Figures 2.2 & 2.3) using the AnalySeries software (Paillard et al. 1996). For three of these records benthic $\delta^{18}O$ data were available (Figure 2.2) and for the other six planktonic $\delta^{18}O$ data were available (Figure 2.3). For the correlation of $\delta^{18}O$ curves I selected tiepoints (Table 2.2) (Chadwick 2022) that marked the midpoint of major $\delta^{18}O$ shifts at MIS stage or sub-stage boundaries, with the age assignment for the MIS 5 sub-stages following Govin et al. (2009). For each core, a minimum of 4 tiepoints were selected and a maximum of 6 was imposed by the AnalySeries software. All nine cores have a tiepoint at the midpoint of Termination II and, with the exception of MD02-2488, Termination I. The other prominent boundaries used as tiepoints in the majority of the core records are MIS 4-5a, MIS 5a-5b and MIS 5d-5e. Only cores ODP Site 1094 and PS1768-8 have tiepoints not situated on stage or sub-stage boundaries. Both cores have a tiepoint at the initiation of Termination II which was added to help with graphical alignment of the records but does not influence the age model for the interval of interest in this work. ODP Site 1094 also has a tiepoint at the $\delta^{18}O$ minimum during MIS 5e which was added to counter the poor sample resolution during MIS 5b-d. Without this additional tiepoint there would be no age constraints for ODP Site 1094 between Termination II and the MIS 5a-5b boundary.

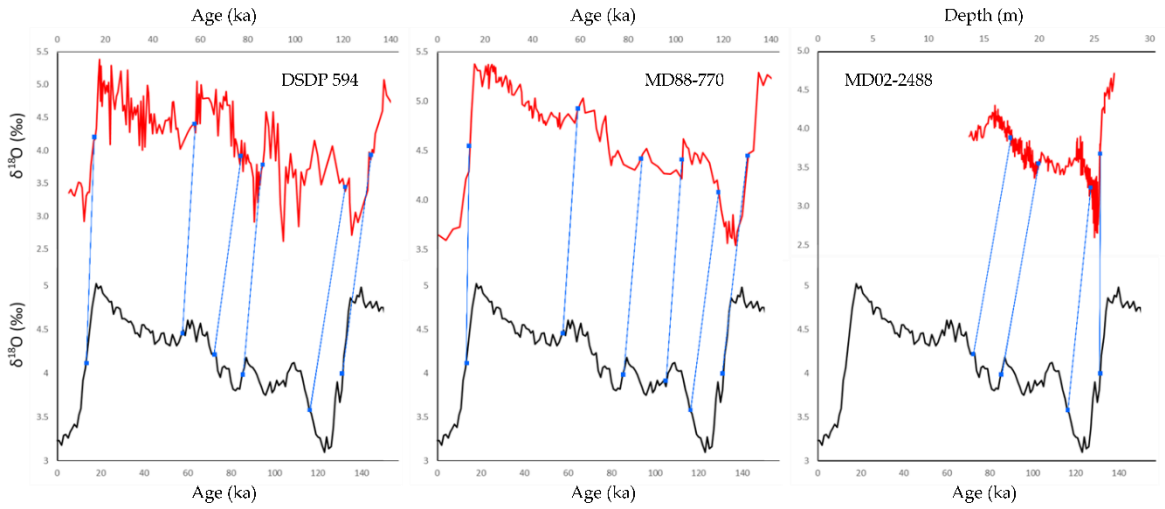

Figure 2.2 Correlations between the benthic $\delta^{18}O$ data (plotted vs. depth or original age) from cores DSDP Site 594, MD88-770 and MD02-2488 (all in red) and the LR04 benthic $\delta^{18}O$ stack (black). Tiepoints are marked by blue squares and connecting lines.

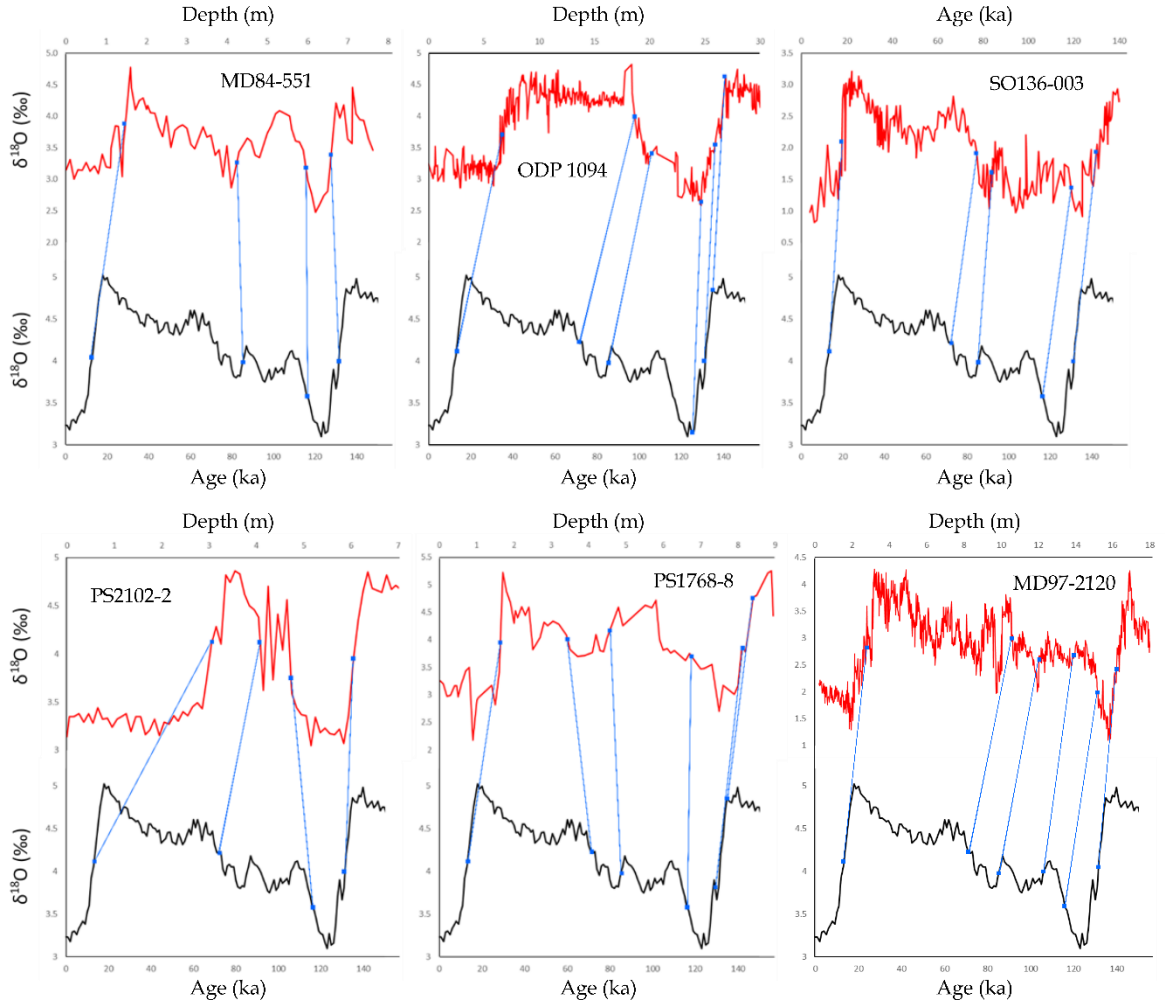

Figure 2.3 Correlations between the planktonic $\delta^{18}O$ data (plotted vs. depth or original age) from cores MD84-551, ODP Site 1094, SO136-003, PS2102-2, PS1768-8 and MD97-2120 (all in red) and the LR04 benthic $\delta^{18}O$ stack (black). Tiepoints are marked by blue squares and connecting lines.

	Termination I	MIS 3-4	MIS 4-5a	MIS 5a-b	MIS 5c-d	MIS 5d-e	Termination II
DSDP 594	X	X	X	X		X	X
MD88-770	X	X		X	X	X	X
MD02-2488			X	X		X	X
MD84-551	X			X		X	X
ODP 1094	X		X	X			X
SO136-003	X		X	X		X	X
PS1768-8	X		X	X		X	X
PS2102-2	X		X			X	X
MD97-2120	X		X	X	X	X	X

Table 2.2 The MIS stage and sub-stage boundaries used as tiepoints in each of the nine core records to correlate their $\delta^{18}O$ values to the LR04 stack. **X** marks which stage or sub-stage boundaries have been used as a tiepoint for that record. Only cores ODP Site 1094 and PS1768-8 have tiepoints that are not (sub-)stage boundaries and thus are not listed in this table.

For all the records on the LR04 chronology, the stated error during the last 1 Ma is ~4 ka (Lisiecki & Raymo 2005). However, for distinct shifts in the LR04 stack (e.g. Termination II) the error on the chronology is likely to be <3 ka (Cortese et al. 2013). The most robust age models are from cores with benthic foraminifera $\delta^{18}O$ data that could be directly correlated with the LR04 stack, and cores with existing SPECMAP or EDC3 tuned chronologies which could be translated onto the LR04 chronology. Age models based on correlations of planktonic foraminifera $\delta^{18}O$ data to the LR04 stack are considered less robust because changes in surface water temperatures incorporated in the $\delta^{18}O$ signals of planktonic foraminifera are unlikely to be fully synchronous with changes in deep water $\delta^{18}O$ composition (mainly global ice volume) represented by the benthic LR04 stack. The least robust chronologies are those for the four records without $\delta^{18}O$ data, which were dated by diatom biofluctuation stratigraphy (PSS76-4, PS2603-3 and PS2305-6) (Bianchi & Gersonde 2002) or by *Cycladophora davisiana* radiolarian abundance stratigraphy (PS1752-1) (Brathauer et al. 2001). The stratigraphy for PS1752-1 was converted onto the LR04 chronology using the *C. davisiana* peak ages published in Pugh et al. (2009).

For cores with age models of different robustness (e.g. ODP Site 1094 and SO136-003), the ages for peak SSTs are within 2 ka of each other and therefore within the error of the LR04 stack. Similarly, for the three cores with the least robust age models the ages of peak warming are within 1-2 ka of other Atlantic and Indian sector records situated south of the PF. The consistency between ages for MIS 5e SST peaks in records with different age model robustness, but from the same SO sector

justifies the inclusion of all records in the analysis of the timing of peak SSTs and sea-ice minima in the different SO sectors. All cores, for which SSTs have been correlated to ice-core deuterium records (ODP Site 1094, MD02-2488 and MD97-2120), were tied to the LR04 stack using their benthic (MD02-2488; Figure 2.2) or planktonic (ODP Site 1094 and MD97-2120; Figure 2.3) $\delta^{18}O$ records to allow an independent comparison between the SST record from the sediment cores and the atmospheric temperature record from Antarctic ice cores. Hereafter, all ages in this chapter refer to the LR04 chronology unless otherwise stated.

2.5 Results

The MIS 5e SST and WSIE records, including ages for the maximum SSTs and the associated errors form the sample resolution are compiled in Table 2.3. Even though it was possible to determine an age relationship between the MIS 5e SST maximum and WSIE minimum in all three SO sectors, the exact age of the MIS 5e sea-ice minimum at a particular core site could often not be precisely constrained as almost all records have extended MIS 5e sediment intervals in which *F. curta* and *F. cylindrus* are absent (FCC = 0). An exception is the MIS 5e record from core PS2305-6 where the percentage of both taxa during the WSIE minimum never fell below 0.8 %. However, all sites have in common a prolonged MIS 5e period when the site was located north of the mean WSIE (FCC = 1-3 %), and at least a short MIS 5e episode when the site was located north of the maximum WSIE (FCC <1 %).

2.5.1 Sea-surface temperatures

The average ages of peak SSTs across all three sectors during MIS 5e range from 128 ka to 125 ka and thus lie within 3 ka throughout the SO, with the full range of ages spanning 129-123 ka (Table 2.3 & Figure 2.4). The SST maxima in the Atlantic and Indian sectors are both well constrained and occurred on average at 127.4 ± 1.1 ka and 128.7 ± 0.8 ka, respectively (errors are one standard deviation). In contrast, peak MIS 5e SSTs in the Pacific sector, with an average age of 124.9 ± 3.6 ka, are much less consistent.

During MIS 5e, SST isotherms were displaced southwards in the SO (Brathauer & Abelmann 1999, Benz et al. 2016). Assuming that the isotherms delineating the modern ACC fronts did so during MIS 5e too (Bianchi & Gersonde 2002), I use the peak SST from each core to assign its oceanographic zone during that time (Table 2.3; Chapter 2.5.3). For all SO sectors, cores located in the Subantarctic Zone reveal a later average age of MIS 5e peak SSTs, at 124.1 ± 3.6 ka, than those north of the STF and in the Polar Frontal Zone, at 126.8 ± 3.0 ka and 127.3 ± 1.3 ka, respectively (Figure 2.5). In the

	Age of MIS 5e sea-ice min (ka)	MIS 5e minimum sea-ice conditions	Age of MIS 5e SST peak (ka)	Error on MIS 5e SST peak age (ka)	MIS 5e peak SST (°C) (*summer SST)	MIS 5e oceanographic zone	References for MIS 5e conditions
Atlantic sector							
PS2489-2	-	-	127.7	±0.8	11.8*	SAZ	Becquey & Gersonde (2003)
PS2082-1	-	-	127	±2.5	14.1*	N of STF	(Brathauer & Abelmann 1999)
PS1752-1	-	-	128.7	+10.9, -4.9	6.0*	SAZ	(Brathauer 1996)
PS1778-5	128.2 ± 1.3	1	127	+2.4, -0.6	6.8*	SAZ	(Brathauer & Abelmann 1999, Gersonde & Zielinski 2000)
ODP 1093	125 ± 1.2	1	124.9	±0.3	5.0*	PFZ	(Schneider Mor et al. 2012)
PS1768-8	127.5 ± 1.3	1	128.1	±1.0	3.9*	PFZ	(Zielinski et al. 1998)
PS2102-2	127.1 ± 3.2	1	129	±0.6	3.8*	PFZ	(Bianchi & Gersonde 2002)
ODP 1094	126.9 ± 4.1 125.8 ± 1.6	1	128.3 126.4	±0.1 ±0.1	4.7* 4.8*	PFZ PFZ	(Bianchi & Gersonde 2002) (Schneider Mor et al. 2012)
PS2276-4	128.2 ± 0.5	1	126.5	+0.5, -0.4	3.1*	PFZ	(Bianchi & Gersonde 2002)
PS2305-6	127.2 ± 1.4	1	127.2	±0.7	1.3*	AZ	(Bianchi & Gersonde 2002)
Indian sector							
RC11-120	-	-	128.8	±0.7	13.5*	N of STF	(Martinson et al. 1987)
MD97-2106	-	-	129.8	±0.6	16.1	N of STF	(Cortese et al. 2013)
MD88-770	-	-	123.7	±0.3	11.1	SAZ	(Barrows et al. 2007)
MD02-2488	-	-	129.4	±0.2	13.3*	N of STF	(Govin et al. 2009)

	Age of MIS 5e sea-ice min (ka)	MIS 5e minimum sea-ice conditions	Age of MIS 5e SST peak (ka)	Error on MIS 5e SST peak age (ka)	MIS 5e peak SST (°C) (*summer SST)	MIS 5e oceanographic zone	References for MIS 5e conditions
MD97-2108	-	-	127.8	+1.4,-1.5	14.4	N of STF	(Cortese et al. 2013)
MD84-551	-	-	128.9	+1.4, -1.3	6.1*	PFZ	(Pichon et al. 1992)
PS2603-3	124.2 ± 3.2	1	127.4	±0.7	3.8*	PFZ	(Bianchi & Gersonde 2002)
Pacific sector							
DSDP 593	-	-	123.9	+1.6, -3.5	15.1	N of STF	(Cortese et al. 2013)
ODP 1123	-	-	118.8	±1.4	17.4	N of STF	(Cortese et al. 2013)
SO136-003	-	-	128.1 127.6 129.8	+0.5, -0.4 ±0.5 +0.2, -0.4	15.4 15.6 19.0	N of STF N of STF N of STF	(Barrows et al. 2007) (Cortese et al. 2013) (Pelejero et al. 2006)
MD06-2986	-	-	126.1	+1.1, -0.9	16.4	N of STF	(Cortese et al. 2013)
DSDP 594	-	-	123.1 128.6	+0.5, -0.9 ±0.5	15.2 15.6	N of STF N of STF	(Cortese et al. 2013) (Barrows et al. 2007)
MD97-2120	-	-	126.8	±0.8	16.1	N of STF	(Pahnke et al. 2003)
Y9	-	-	121.8	±1.3	12.3	SAZ	(Cortese et al. 2013)
SO136-038	-	-	117.7	±2.8	10.6	SAZ	(Cortese et al. 2013)
MD97-2109	-	-	122.4	+1.4, -1.5	11.6	SAZ	(Cortese et al. 2013)
SO136-111	124.1 ± 6.1	1	127.4	+0.3, -0.8	6.1*	PFZ	(Crosta et al. 2004)
PS58/271-1	127.9 ± 0.4	1	125.8	+0.3, -0.6	3.1*	PFZ	(Esper & Gersonde 2014b, a)

Table 2.3 (previous page) Published ages and values of MIS peak SSTs with associated errors from the sample resolution (+ indicates younger ages, - indicates older ages). Ages for the MIS 5e minimum in WSIE are given as the centre age of the MIS 5e interval with either FCC <1 % or FCC = 0 % (for a core with an MIS 5e interval barren of sea-ice diatoms), with the errors indicating the duration of this interval. The MIS 5e sea-ice conditions use the same definitions as Table 2.1: 1 – core is located north of the maximum WSIE. The peak MIS 5e SSTs are also given alongside the inferred oceanographic setting, assuming that SSTs at fronts during MIS 5e were similar to those at the modern SO fronts. Cores are listed in the same order as Table 2.1. AZ: Antarctic Zone, PFZ: Polar Frontal Zone, SAZ: Subantarctic Zone.

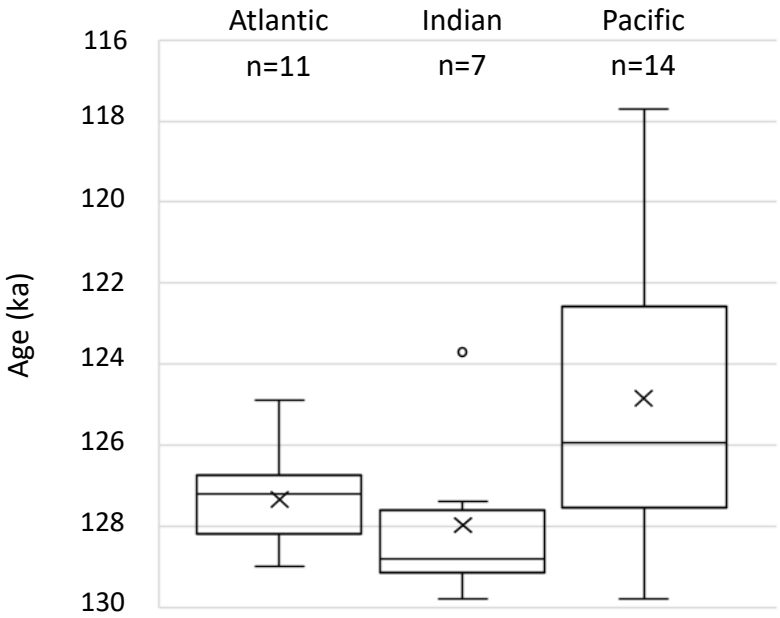

Figure 2.4 Box plots showing the age distribution of peak SSTs in the three SO sectors during MIS 5e. An x marks the mean age for each sector. The horizontal line within each box marks the median; the box demarcates the interquartile range and the extended vertical lines illustrate the full age range of peak SSTs in each sector. The circle marks an anomalous age from core MD88-770.

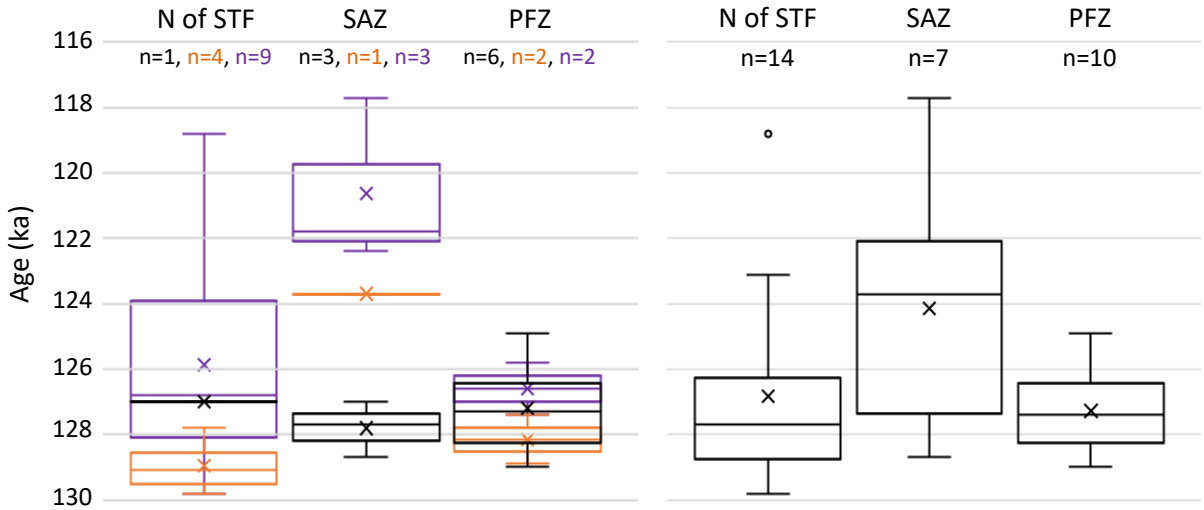

Figure 2.5 (previous page) Box plots showing the age distribution of peak SSTs in the oceanographic zones of each sector (LHS) and the entire SO (RHS) during MIS 5e (SAZ: Subantarctic Zone; PFZ: Polar Frontal Zone). Black – Atlantic, Orange – Indian, Purple – Pacific. There is only one MIS 5e Antarctic Zone record (PS2305-6) which has peak SSTs at 127 ± 0.7 ka. The x marks the mean age for each sector. The horizontal line within each box marks the median; the box demarcates the interquartile range and the extended vertical line illustrates the full range of values.

Pacific sector cores from the Subantarctic Zone, SSTs reached their maximum at 120.6 ± 2.1 ka, over 5 ka later than in the cores north of the STF and from the Polar Frontal Zone, at 125.9 ± 3.2 ka and 126.6 ± 0.8 ka, respectively.

Almost all the core records show increased SSTs during MIS 5e, with the exceptions of cores PS1752-1 and DSDP Site 593, which are characterised by negative SST anomalies of -2 °C and -0.5 °C respectively. For core PS1752-1 the apparent SST cooling is likely due to the large age uncertainty caused by the low sample resolution (Tables 2.1 & 2.3), whilst the cooling at DSDP Site 593 is probably a consequence of local oceanographic changes during MIS 5e (for details, see Cortese et al. (2013)). In the Atlantic sector, only ODP Site 1093 has a peak SST age younger than 129-126 ka (Figure 2.6). The records from cores MD84-551, MD02-2488 and RC11-120, from the central part of the Indian sector, exhibit very similar ages for the SST maxima, around 129 ka, whilst the peak SST in core MD88-770 lags by ~5 ka. Thus, the latter age is clearly an outlier (Figures 2.4 & 2.6) that does not appear to be caused by low resolution or local oceanographic conditions and is excluded when calculating the average age of the MIS SST maximum in the Indian sector. The ages of peak warming in the Pacific sector show considerable variability, although in the majority of the Pacific sector cores peak MIS 5e SSTs occur at younger ages than 127 ka (Figures 2.4 & 2.6). For the records from the Atlantic and Indian sectors, the average sampling interval error is ~0.8 ka, whereas the Pacific sector cores have an average sampling resolution error of ~1.1 ka (Figure 2.6). Core PS1752-1 from the Atlantic sector is the only record for which the error associated with the sample resolution exceeds the error arising from the age model.

MIS 5e SST maxima and their anomalies relative to the modern SSTs are greater at lower latitudes (Figure 2.7a). Peak MIS 5e SSTs of >10 °C and anomalies of >3 °C relative to the present, with the exception of core MD84-551, are only reconstructed from cores located north of 50 °S (Figure 2.7). Cores located 2° south of the modern STF show the greatest warming during MIS 5e relative to the present (e.g. MD97-2108, DSDP Site 594, MD97-2120 and PS2082-1). In cores which are located in the same SO sector and oceanographic zone, but for which MIS 5e SSTs were reconstructed using different techniques, peak SSTs have similar ages (Figure 2.6) and are comparable (Figure 2.7b; e.g. RC11-120 and MD02-2488). The variability of peak SSTs regarding their ages (Figures 2.4, 2.5 & 2.6), deviations from present (Figure 2.7a) and absolute values (Figure 2.7b) observed across the SO

during MIS 5e is primarily related to the core site location (oceanographic zone, SO sector) but not the SST reconstruction technique. This is highlighted by the variation in peak SST values, anomalies and ages in Pacific sector cores north of 51 °S (Figures 2.6 & 2.7), all of which were reconstructed using the same technique.

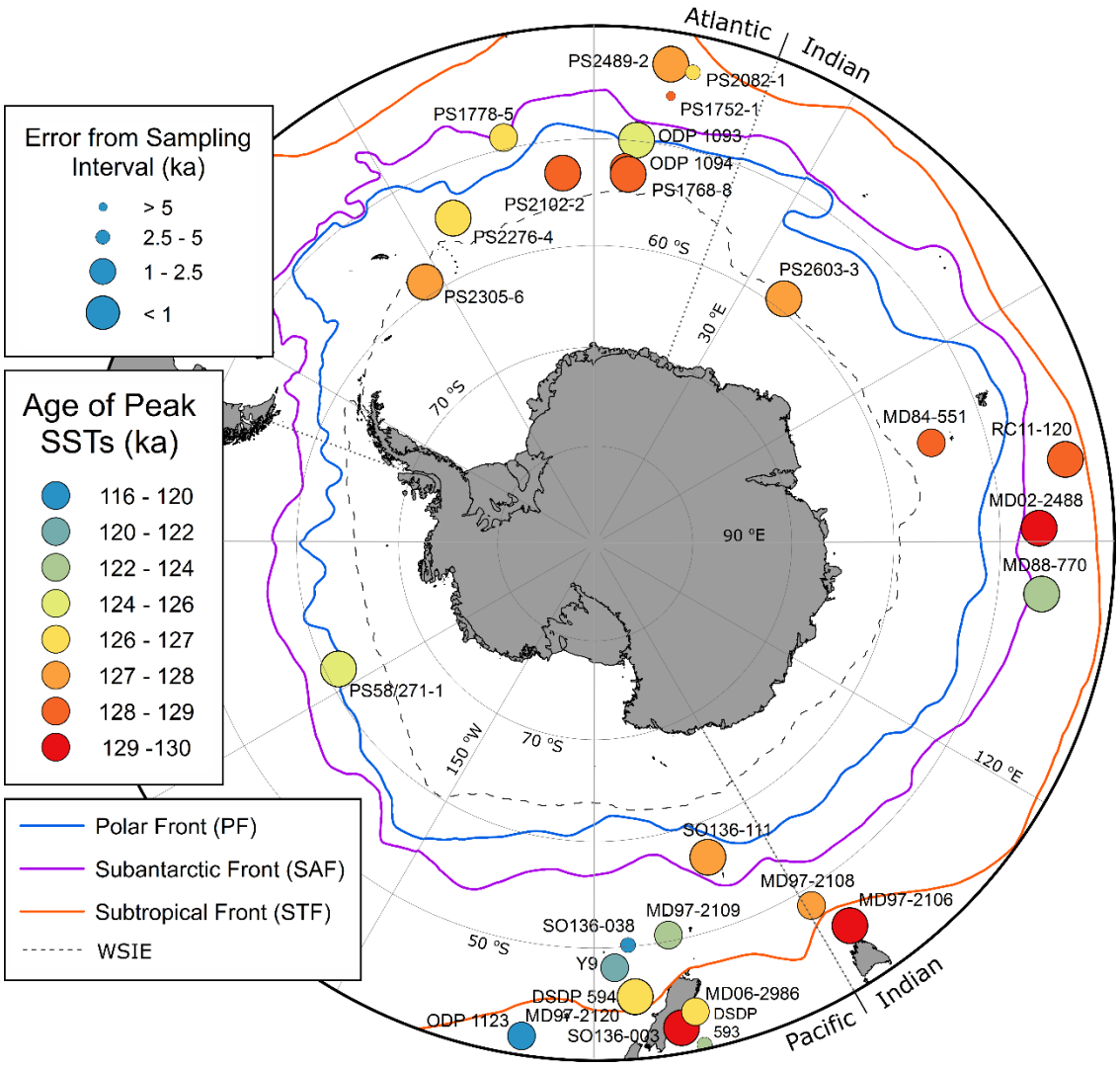

Figure 2.6 Map of the ages of peak SSTs (colour coded) in the MIS 5e records and the age error (symbol size) arising from the sample resolution for each MIS 5e record. The map includes the modern (1981-2010) median September sea-ice extent and SO frontal positions.

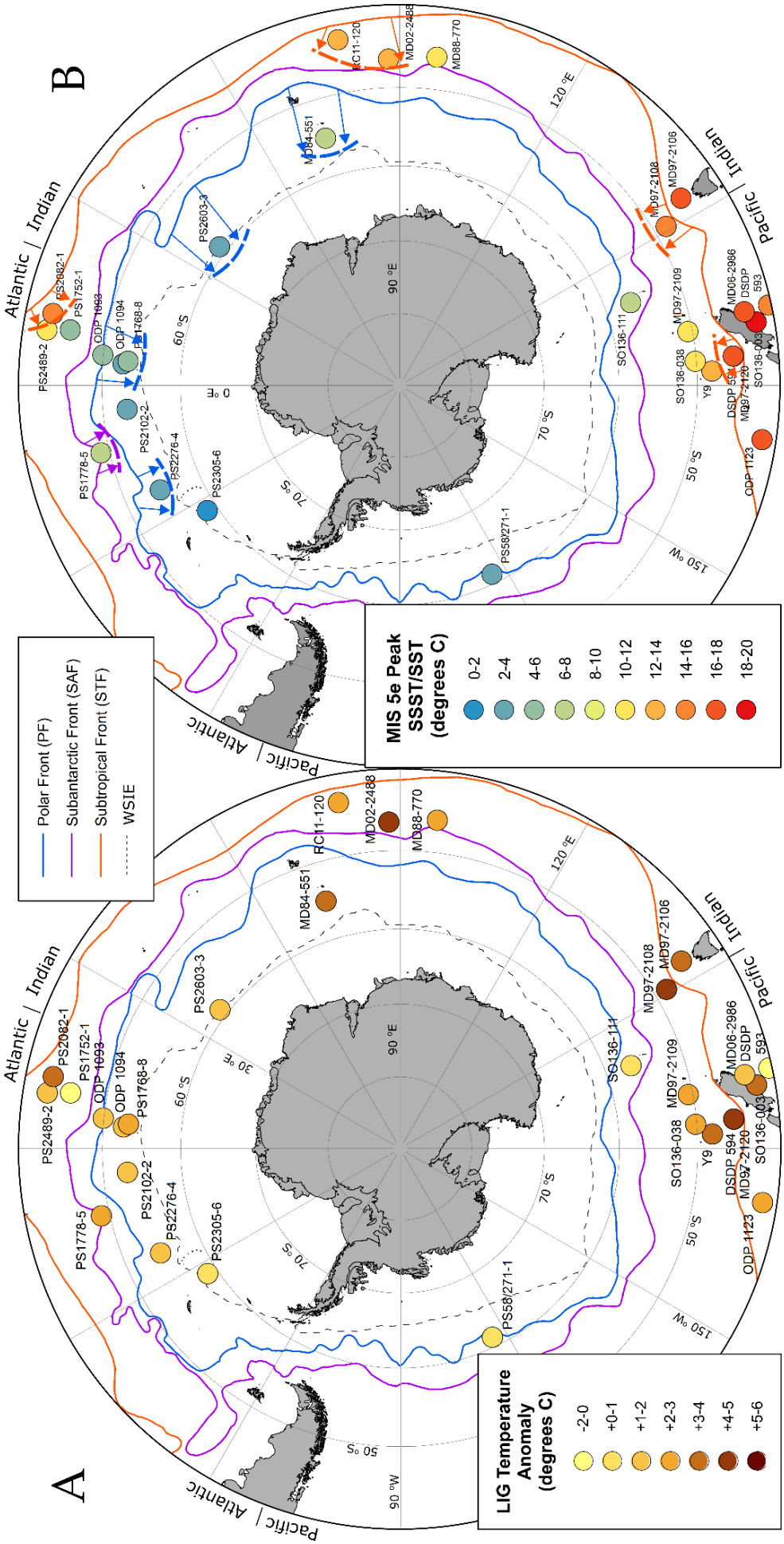

Figure 2.7 **A:** Map with SST anomalies relative to the present for the MIS 5e records. **B:** Map with SST maxima for the MIS 5e records and inferred MIS 5e frontal positions (dashed lines) and their shifts relative to the modern positions (arrows). Both maps have modern SO frontal positions (continuous lines) and median September sea-ice extent for 1981-2010 (grey dashed line). The PF shift south of core MD84-551 may be an artefact of SST over-estimation at this site (Pichon et al. 1992).

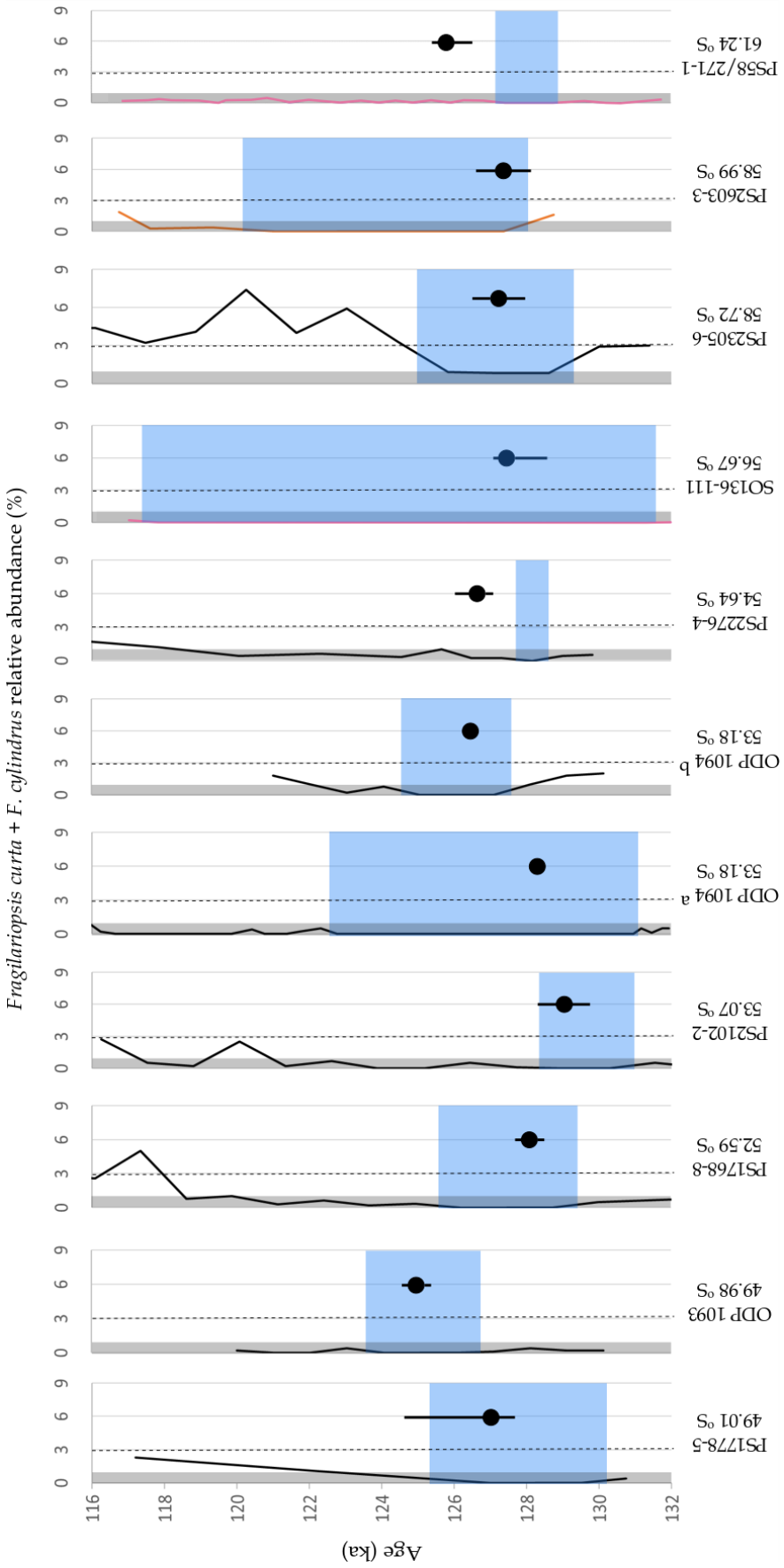

Figure 2.8 *Fragilariopsis curta* and *F. cylindrus* (FCC) downcore abundances for the MIS 5e interval in ten SO marine sediment cores (two records from ODP Site 1094). Black lines are Atlantic sector records, pink lines (SO136-111 and PS58/271-1) are Pacific sector records and the orange line is the only Indian sector record (PS2603-3). Blue shading indicates the period of minimum WSIE, where the lowest FCC abundances are recorded. The dotted vertical lines mark the 3 % threshold for mean WSIE and the grey shading marks the 1 % threshold for maximum WSIE (Gersonde & Zielinski 2000, Gersonde et al. 2003, Gersonde et al. 2005). The black dots mark ages of peak SSTs in each core with error bars arising from the sample resolution. Records are ordered from north to south. [a] Bianchi & Gersonde (2002), [b] (Schneider-Mor et al. 2012)

2.5.2 Sea ice

The records suggest that the age of the MIS 5e WSIE minimum, defined by the centre age of an MIS 5e interval with either FCC <1 % or FCC = 0 % (for a core with an MIS 5e interval barren of sea-ice diatoms), occurred during the time window 129-125 ka, when mean and even maximum WSIE were restricted to the south of each core site at least at one point (Figure 2.8). The onset of the WSIE minimum precedes the SST maximum within each record, except for core PS2603-3, in which both seem to coincide. This sequence is particularly suggested by the data from sites PS2276-4 and PS58/271-1, where the ages of sea-ice minima and peak SSTs are precisely constrained, but where, as in the majority of records, the sea-ice diatom abundance throughout MIS 5e is very low (Figure 2.8). In core PS2305-6, there is a large increase in FCC abundance, from <1 % to ~8 % later in MIS 5e with the FCC maximum occurring 4-5 ka after the end of the WSIE minimum (Figure 2.8).

2.5.3 Oceanographic fronts

Almost all the records show increased SSTs during MIS 5e, which suggests that the oceanographic fronts were positioned further poleward than at present (Brathauer & Abelmann 1999, Benz et al. 2016). The MIS 5e frontal positions (Table 2.4 & Figure 2.7b) are inferred from the reconstructed SSTs (cf. Bianchi & Gersonde (2002)), assuming the same temperature relations across the fronts as in the modern ocean (Orsi et al. 1995, Sikes et al. 2002, Meinen et al. 2003, Dong et al. 2006). The frontal positions inferred for MIS 5e are shown alongside the reconstructed MIS 5e SST maxima and anomalies in Figure 2.7. These reconstructed frontal positions are solely based on the reconstructed peak SSTs for the cores presented here, and thus only cover small spatial areas (Table 2.4). In the Pacific sector, where almost all available records are located near New Zealand (between 160 ^{o}E and 170 ^{o}W), only MIS 5e SST data from a single core (PS58/271-1) is available from the eastern Pacific sector of the SO (170 ^{o}W – 65 ^{o}W). It is important to acknowledge that, if the entire SO was evenly warmed during MIS 5e, relative to the present, then it could give the impression of frontal movement without requiring any actual latitudinal shift of the boundaries between surface water masses. This limitation in the use of SSTs (or sea-surface height) to determine frontal shifts has been taken into account by Gille (2014).

Assuming the reconstructed SSTs are an accurate indicator of frontal location, then the SO fronts were positioned between 1^{o} and 5^{o} further south during MIS 5e when compared to their modern locations, which is consistent with previous reconstructions (Bianchi & Gersonde 2002) (Figure 2.7b). The fronts are best constrained for the SE Atlantic sector (30 ^{o}W – 15 ^{o}E), where the MIS 5e latitudinal ranges of all three fronts show no overlap with those defined by modern SSTs or sea-surface height (Dong et al. 2006, Sokolov & Rintoul 2009) (Figure 2.7b & Table 2.4).

	Modern, hydrographic sections (Orsi et al. 1995)	Modern, sea-surface height (Sokolov & Rintoul 2009)	MIS 5e (this chapter)
30 °W – 15 °E STF	38 – 43 °S	-	43 – 45 °S
30 °W – 15 °E SAF	45 – 48 °S	41 – 48 °S	49 – 51 °S
30 °W – 15 °E PF	49 – 53 °S	48 – 55 °S	55 – 57 °S
70 -100 °E STF	40 – 42 °S	-	45 – 48 °S
70 -100 °E SAF	45 – 49 °S	43 – 51 °S	49 – 52 °S
70 -100 °E PF	48 – 53 °S	56 – 59 °S	S of 56 °S
140 – 180 °E STF	45 – 48 °S	-	46 – 51 °S
140 – 180 °E SAF	52 – 58 °S	50 – 60 °S	52 – 58 °S
140 – 180 °E PF	55 – 62 °S	55 – 64 °S	S of 57 °S

Table 2.4 Inferred MIS 5e frontal positions in the three SO sectors and modern latitudinal ranges of the fronts. The modern positions are given as defined by hydrographic sections (Orsi et al. 1995) and sea-surface height (Sokolov & Rintoul 2009). The former definition utilises hydrographic data up to 1990 and the sea-surface height definition utilises weekly data from 1992-2007.

2.6 Discussion

2.6.1 Sea-surface temperatures

The peak SO warming during MIS 5e seems to occur asynchronously in the three sectors. In the Atlantic and Indian sectors, the SST maxima have well constrained ages of 127.4 ± 1.1 ka and 128.7 ± 0.8 ka, respectively, which are, however, within age-model error of each other and therefore I cannot exclude the possibility that both SST maxima occurred concurrently. The SST record for core MD88-770 (Barrows et al. 2007) is an average of three different transfer function methodologies, with reconstructed SSTs varying between the methods by 0.3-2 °C during MIS 5e, and shows an anomalously late SST peak relative to the other cores from the central part of the Indian sector (RC11-120, MD84-551 and MD02-2488). However, it is worth noting that the artificial neural network derived SST record of Barrows et al. (2007) has an older maximum, with an age similar to that of the SST peaks in the other three cores. The ages of peak SSTs in the Pacific sector vary considerably, from 129.8 ka to 117.7 ka and in most cores from this sector, particularly those from the MIS 5e Subantarctic Zone (Figure 2.6), they seem to lag those of the peak SSTs in the Atlantic and Indian sectors. Average ages of MIS 5e peak SSTs for the different sectors lie within 3 ka (128-125 ka, see Figure 2.4), which is within the uncertainty of the LR04 chronology. Therefore, within error, the MIS 5e SST maxima appear to occur synchronously in all sectors. However, whilst the

offset in timing of peak SSTs between the Atlantic and Indian sectors is ~1.5 ka, SST maxima in several Pacific sector cores occurred over 3 ka later than in the Atlantic and Indian sector cores.

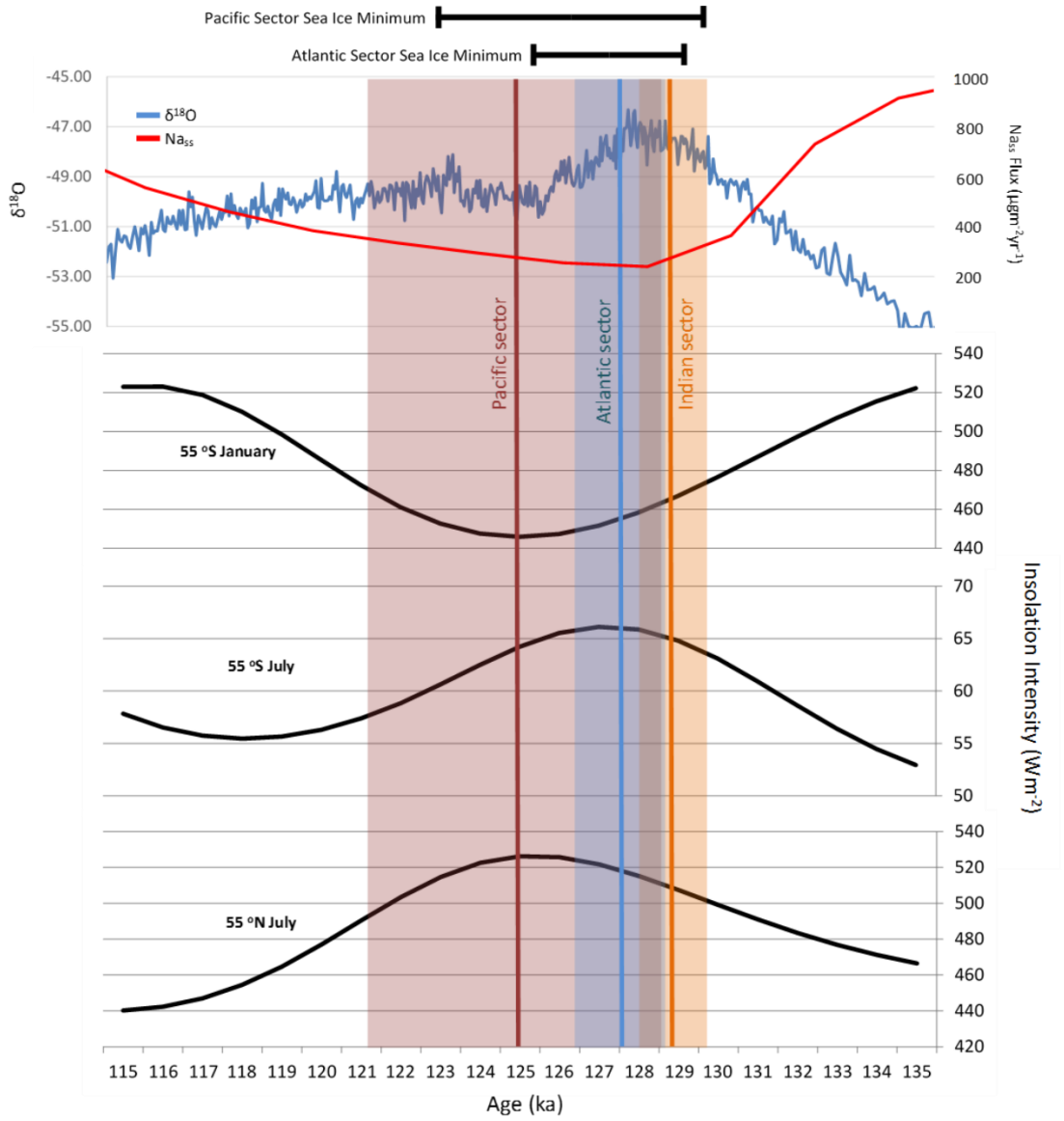

Figure 2.9 EPICA Dome C $\delta^{18}O_{ice}$ (Masson-Delmotte et al. 2011) and Na_{ss} flux (Wolff et al. 2006) records and insolation intensity for the time period 135 – 115 ka (all converted onto the LR04 chronology). The insolation intensities are January or July means for latitudes at 55 °S and 55 °N. The average age of the MIS 5e SST maximum for each SO sector is marked by a vertical line (Red – Pacific sector, Blue – Atlantic sector, Orange – Indian sector), with the standard deviation marked by the shaded area of corresponding colour. The average and standard deviation for the Indian sector was calculated excluding the SSTs from site MD88-770. The average age ranges of the MIS 5e sea-ice minima in the Atlantic and Pacific sectors are also marked.

The three Pacific sector records from the MIS 5e Subantarctic Zone (MD97-2120, Y9 and SO136-038) are all located on the Campbell and Bounty Plateaus, south of New Zealand. These plateaus are overlain by highly stratified and thermally isolated surface waters (Neil et al. 2004). This

isolation, coupled with the northward influx of colder waters along the Pukaki Saddle (Neil et al. 2004, Cortese et al. 2013) could explain the later age of peak SSTs observed in the three records.

Antarctic air temperature, documented in isotope records from East Antarctic ice cores (Masson-Delmotte et al. 2011, Holloway et al. 2017), reaches a maximum at 127.7 ka. The ice-core chronologies have an uncertainty of 1.5 ka during MIS 5e (Bazin et al. 2013b) and therefore only the Pacific sector reaches maximum SSTs later than peak Antarctic air temperatures during MIS 5e (Figure 2.9). For the Atlantic and Indian sectors, the ages of peak atmospheric and oceanic temperatures overlap within error.

To explore the forcing of maximum SSTs during MIS 5e, I compare the timing of insolation changes with the peak SST ages. The ages of maximum SSTs in the three SO sectors do not match that of peak austral summer insolation (monthly mean for January at 55 ^{o}S), which reaches a minimum between 130 and 120 ka (Figure 2.9). The SST maximum in the Atlantic sector coincides closely with peak austral winter insolation (July monthly mean) at 55 ^{o}S and occurs earlier than peak boreal summer insolation (July monthly mean) at 55 ^{o}N (Figure 2.9). Boreal summer insolation is predicted to drive SO warming via the 'bipolar seesaw' mechanism, whereby increased boreal insolation causes substantial melting and freshwater release from the Northern Hemisphere ice sheets (Marino et al. 2015). This large freshwater release results in reduced North Atlantic overturning and an associated warming of the SO (Stocker & Johnsen 2003, Marino et al. 2015). The MIS 5e SST maxima in the Pacific and Indian sectors do not seem to match any of the Southern Hemisphere insolation peaks (Figure 2.9). The peak SST age in the Pacific sector matches that of the insolation peak for boreal summer (July at 55 ^{o}N) but the mechanism behind this concurrence is unknown.

Currently, there are not enough marine MIS 5e records from the SO to test the statistical significance of the temporal offsets between peak SSTs in the three SO sectors, but the ages of the SST maxima appear to have occurred earliest in the Indian and Atlantic sectors followed by the Pacific sector. It is unclear whether this sequence is consistent with the 'bipolar seesaw' model of SO warming during MIS 5e proposed by Holloway et al. (2017) due to the uncertainties in the age models. However, it does seem to suggest the intriguing possibility of other unknown mechanisms, if indeed the SSTs in the Pacific sector reached their maximum later than in the Indian and Atlantic sectors.

2.6.2 Sea ice

Although many of the core records are located too far north to give a precise age for the MIS 5e WSIE minimum, its reconstructed temporal range is largely consistent with an average age of 129-125 ka at the beginning of MIS 5e. Notably, with the exception of ODP Site 1093, the WSIE minima

of all records (Figure 2.8) coincide with the minimum in sea-salt sodium (Na_{ss}) flux in the East Antarctic EPICA Dome C ice cores at ~128 ka (Wolff et al. 2006). Comparisons between the ages of peak SSTs and WSIE minima show that for most cores the peak SSTs occurred within the time of the absolute WSIE minimum. Exceptions may be cores PS2276-4 and PS58/271-1, where the minimum WSIE intervals are better constrained and seem to suggest that minimum WSIE preceded peak SSTs during MIS 5e (Figure 2.8). However, the abundance of sea-ice diatoms in both of these cores are <1 % throughout most of MIS 5e (Figure 2.8), and therefore more southerly cores with precise ages for minimum WSIE during MIS 5e are required to further analyse any possible lead/lag between peak SSTs and minimum WSIE.

The FCC abundance values >0 % in core PS2305-6 suggest that the sea-ice cover during the MIS 5e minimum reached further north in the Scotia Sea than in the Amundsen Sea (PS58/271-1). The WSIE in the Scotia Sea also shows an earlier resurgence following the minimum, with FCC abundances in core PS2305-6 rising to ~8 % within only 4-5 ka (Figure 2.8).

If the sea-ice minimum exactly coincided with the Na_{ss} flux minimum at 128 ka, then it would have preceded the peak SSTs in the Atlantic sector, although this offset is within age model errors. Currently there are only three sea-ice records available from outside the Atlantic sector, so it is difficult to draw robust conclusions on the relative timing of the WSIE minima between the three sectors. The records from the Pacific sector (SO136-111 and PS58/271-1) and the Indian sector (PS2603-3) exhibit WSIE minima during similar time intervals as the Atlantic sector records (Figures 2.8 & 2.9), so it appears the MIS 5e WSIE minimum occurred largely synchronously throughout the SO.

The age ranges for the WSIE minima during MIS 5e encompass the 127 ka insolation peak for austral winter (July mean) at 55 ^{o}S (Figure 2.9). Peak austral winter insolation results in a milder and shorter austral winter with reduced sea-ice formation, whilst the nearly coinciding minimum in austral summer insolation (January mean at 55 ^{o}S) is characterised by a cooler but longer austral summer, resulting in increased sea-ice melt back, as is supported by the model results of Huybers & Denton (2008). The peak in austral winter insolation could therefore have driven Antarctic sea-ice retreat at 127 ka.

The possible importance of shorter austral winter duration with milder July temperatures in the timing of the WSIE minimum during MIS 5e might explain the seeming decoupling between the timing of the WSIE minimum and peak SSTs in cores PS2276-4 and PS58/271-1 (Figure 2.8). For both of these cores the SST records are summer SSTs, not annual SSTs, and thus do not incorporate the potentially crucial winter SSTs. The peak in summer SSTs may reflect a period of increased seasonality, with warmer summers and cooler winters, rather than the period when annual SSTs

were highest for MIS 5e. There is also the possibility that the transfer functions used to reconstruct summer SSTs during MIS 5e are sensitive to events of a different frequency or magnitude than those recorded by FCC abundances.

2.6.3 Oceanographic fronts

The reconstructed peak SSTs during MIS 5e were higher than today, suggesting more southerly frontal positions in the SO. The inferred latitudinal shifts of the MIS 5e frontal positions, when compared with the present, assume that the SST characteristics of SO surface water masses are the same as the modern during MIS 5e. These latitudinal shifts vary substantially, with some fronts (e.g. STF at 30 °W – 15 °E) having shifted by only 1° and others (e.g. PF at 30 °W – 15 °E) having shifted by 5°. The differences in the latitudinal frontal shifts could be related to bathymetric constraints. For example, Moore et al. (1999) showed that the latitudinal position of the present day PF in areas without such constraints varies considerably on seasonal and annual timescales but that such variations are reduced in areas where bathymetric features "pin" the frontal position. Notable areas where fronts are pinned include Drake Passage, Kerguelen Plateau and the Pacific-Antarctic Ridge (Orsi et al. 1995). Thus, core sites located close to these regions probably recorded only very limited shifts of frontal positions during MIS 5e.

The overall concentric geographical pattern of the SO fronts was the same during MIS 5e as today, with the reconstructed frontal positions between 140 °E and 180 °E located more southerly than in other regions, and the fronts between 30 °W and 15 °E located at the most northerly positions when compared to other regions (Table 2.4). However, the MIS 5e frontal positions are averages for each region (Table 2.4) and only represent a limited geographical coverage of the entire SO. Therefore, they may not be an accurate representation of the full latitudinal range of frontal position shifts during the MIS 5e climatic optimum. This is particularly true for the Pacific sector, where there is considerable spatial bias in the distribution of available records, with only a single MIS 5e SST record from the area between 65 °W and 170 °W. The reconstructions of frontal positions are also potentially biased by the proxy records, which can exacerbate the actual SST signal. This is evident from the +2.5 °C over-estimation of the modern SST by the diatom assemblage inferred SST from core-top sediments at site MD84-551 (Pichon et al. 1992). SST over-estimation due to proxy is also indicated for the MIS 5e SST maximum at site SO136-003, for which Pelejero et al. (2006) reconstructed 19.6 °C, whereas Barrows et al. (2007) and Cortese et al. (2013) concluded SST maxima of only 16.24 °C and 16.4 °C, respectively. The higher SST reconstructed by Pelejero et al. (2006) used the biomarker proxy $U^{K'}_{37}$, which - similar to Mg/Ca ratios measured on calcareous shells of planktonic foraminifera - produces warmer SSTs than microfossil assemblages (Hoffman et al. 2017) and which reproduces less accurate modern SSTs in regions with cool surface waters

(Filippova et al. 2016). However, most of the SST proxy records reported here use microfossil transfer functions, and so the risk of any bias in the SST values is minimal, which suggests the frontal positions reconstructed for MIS 5e are reliable, even if the absolute SST values are not. The type of microfossil group used in the MIS 5e SST reconstructions has no impact on the timing of the peak SSTs.

The differences between the MIS 5e and the modern SSTs are largest (>3 °C) in the region between 45 °S and 49 °S and between 140 °E and 180 °E (Figure 2.7a). This is interpreted as a consequence of the STF location in this region having shifted south of 46 °S during MIS 5e, i.e. at least 1 ° further south than at present (Figure 2.7b). The MIS 5e shifts in the STF position are associated with the largest SST anomalies due to the greater thermal gradient across this front when compared to the SAF and PF (Orsi et al. 1995). In the Atlantic sector, the ages of peak MIS 5e SSTs within the four oceanographic SO zones are all coeval within the age model errors (Figure 2.5). This suggests that the SST maxima and most poleward ACC frontal positions during MIS 5e were reached at the same time within this sector. SSTs north of the STF and in the Polar Frontal Zone of the Indian and Pacific sectors peaked around the same time (Figure 2.5). SSTs in the Subantarctic Zone of the Pacific sector reached their maxima 3-7 ka later than in the other sectors and other oceanographic zones (Figure 2.5).

Although the peak SST during MIS 5e was higher than the present day SST at almost every core site, the positive SST anomalies vary between 0.1 °C and 5.2 °C (Figure 2.7a). The lack of consistent SST increases may result from some cores having been affected by the same surface water mass during both the present and MIS 5e (e.g. PS2305-6, SO136-003 and PS58/271-1), whereas others were bathed by different surface water masses during these times (e.g. DSDP Site 594, MD97-2108 and MD84-551). Variability of SST anomalies between core sites across the SO and within the same SO sector strengthen the argument that the higher SSTs during MIS 5e are associated with the poleward shift of the SO fronts and associated water masses. If the entire SO warmed evenly and independently of any change in the location of a front (Gille 2014) then the SST anomalies should be more consistent between sites, at least between sites from the same SO sector. High latitude sites south of 55 °S have MIS 5e SST anomalies <1 °C, which may suggest that MIS 5e warming closer to the Antarctic continent was less pronounced than north of the PF. However, the observed slight trend towards higher SST anomalies at more northerly SO sites than at sites nearer to the Antarctic continent may be an artefact caused by the higher SST anomalies being associated with the southward shift of the STF (Figure 2.7b).

2.6.4 Wider implications

The high SST maxima and inferred poleward shifts of the SO fronts during MIS 5e must have had impacts on both the Antarctic region and further afield. The more southerly position of the ACC fronts was compatible with a poleward shift in the westerly wind field, which would have resulted in a more southerly precipitation field and storm tracks (Russell et al. 2006, Liu & Curry 2010). More southerly storm tracks would have increased sea-ice break up and promoted a reduced annual sea-ice duration and extent (Hall & Visbeck 2002). The precipitation field shift would also have resulted in reduced precipitation in regions like southern Australia and increased precipitation closer to Antarctica (Fletcher & Moreno 2011, Saunders et al. 2012). Changes in the precipitation sources and fields also have an effect on the interpretation of ice core records because they can affect the air temperature signature of water isotopes (Masson-Delmotte et al. 2011).

A more southerly and warmer ACC would also have caused increased warming of the continental shelves around Antarctica with anomalous bottom Ekman flow (Spence et al. 2017), causing increased advection of relatively warm ACC water masses, such as Circumpolar Deep Water, onto the Antarctic continental shelf (Fogwill et al. 2014). Increased warm water upwelling would have increased melting of floating ice shelves (Ronne-Filchner, Ross, Amery etc.) and at grounding zones of marine-terminating ice streams around Antarctica which, in turn, would have caused major mass loss from the Antarctic ice sheets (Pollard & DeConto 2009, DeConto & Pollard 2016), similar to what has been observed along the Pacific margin of Antarctica today (Jenkins et al. 2016, Shepherd et al. 2018, Rignot et al. 2019) and since the last ice age (Hillenbrand et al. 2017). Intrusions of warm water into the Weddell Sea might have caused significant reduction in sea-ice formation, given the high rates of sea-ice production in this area today (Haid & Timmermann 2013), as well as considerable loss of glacial ice (Hellmer et al. 2012). Warming of Weddell Sea waters and the poleward shift of the northern boundary of the Weddell Gyre (Orsi et al. 1995) would also have reduced the extent of the Weddell Gyre circulation whilst increasing its strength (Wang 2013). A similar scenario can also be assumed for the Ross Sea Gyre.

A poleward shift of the STF would have increased the flow in counter currents, such as the Agulhas Current, that would therefore increase the influx of warmer Indian Ocean waters into the South Atlantic (Biastoch et al. 2009). Other boundary currents, such as the East Australian Current, would also have been able to expand, and this current may have changed its flowpath from north of Chatham Rise to the south of it (Cortese et al. 2013). In contrast, the Brazil Current is unlikely to have changed substantially and shifted its flowpath into Drake Passage because of the inability of the ACC to be displaced substantially poleward through that region (Mazloff 2012). Changes in the boundary currents and fronts would have impacted not only the oceanic conditions but also have

influenced ecosystems within the SO and adjacent ocean basins. An example of this is the effect of an increased Agulhas Current flow that would have injected more warmth into the South Atlantic and reduced nutrient availability, substantially damaging biological productivity in the cold water Benguela Current (Hutchings et al. 2009, Tim et al. 2018).

The reduced sea-ice extent in the SO during MIS 5e would have influenced deep and bottom water formation around Antarctica. A reduction in the extent of sea ice (and possibly also of ice shelves, see above) would have resulted in less formation of dense shelf waters by brine rejection (and by super-cooling in ice-shelf cavities), which in turn would have reduced the rate of deep and bottom water mass production in the SO and caused a subsequent warming of abyssal waters (Armand & Leventer 2003, Ferrari et al. 2014). Reductions in formation of southern-sourced cold deep and bottom waters would have had far reaching consequences for the water column structure of the world ocean. This is because the reduction of SO deep and bottom water masses probably resulted in a slowdown of SO circulation and therefore Atlantic Meridional Overturning Circulation, which in turn may have delayed the re-initiation of North Atlantic Deep Water formation, following its initial shutdown at the beginning of MIS 5e due to meltwater stratification in the North Atlantic (Marino et al. 2015, Holloway et al. 2017). The possible impact of sea-ice decrease in the SO on North Atlantic Deep Water formation gives evidence of its importance for global ocean and atmosphere interactions, and how crucial it is to gain a better understanding of past changes for predicting future changes.

2.7 Conclusions

The available SST records from the SO indicate that the SST maximum during MIS 5e in the Atlantic, Indian and Pacific sectors occurred on average at 127.4 ± 1.1 ka, 128.7 ± 0.8 ka and 124.9 ± 3.6 ka, respectively. Whilst SSTs seem to have peaked simultaneously within the age uncertainties in all three SO sectors, the maximum SSTs in several Pacific sector records occurred much later than those in the Atlantic and Indian sectors, suggesting that peak warming was not synchronous throughout the SO. The low number and limited geographical coverage of records prevents statistical analyses. Nonetheless, the peak SST ages from cores in the Atlantic and Indian sectors indicate that maximum SSTs were reached concurrently with peak atmospheric temperatures measured in Antarctic ice cores (127.7 ka).

The age ranges for MIS 5e sea-ice minima in the SO are consistent with ice core proxy-based estimates of sea-ice extent, but there is a clear need for more marine records from the Antarctic Zone to better constrain the exact timing and position of minimum sea-ice extent during MIS 5e. Better constrained ages for the minimum WSIE will help to interrogate whether an observed

temporal offset between peak SSTs and minimum WSIE in cores PS2276-4 and PS58/271-1 is an artefact or not. Despite the paucity of records from the Indian and Pacific sectors, the WSIE minimum appears to have been synchronous throughout the SO.

The Subtropical, Subantarctic and Polar Fronts were potentially situated at least 1^{o} further south during MIS 5e than today, and accompanying poleward shifts of surface water masses are inferred from SSTs that were considerably higher during MIS 5e than at present. However, the large latitudinal variations in frontal positions observed today, both within a SO sector and on seasonal and annual time scales, make it difficult to accurately reconstruct the ACC structure during MIS 5e based on a limited and geographically restricted number of records. The relatively high number of records from the Atlantic sector, the coherency of the latitudinal temperature gradient reconstructed for these records, and the absence of bathymetric constraints in this region indicate that the MIS 5e frontal migrations there are the most robust.

The proxy records compiled here provide data that can constrain model experiments and test their results. Evaluating numerical models, which simulate the processes operating under a warmer climate, such as during MIS 5e, with palaeo-data as compiled in this chapter, will help improve confidence in predictions of future climate change. The MIS 5e records reveal potential heterogeneity in SO warming and sea-ice reduction that can be used to evaluate the significance of processes built into models, such as deep and bottom water formation and overturning circulation.

Chapter 3 How does the Southern Ocean Palaeoenvironment during MIS 5e compare to the Modern?

3.1 Introduction

The bulk of this chapter is presented in: Chadwick M., Allen C.S., Sime L.C., Crosta X. & Hillenbrand C.-D. 2022. How does the Southern Ocean palaeoenvironment during Marine Isotope Stage 5e compare to the modern? *Marine Micropaleontology*, **170:** 102066.

In the modern Southern Ocean (SO) there is substantial spatial and temporal heterogeneity in the observed sea-ice (Stammerjohn et al. 2008a, Hobbs et al. 2016, Parkinson 2019) and sea-surface temperature (SST) trends (Maheshwari et al. 2013). The published records analysed in Chapter 2 indicate that there was also spatial heterogeneity in SSTs during MIS 5e but the scarcity of existing records from the Antarctic Zone (south of the Polar Front) and within the modern seasonal sea-ice zone (Figure 2.1) limits the reconstruction of MIS 5e sea-ice cover.

In this chapter I reconstruct the SO environmental conditions during MIS 5e using new diatom species assemblage data from seven marine sediment cores located south of 55 ^{o}S (Figure 3.1 & Table 3.1). MIS 5e diatom assemblages are compared to the modern diatom assemblages in SO surface sediments to determine:

- How the SO palaeoenvironment during MIS 5e compares between the three SO sectors
- Whether all three SO sectors show consistent SST warming and sea-ice reduction during MIS 5e relative to the modern.

3.2 Materials and methods

3.2.1 Core sites

The seven marine sediment cores for which MIS 5e palaeoenvironmental conditions are reconstructed are detailed in Table 3.1. These cores were selected as they contain >20 cm thick intervals of diatom rich MIS 5e sediments and are located further south than almost all cores with existing MIS 5e diatom records (Chapter 1). Surface sediment from an additional Indian sector core, International Ocean Discovery Program (IODP) Expedition 318 Hole U1361A, is also included in this

chapter. Three of these cores are located in the Atlantic sector, one in the Indian sector and three in the Pacific sector (Figure 3.1).

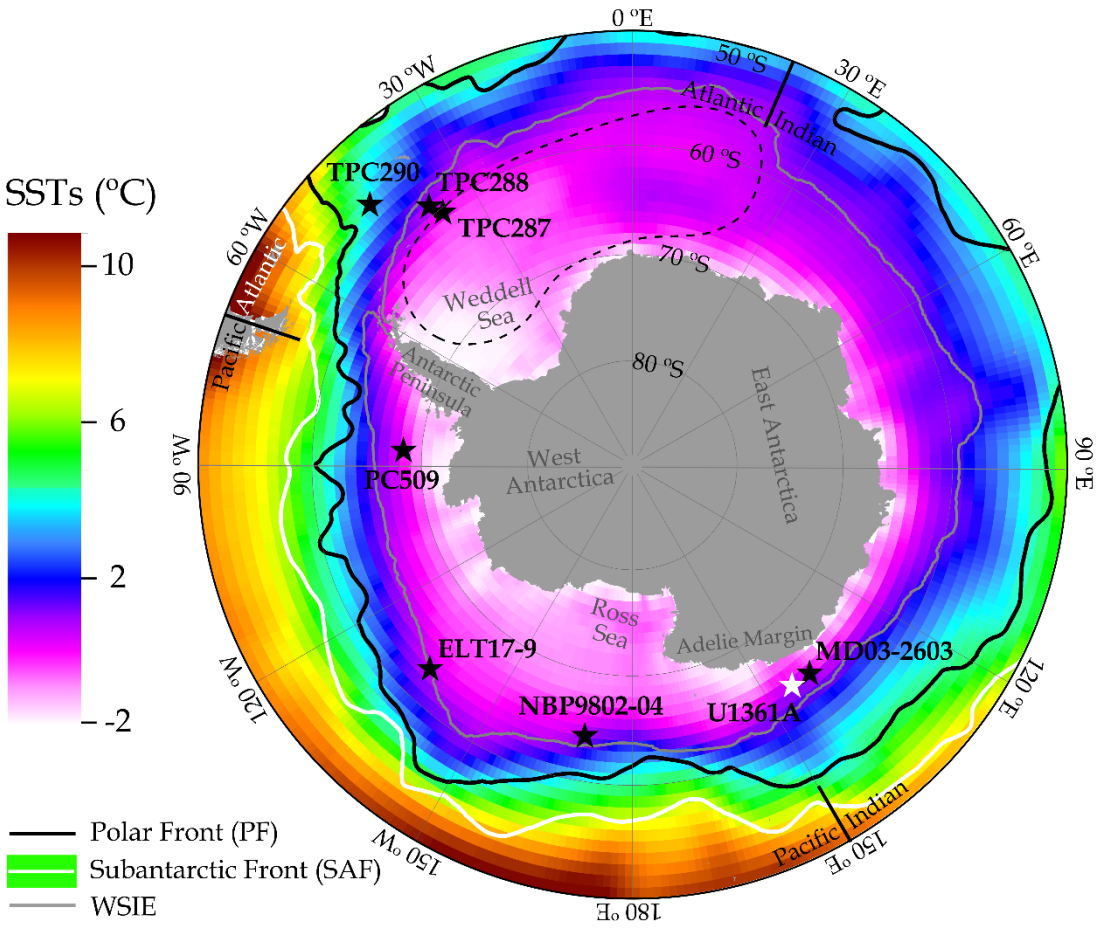

Figure 3.1 Map of core locations (black stars) with modern SSTs, locations of SO fronts and winter sea-ice extent (WSIE). The white star indicates a surface sample (U1361A) assumed to contain a modern diatom assemblage characteristic for the Indian sector. The white line marks the modern SAF (position from Orsi et al. (1995)), the solid black line marks the modern PF (position from Trathan et al. (2000)), the dashed black line marks the extent of the Weddell Gyre (Vernet et al. 2019) and the grey line marks the median September sea-ice extent from 1981-2010 (data from Fetterer et al. (2017)). The background shadings display the mean annual SSTs from 1981-2010 using the COBE-SST2 dataset provided by the NOAA PSL, Boulder, Colorado, USA (https://psl.noaa.gov). The boundaries between the three SO sectors (Atlantic, Indian and Pacific) are also marked.

3.2.2 Diatom counts

For the diatom assemblage data, microscope slides were produced using a method adapted from Scherer (1994). Samples of 7-20 mg of sediment were exposed to 10 % Hydrochloric acid, to remove any carbonate, 30 % Hydrogen peroxide, to break down organic material, and a 4 % Sodium Hexametaphosphate solution, to promote disaggregation during their placement in a warm water

bath for a minimum of 12 hours. The material for each sample was homogenised into a ~10 cm tall water column and allowed to settle randomly onto microscope slide coverslips over a minimum of 4 hours. The water was slowly drained away and coverslips were mounted onto microscope slides with Norland Optical Adhesive (NOA 61). Slides were investigated using a light microscope (Olympus BH-2) at x1000 magnification and a minimum of 300 diatom valves were counted for each sample.

Core	Latitude (°S), Longitude (°E)	Water depth (m)	Cruise , Year	Ship	Core length (cm)
TPC290	55.55, -45.02	3826	JR48, 2000	*RRS James Clark Ross*	1179*
TPC288	59.14, -37.96	2864	JR48, 2000	*RRS James Clark Ross*	940*
TPC287	60.31, -36.65	1998	JR48, 2000	*RRS James Clark Ross*	615*
ELT17-9	63.08, -135.12	4935	ELT17, 1965	*R/V Eltanin*	2018
NBP9802-04	64.20, -170.08	2696	PA9802, 1998	*RV/IB Nathaniel B. Palmer*	740
MD03-2603	64.28, 139.38	3320	MD130, 2003	*R/V Marion DuFresne II*	3033
U1361A	64.41, 143.89	3459	IODP Exp. 318, 2010	*JOIDES Resolution*	38800
PC509	68.31, -86.03	3559	JR179, 2008	*RRS James Clark Ross*	989

Table 3.1 Details of the location and recovery information for the eight sediment cores analysed in this chapter. Cores are ordered by latitude. For IODP Site U1361, only the core top surface sample from Hole U1361A was analysed in this chapter. * For each of the three TPC cores (TPC290, TPC288 and TPC287), the trigger core (TC) and piston core (PC) were spliced together to produce a composite record.

Multiple samples from different cores were tested to ensure that 300 valves captures a representative diversity of the diatom assemblage, e.g. the rate of new species being identified in the sample has flattened off (examples in Figure 3.2). Furthermore, all the species/groups of diatoms that are major components of the final assemblage (>2 %) were identified within the first 50 valves counted for each sample. Therefore, even though a small number of species/groups are still being added to the assemblage after 250-300 valves, these species/groups only constitute trace components of the overall assemblage and enough valves have been counted to stabilise the relative abundances of the major assemblage components.

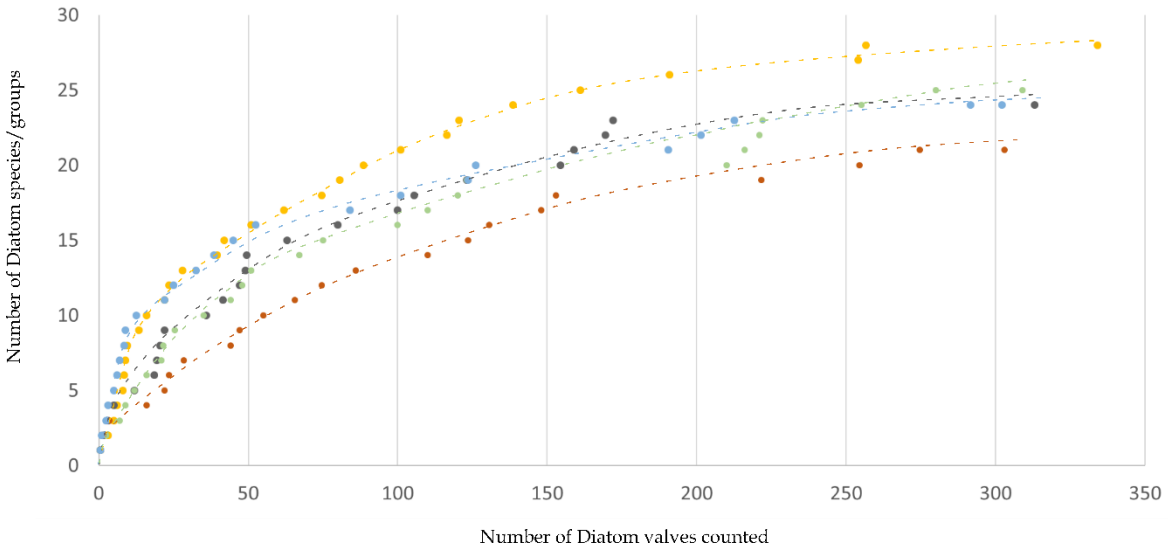

Figure 3.2 Graph of the number of diatom species/groups identified in five test samples against the total number of diatom valves counted. The dashed lines mark the smoothed trends and indicate a flattening rate of species/group addition to the assemblage after 250-300 valves. The final point marked for each sample is the end assemblage after 300+ valves and therefore has the same number of species/groups as the penultimate point.

Diatom species/genera	Modern summer SST (°C)	Modern sea-ice duration (months/yr)
Actinocyclus actinochilus	-0.5 – 0.5 [a]	7.5 – 9 [a]
Azpeitia tabularis	1 – 22.5 [b]	0 – 3.5 [b]
Chaetoceros rs.	-1.3 – 3.5 [a]	0 – 10.5 [a]
Eucampia antarctica	-2 – 9.5 [c]	–
Fragilariopsis curta	-1.3 – 2.5 [a]	5 – 10.5 [a]
Fragilariopsis cylindrus	-1.3 – 1 [a]	7.5 – 10.5 [a]
Fragilariopsis kerguelensis	-1 – 22 [d]	0 – 9 [d]
Rhizosolenia antennata f. *semispina*	0.5 – 2 [e]	1 – 3.5 [d]

Table 3.2 Modern summer SST and sea-ice duration ranges for diatom species and genera that are presented in this chapter. The SST and sea-ice duration ranges for the present day are based on surface sediment samples where the listed species/genera is >2 % of the assemblage. *E. antarctica* does not have any clear relationship to modern sea-ice duration. [a] Armand et al. (2005), [b] Romero et al. (2005), [c] Zielinski & Gersonde (1997), [d] Crosta et al. (2005), [e] Armand & Zielinski (2001).

Diatom relative abundances for each sediment core are reported in this chapter for species or groups with well-constrained present-day ecologies/habitats (Table 3.2). The complete MIS 5e diatom assemblage counts for the seven cores are available from the Polar Data Centre (Chadwick & Allen 2021b, c, d, e, f, g, h). *Actinocyclus actinochilus* is a cold-water species (Table 3.2) generally found in low abundances (<3 %) in SO seafloor surface sediment samples within the maximum WSIE

(Armand et al. 2005, Esper & Gersonde 2014b). Increasing relative abundances of this species in southern high latitude sediments suggest colder SSTs and heavier sea-ice conditions. *Azpeitia tabularis* is a warm water species (Table 3.2), reaching up to 20 % of the total diatom assemblages in the Subantarctic Zone and presenting relative abundances <5 % in surface sediments south of the Polar Front (Romero et al. 2005, Esper & Gersonde 2014b). This species additionally has a southerly occurrence restricted by the maximum WSIE (Zielinski & Gersonde 1997). Increasing abundances of this group in southern high latitude sediments therefore suggest warmer SSTs and ice-free conditions.

The abundance of *Chaetoceros* rs. in SO surface sediments is dominantly influenced by meltwater surface stratification and nutrient availability (Armand et al. 2005), with high surface stratification and nutrient availability resulting in *Chaetoceros* rs. dominated (>60 %) assemblages in coastal Antarctic systems (Leventer & Dunbar 1988, Leventer 1991, 1992, Crosta et al. 1997). High *Chaetoceros* rs. abundances are also associated with moderately consolidated winter sea ice (sea-ice duration = 3-9 months/yr) but this relationship is still poorly understood (Armand et al. 2005). The *Chaetoceros* rs. abundances in this thesis include a small number (up to 1 %) of *Chaetoceros (Hyalochaete)* vegetative cells in some samples. Other than *Chaetoceros* rs., *Fragilariopsis kerguelensis* is the dominant diatom species/group in SO surface sediments, with the greatest abundances found in locations with year-round open ocean conditions (Crosta et al. 2005, Cefarelli et al. 2010, Esper et al. 2010) and, as a result, changes in *F. kerguelensis* abundance are often negatively correlated with changes in *Chaetoceros* rs. abundance. Taken together, an increase in the relative abundance of *F. kerguelensis,* and concurrent decrease in the relative abundance of *Chaetoceros* rs. in my core records indicates a shift from conditions with moderate sea-ice cover and stratified surface waters to open ocean conditions with little or no winter sea-ice cover.

Fragilariopsis curta and *F. cylindrus*, composing the FCC group, are sea-ice associated species (Kang & Fryxell 1992, Beans et al. 2008), presenting their maximum abundances in modern sediments at winter sea-ice concentrations >70 % and SSTs <1 ^{o}C (Armand et al. 2005, Esper & Gersonde 2014b, a). The FCC group is used as a WSIE proxy (Gersonde & Zielinski 2000, Gersonde et al. 2005), as detailed in Chapter 1.3. Increasing relative abundances of the FCC group in my cores therefore infer heavy sea-ice conditions and cold SSTs.

The abundance of *Eucampia antarctica* in SO surface sediments does not show a clear pattern relative to SSTs or sea-ice extent (Zielinski & Gersonde 1997), probably because its two varieties have generally been mixed together. The cold variety of *E. antarctica* has however been related to iceberg flux, with high iceberg flux promoting high *E. antarctica* abundances through meltwater-induced buoyancy and high iron availability (Burckle 1984, Fryxell & Prasad 1990, Allen 2014). Based

on restricted modern studies, high relative abundances of *E. antarctica* cold variety encountered downcore have been used as an indicator of iceberg or marine-terminating glaciers melting (Barbara et al. 2016). The *E. antarctica* relative abundances reported in this thesis only include valves from the cold variety. *Rhizosolenia antennata* f. *semispina* reaches its maximum abundance in SO surface sediments located within, and just north of, the mean WSIE (Crosta et al. 2005) and is also an indicator of high meltwater flux and surface stratification (Allen et al. 2005).

Surface sediment samples from four of the core sites (TPC290, TPC288, TPC287 and PC509) are used to obtain modern diatom assemblages for those sites. For core MD03-2603, the surface sediment sample from the nearby Site U1361 (Table 3.1 & Figure 3.1) is used for the modern diatom assemblage. There was no surface material available for the central Pacific sector cores (ELT17-9 and NBP9802-04) so the MIS 5e diatom assemblages in these cores are not compared against any modern assemblages. Using surface sediment samples to represent the modern surface water conditions is consistent with previous studies (Zielinski & Gersonde 1997, Crosta et al. 1998, Armand et al. 2005, Crosta et al. 2005, Romero et al. 2005, Esper & Gersonde 2014b, a), however, the assemblage preserved in surface sediments is likely an integrated signal of up to 500 yrs. (Miklasz & Denny 2010). The complete surface sediment diatom assemblages can be found at http://dx.doi.org/10.17632/2tnxcww6c8.1, an open-source online data repository hosted at Mendeley Data (Chadwick 2020).

3.3 Age models

3.3.1 Published chronologies

Of the seven sediment cores, for which MIS 5e data are presented in this chapter, five utilise previously published age models (Table 3.3). The chronologies for cores TPC290 and TPC288 are published in Pugh et al. (2009) and utilise the correlation between the magnetic susceptibility (MS) record in marine sediment cores from the Scotia Sea and the dust record in the EPICA Dome C (EDC) ice core over past glacial-interglacial cycles (Pugh et al. 2009, Weber et al. 2012). In both cores this chronology is combined with the abundance stratigraphy of the radiolarian species *Cycladophora davisiana*, with the e_3 low abundance event indicating MIS 5e (Brathauer et al. 2001). The Termination II tiepoint in TPC290 was adjusted from the 7.11 mbsf given in Pugh et al. (2009) to 7.23 mbsf (Allen C.S. unpublished) to improve the alignment of the MS signal in the sediments with the EDC dust record. The chronology for core NBP9802-04 also utilises the correlation between sediment MS and EDC dust, alongside the presence/absence of the diatom species *Hemidiscus karstenii* (Williams 2018), which is a biostratigraphic marker for the MIS 6/7 boundary (Burckle et al. 1978).

Cores MD03-2603 and ELT17-9 have published chronologies tied to the LR04 and SPECMAP age scales respectively (Table 3.3). For core MD03-2603, Presti et al. (2011) correlated its downcore records of Ba/Al and Ba/Ti ratios, which are palaeo-productivity proxies, to the LR04 benthic foraminifera $\delta^{18}O$ stack (Lisiecki & Raymo 2005). The chronology for core ELT17-9 was published by Chase et al. (2003) and uses abundances for *C. davisiana* (Hays J. unpublished data) and *E. antarctica* (Burckle L.H. unpublished data) correlated with their abundance stratigraphies (Burckle & Burak 1995, Brathauer et al. 2001).

Core	SO sector	Chronology for MIS 5e	Chronological uncertainty (ka)
TPC290	Atlantic	Correlating MS from TPC290 to EDC ice core dust record combined with *C. davisiana* abundances (Pugh et al. 2009)*	± 2.58
TPC288	Atlantic	Correlating MS from TPC288 to EDC ice core dust record combined with *C. davisiana* abundances (Pugh et al. 2009)	± 2.59-2.64
TPC287	Atlantic	Correlating MS from TPC287 to MS from TPC288 (Chapter 3.3.2, Figure 3.3)	± 2.57-2.65
ELT17-9	Pacific	Combined abundance stratigraphies of *E. antarctica* and *C. davisiana* on SPECMAP age scale (Chase et al. 2003)	± 2.51
NBP9802-04	Pacific	Correlating MS from NBP9802-04 to EDC ice core dust record combined with LOD *H. karstenii* (Williams 2018)	± 2.68
MD03-2603	Indian	Correlating Ba/Al and Ba/Ti ratios from MD03-2603 to LR04 benthic oxygen isotope stack combined with diatom biostratigraphy (Presti et al. 2011)	± 2.55-2.56
PC509	Pacific	Correlating wet bulk density (= proxy mirroring biogenic opal content) from PC509 to the LR04 benthic oxygen isotope stack (Chapter 3.3.3, Figure 3.4)	± 2.59-2.65

Table 3.3 Summary of the locations and chronologies for the seven sediment cores analysed in this chapter. Cores are ordered by latitude. LOD: Last Occurrence Datum. *For core TPC290 the chronology was adjusted from the age model previously published in Pugh et al. (2009) by shifting the Termination II tiepoint to improve alignment of its MS signal with the EDC dust record (Allen C.S. unpublished).

To allow for consistent comparison of timings between cores, all cores are converted onto the same chronology. The EDC3 chronology (Parrenin et al. 2007) is chosen for this chapter as it has the lowest chronological uncertainty (±1.5 ka) during MIS 5e (Bazin et al. 2013b) and is tuned to SO climatic shifts, as opposed to LR04 which represents a globally-averaged climate signature. The chronologies for cores MD03-2603 and ELT17-9 are converted onto the EDC3 chronology using the conversion tables published in Lisiecki & Raymo (2005) and Parrenin et al. (2013b).

Chronological uncertainties for the MIS 5e ages of samples in this chapter (Table 3.3) vary between 2.5 and 2.7 ka. The EDC3 chronology has an uncertainty of ±1.5 ka (Bazin et al. 2013b) during MIS

5e, with an additional uncertainty of ±1 ka arising from the translation between chronologies (Capron et al. 2014). Each core sample comprises a 0.5 cm thick slice of sediment, and therefore additional age uncertainty due to integrating over the corresponding time interval in each core needs to be taken into account (see Table 3.3).

3.3.2 TPC287 chronology

The chronology for core TPC287 was constructed by aligning the downcore MS records in cores TPC287 and TPC288 (Figure 3.3). TPC287 is located approximately 150 km southeast of TPC287 (Figure 3.1) and thus the MS variations in both cores are expected to occur synchronously across glacial and interglacial cycles. The two MS records were graphically aligned used the AnalySeries software (Paillard et al. 1996) by choosing prominent features as tiepoints (Figure 3.3 & Table 3.4).

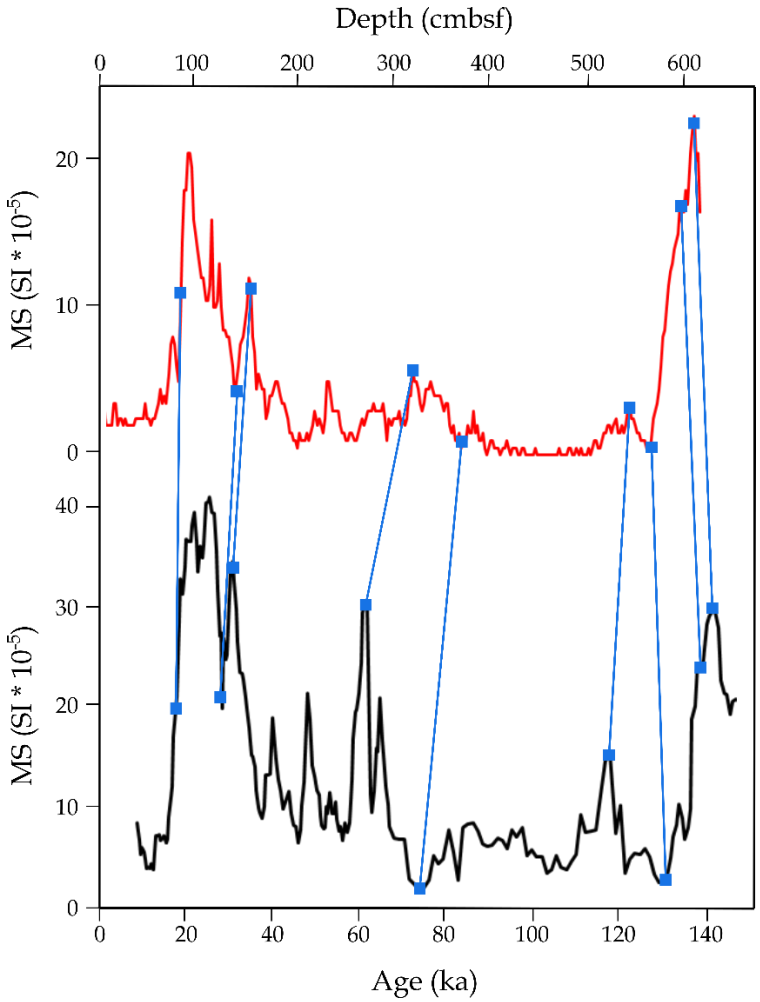

Figure 3.3 Alignment between the MS downcore records from cores TPC287 (red) and TPC288 (black) using the AnalySeries software (Paillard et al. 1996). The blue squares and connecting lines mark tiepoints between the records. The age model for core TPC288 was published by Pugh et al. (2009).

TPC287 depth (mbsf)	TPC288 age (ka)
0.84	17.5
1.39	28.5
1.53	31
3.21	61
3.71	75
5.43	118
5.65	129.5
5.95	137
6.09	142

Table 3.4 Tiepoints for the TPC287 chronology with depths for core TPC287 being tied to the EDC3 ages published by Pugh et al. (2009) for core TPC288.

3.3.3 PC509 chronology

The chronology for core PC509 was constructed by visually aligning the wet bulk density (WBD), a proxy mirroring biogenic opal content (Busch 1991, Weber et al. 1997, Hillenbrand et al. 2009), to the LR04 benthic foraminifera $\delta^{18}O$ stack (Lisiecki & Raymo 2005) using the AnalySeries software (Paillard et al. 1996). Tiepoints were selected in the WBD record at MIS stage and sub-stage boundaries (Table 3.5 & Figure 3.4). The MIS 5 sub-stages use the age assignments from Govin et al. (2009) and the ages are translated across from the LR04 chronology to the EDC3 chronology using the conversion tables published by Parrenin et al. (2013b).

PC509 depth (mbsf)	LR04 age (ka)	MIS stage/sub-stage boundary
5.00	73	4-5a
5.20	84	5a-5b
5.64	91	5b-5c
5.78	106	5c-5d
5.97	116	5d-5e
6.38	130	5e-6
6.48	136	-

Table 3.5 Tiepoints for the PC509 chronology. The WBD record for PC509 was aligned with the LR04 benthic stack using the AnalySeries software (Paillard et al. 1996). The ages for MIS stage/sub-stage boundaries used as tiepoint are listed.

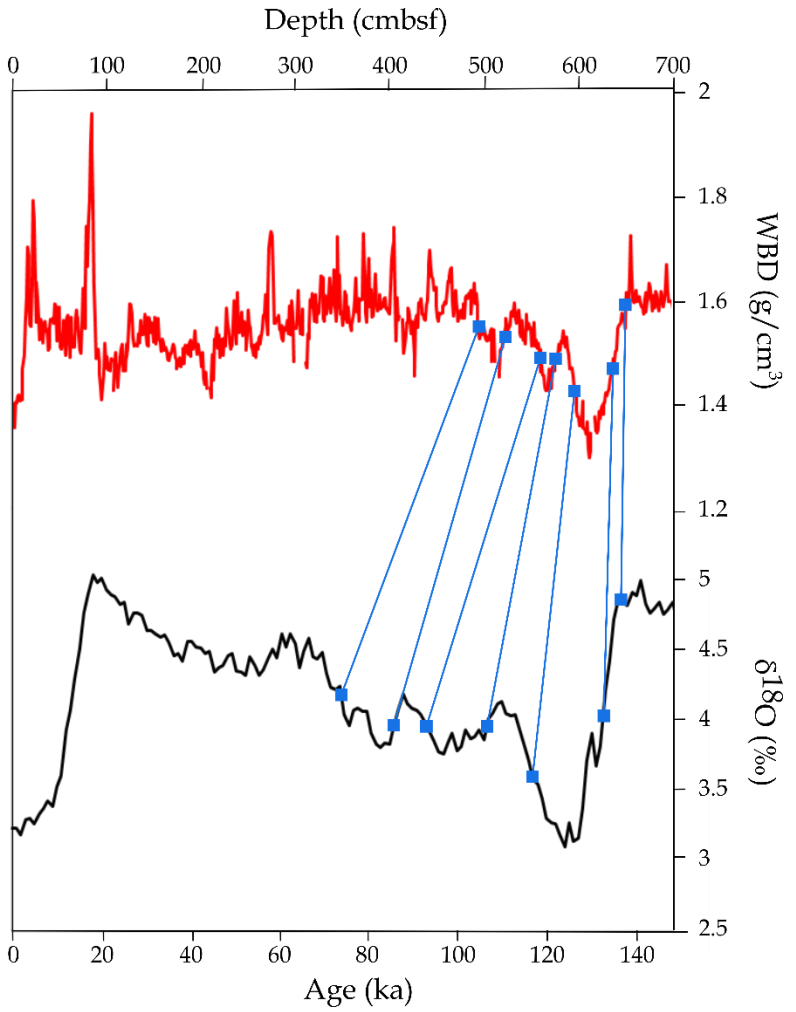

Figure 3.4 Alignment between the downcore WBD record of core PC509 (red) and the LR04 benthic $\delta^{18}O$ stack (black) using the AnalySeries software (Paillard et al. 1996). The tiepoints are marked by blue squares and connecting lines.

3.4 Results and discussion

3.4.1 MIS 5e diatom assemblages

Relative diatom abundances in the sediments deposited during the time interval 132-120 ka are presented for all seven core sites (Figure 3.5, 3.6 & 3.7) in order to capture the palaeoenvironmental signal from the end of the Termination II deglaciation and during the 'peak' MIS 5e. The *Azpeitia tabularis* and *Actinocyclus actinochilus* abundances are low in all seven cores (0.3 ± 0.4 % and 0.5 ± 0.6 %) with cores TPC288, ELT17-9 and PC509 recording only negligible contributions (0.3 ± 0.3 %) of either species (Figures 3.5, 3.6 & 3.7). Core TPC287 has the largest 'cold signal' (Table 3.2), with an *A. actinochilus* peak of 2 % at 120 ± 2.7 ka (Figure 3.5), and core TPC290 has the greatest 'warm signal' (Table 3.2), with high *A. tabularis* abundances of 1.8 ± 0.7 % and 2.0 ± 0.4 % from 126-124

ka and 121-120 ka respectively (Figure 3.5). Core NBP9802-04 also has a strong 'warm signal' with *A. tabularis* being present almost throughout MIS 5e (Figure 3.7).

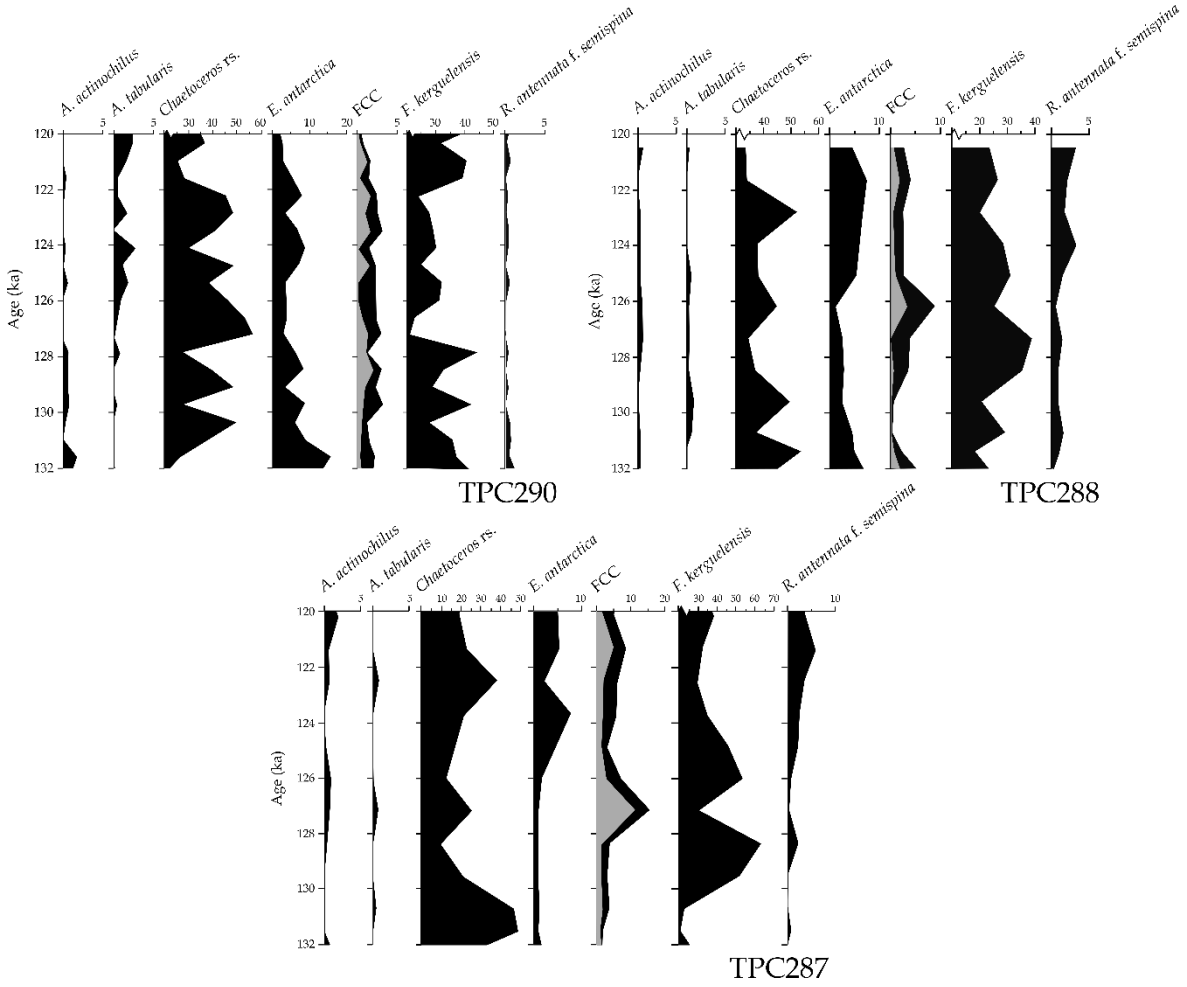

Figure 3.5 Downcore diatom relative abundances for the three Atlantic sector cores (TPC290, TPC288 and TPC287) covering the 132-120 ka period. For the FCC group, the grey shading shows the *F. cylindrus* abundance and the black shading shows the *F. curta* abundance.

The highest MIS 5e *Chaetoceros* rs. abundances occur in core PC509 (78 ± 4 %). This is likely due to its proximity to the Antarctic Peninsula where high meltwater stratification and nutrient availability promote extensive *Chaetoceros* rs. blooms (Crosta et al. 1997). The three Atlantic sector cores (TPC290, TPC288 and TPC287) are dominated by both *Chaetoceros* rs. (38 ± 10 %, 40 ± 8 % and 28 ± 11 %, respectively) and *F. kerguelensis* (34 ± 8 %, 27 ± 6 % and 33 ± 12 %, respectively) throughout MIS 5e, with peaks in one group coinciding with troughs in the other (Figure 3.5). This alternation is particularly evident in core TPC287 where *Chaetoceros* rs. relative abundance declined by ~40 % after 131 ± 2.6 ka concurrent with an equivalent increase in *F. kerguelensis* relative abundance (Figure 3.5). Both TPC288 and TPC287 have similar *F. kerguelensis* abundance profiles with higher values of 34 ± 4 % and 53 ± 6 %, respectively, between 130-127 ka and 126-124 ka (Figure 3.5). This contrasts with core TPC290 where the *F. kerguelensis* abundance is lowest (27 ± 4 %) from 128-122

ka (Figure 3.5). Consistent with the modern distribution pattern in Crosta et al. (1997), the Indian and central Pacific sector cores (ELT17-9, NBP9802-04 and MD03-2603) have low *Chaetoceros* rs. abundances (10 ± 2 %, 5 ± 2 % and 17 ± 5 %, respectively) during MIS 5e and are dominated instead by *F. kerguelensis* (63 ± 4 %, 74 ± 4 % and 59 ± 8 %, respectively) (Figures 3.6 & 3.7).

The FCC abundances in cores TPC288 and TPC287 are very similar with minima (0.3 % and 1 %) early in the 132-120 ka interval followed by an increase to maxima of ~9 % and ~15 %, respectively, at ~127-126 ka before decreasing to largely steady abundances of ~3 % and ~6 %, respectively, between 125-120 ka (Figure 3.5). In contrast, the FCC abundances in core TPC290 remain largely consistent at 2.3 ± 0.7 % from 130 to 124 ka before gradually declining to a minimum of ~0.6 % at 120 ± 2.6 ka (Figure 3.5). In the Pacific sector cores (ELT17-9, NBP9802-04 and PC509), the FCC abundances are largely uniform throughout MIS 5e, at ~2 %, ~3.5 % and ~6 % respectively (Figure 3.7). Cores ELT17-9 and NBP9802-04 reach a FCC abundance minimum of ~0.9 % at ~124 ka, whereas the minimum (4.5 %) in PC509 occurs earlier at ~129 ± 2.6 ka, consistent with the more southerly Atlantic sector cores (TPC288 and TPC287) (Figures 3.5 & 3.7). Core MD03-2603 also has a largely constant FCC abundance of ~3.5 % throughout MIS 5e, although it reaches minima of 1.7 % at ~130.5 ± 2.6 ka and 2.2 % at ~127.5 ± 2.6 ka, both of which are concurrent with *A. tabularis* abundance peaks of >1 % (Figure 3.6).

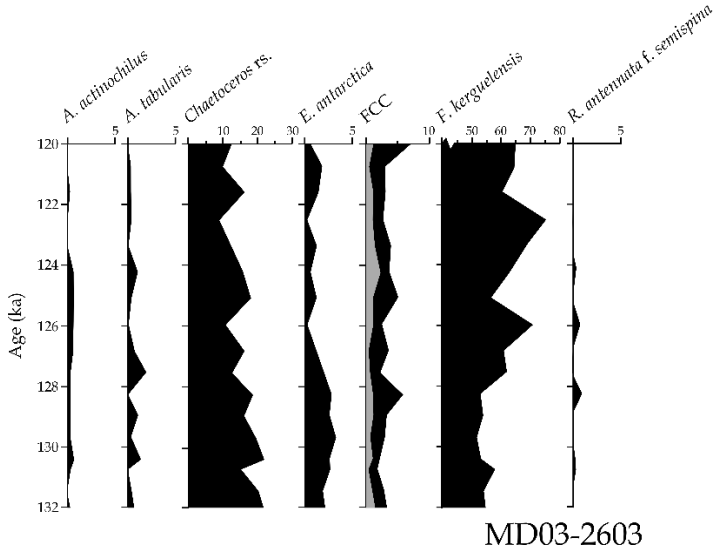

Figure 3.6 Downcore diatom relative abundances for the Indian sector core (MD03-2603) covering the 132-120 ka period. For the FCC group, the grey shading shows the *F. cylindrus* abundance and the black shading shows the *F. curta* abundance.

The *Eucampia antarctica* and *Rhizosolenia antennata* f. *semispina* abundances in TPC288 and TPC287 show coincident increases after 126 ± 2.6 ka (Figure 3.5). This pattern is not seen in TPC290 where the *R. antennata* f. *semispina* abundance remains low (0.3 ± 0.4 %) throughout MIS 5e and the highest *E. antarctica* abundances (>10 %) are observed before 131 ± 2.6 ka (Figure 3.5). In the

four Indian and Pacific sector cores both *R. antennata* f. *semispina* and *E. antarctica* have low abundances (<5 %) throughout the 132-120 ka interval (Figures 3.6 & 3.7).

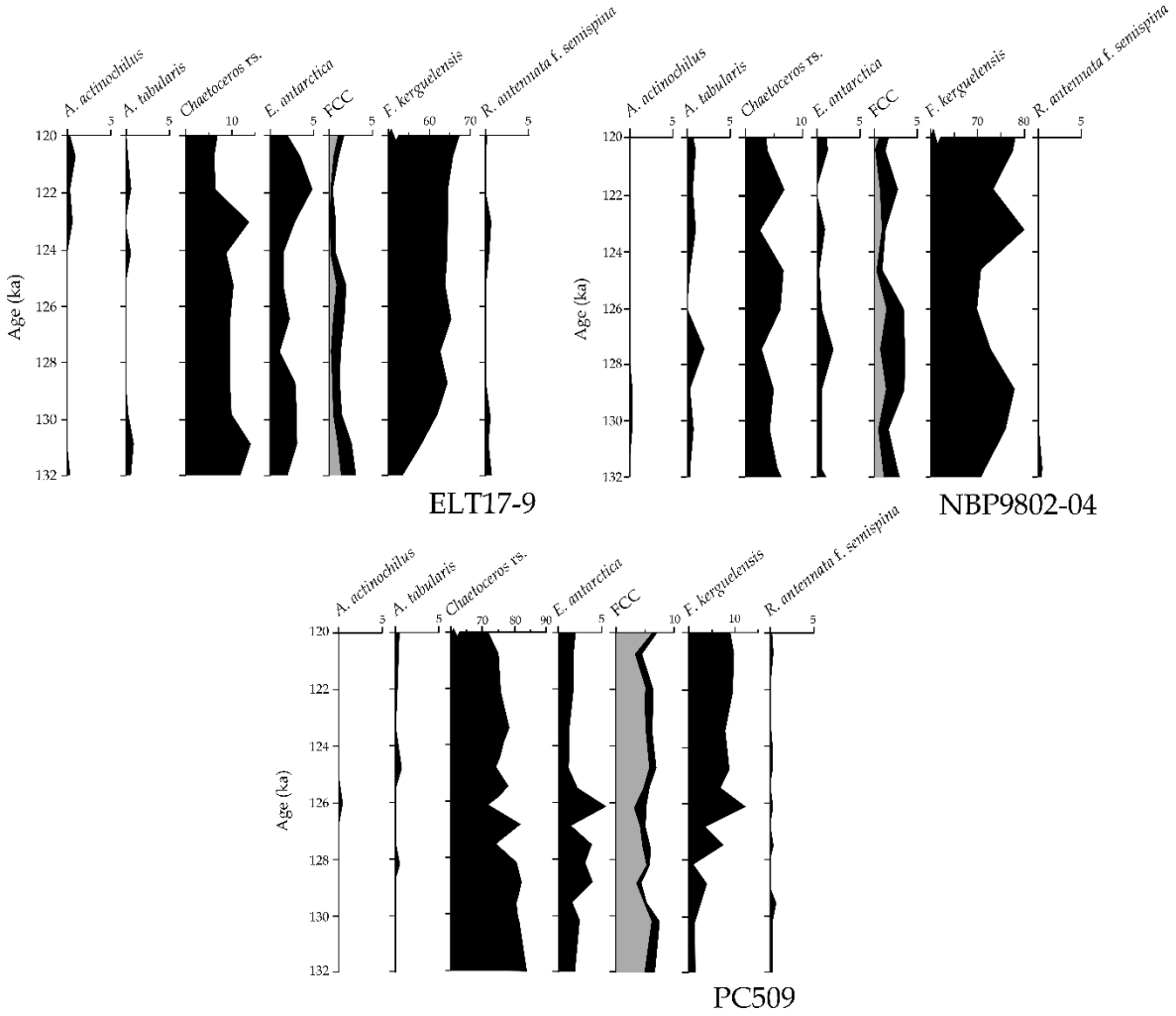

Figure 3.7 Downcore diatom relative abundances for the three Pacific sector cores (ELT17-9, NBP9802-04 and PC509) covering the 132-120 ka period. For the FCC group, the grey shading shows the *F. cylindrus* abundance and the black shading shows the *F. curta* abundance.

3.4.2 Comparison of MIS 5e to surface sediments

The diatom abundances in the surface sediments are compared with the average abundances in three MIS 5e time slices – early (132-130 ka), mid (130-125 ka) and late (125-120 ka) (Table 3.6). These MIS 5e time windows are chosen to get average palaeoenvironmental conditions for; the end of the deglaciation, the peak of MIS 5e and the later stage of MIS 5e, respectively, thereby following the divisions suggested by Capron et al. (2014). To ensure there are data from at least 3 samples averaged for each MIS 5e time slice, 1 sample older than 132 ka had to be included in the 132-130 ka window for five of the cores (TPC288, TPC287, ELT17-9, NBP9802-04 and PC509). Figures 3.8, 3.9, 3.10 & 3.11 show the differences in spatial and temporal relative abundances for four of the key groups (*Chaetoceros* rs., *E. antarctica*, FCC, *F. kerguelensis*) in the three MIS 5e intervals and

the modern surface sediments. Diatom assemblages in the surface sediments are consistent with the modern environmental setting.

A. actinochilus and *A. tabularis* have similar, but opposing, offsets (~1-2 %) between the surface sediments and the MIS 5e intervals in all the cores (Table 3.6). The higher (lower) *A. tabularis* (*A. actinochilus*) abundances during MIS 5e than in the surface sediments supports the warmer than present conditions expected during MIS 5e (Capron et al. 2014). Care should be taken when interpreting such small changes in species abundance. But because both *A. actinochilus* and *A. tabularis* occur in very low abundances (<3-5 %) throughout the Antarctic Zone of the SO (Armand et al. 2005, Romero et al. 2005, Esper et al. 2010), even small variations in their relative abundances, especially across multiple downcore sediment samples, can indicate substantial environmental shifts.

Most of the cores have largely similar *Chaetoceros* rs. abundances across all three MIS 5e time slices and in the surface sediments. Core site TPC287 is a clear exception, with a decrease of >20 % between the early MIS 5e (42.5 %) and the mid and late MIS 5e (17.2 % and 23.4 % respectively) (Figure 3.8). The modern *Chaetoceros* rs. abundance for TPC287 (33.3 %) is most similar to the early MIS 5e (42.5 %) but is ~10 % different from any of the MIS 5e time slices (Figure 3.8). The combined abundance of *F. kerguelensis* and *Chaetoceros* rs. in TPC287 is very similar between early and mid MIS 5e (65.8 % and 66.7 % respectively) indicating that the decrease in *Chaetoceros* rs. is almost exactly matched by an increase in *F. kerguelensis* (Figure 3.5). This transition from a *Chaetoceros* rs. dominated assemblage during early MIS 5e to a *F. kerguelensis* dominated one during mid and late MIS 5e is likely related to a change in the major oceanographic influence at this site. The stratified surface waters of the Weddell Gyre overlie core site TPC287 in the present (Vernet et al. 2019), and, combined with clockwise lateral transport of robust *Chaetoceros* rs. from the Antarctic Peninsula and Weddell Sea Embayment (Crosta et al. 1997) may have caused the high *Chaetoceros* rs. abundances in this core during early MIS 5e. A poleward shift of the northern boundary of the Weddell Gyre during MIS 5e, as indicated by multiple CMIP3 and CMIP5 models under a warmer than present climate (Meijers et al. 2012, Wang 2013), and the accompanying southerly displacement in surface water masses, would result in the replacement of high *Chaetoceros* rs. abundances with high *F. kerguelensis* abundances, indicative of open ocean conditions (Hasle 1969, Cefarelli et al. 2010). A reduction in the longitudinal extent of the Weddell Gyre during MIS 5e is supported by other core records from the SW Indian sector (Ghadi et al. 2020). The Indian and Pacific sector cores show similar *F. kerguelensis* abundance patterns with increasing abundances in the mid and late MIS 5e (Figure 3.11). All cores for which a surface sample is available have greater *F. kerguelensis* abundances during mid and late MIS 5e than in the surface sediments (Figure 3.11), indicating increased open ocean conditions during MIS 5e.

		A. actinochilus	*A. tabularis*	*Chaetoceros* rs.	*E. antarctica*	FCC	*F. kerguelensis*	*R. antennata* f. *semispina*
TPC290	Early MIS 5e	0.7	0.0	38.6	10.1	1.6	33.4	0.5
	Mid MIS 5e	0.4	0.5	42.5	5.0	2.5	31.9	0.2
	Late MIS 5e	0.1	1.2	38.1	5.5	2.0	30.7	0.2
	Modern	0.0	0.0	46.8	6.6	7.6	20.8	0.7
TPC288	Early MIS 5e	0.3	0.2	45.2	5.5	2.6	23.8	0.9
	Mid MIS 5e	0.4	0.5	40.9	3.0	3.9	30.2	0.8
	Late MIS 5e	0.3	0.1	39.4	6.2	3.0	24.7	2.4
	Modern	0.6	0.0	39.0	3.4	5.3	23.9	7.8
TPC287	Early MIS 5e	0.2	0.1	42.5	1.3	2.2	23.3	0.6
	Mid MIS 5e	0.5	0.2	17.2	1.2	7.2	49.5	0.9
	Late MIS 5e	0.7	0.1	23.4	5.1	5.8	37.0	3.6
	Modern	1.0	0.3	33.3	2.6	14.0	16.6	6.2
ELT17-9	Early MIS 5e	0.1	0.6	12.0	2.8	2.4	57.9	0.2
	Mid MIS 5e	0.0	0.0	9.7	2.1	1.6	64.1	0.3
	Late MIS 5e	0.5	0.4	8.8	3.3	0.8	64.9	0.3
NBP9802-04	Early MIS 5e	0.1	0.4	6.2	1.4	2.7	71.8	0.1
	Mid MIS 5e	0.1	0.8	4.6	1.1	3.4	73.5	0.0
	Late MIS 5e	0.0	0.7	4.9	0.6	1.6	75.3	0.0
MD03-2603	Early MIS 5e	0.3	0.6	19.1	2.4	2.2	55.1	0.2
	Mid MIS 5e	0.5	0.6	16.1	2.0	3.5	58.4	0.2
	Late MIS 5e	0.2	0.4	12.6	1.1	3.2	66.3	0.1
	Modern [a]	0.7	0.7	12.5	1.0	4.8	56.1	0.3
PC509	Early MIS 5e	0.0	0.0	82.9	2.2	7.0	1.5	0.3
	Mid MIS 5e	0.1	0.1	78.6	3.0	5.4	5.5	0.2
	Late MIS 5e	0.0	0.3	76.0	1.5	6.1	9.1	0.3
	Modern	0.0	0.0	73.5	2.0	7.8	5.1	0.0

Table 3.6 Mean abundances for the three MIS 5e time slices (early = 132*-130 ka; mid = 130-125 ka; late = 125-120 ka) in each core site and the modern abundances from surface sediments. *The early MIS 5e time slice includes samples older than 132 ka in five of the cores (TPC288, TPC287, ELT17-9, NBP9802-04 and PC509). [a] modern abundances for core MD03-2603 are from the surface sediments at IODP Site U1361.

Consistent with the evidence of increased open ocean conditions during MIS 5e, the MIS 5e FCC abundances, in all core sites with surface sediment assemblages, indicate a reduced WSIE relative to the surface sediments (Figure 3.10). All three Atlantic cores share similar patterns of FCC abundances, with the lowest abundances occurring during early MIS 5e (average 2.1 %) followed by an increase during mid MIS 5e (average 4.5 %) and subsequent decrease during late MIS 5e (average 3.6 %) (Figure 3.10). The amplitude of these abundance changes exhibits a N-S trend with the highest amplitude shifts at the most southerly site (TPC287) and the least variation at the northernmost site (TPC290). The FCC abundances in core PC509 are consistently >3 % throughout MIS 5e which indicates that the site was located to the south of the mean WSIE for the entire 132-120 ka period (Figure 3.7). The two central Pacific sector cores (ELT17-9 and NBP9802-04) do not have surface sediment assemblages to compare with. However, the FCC abundances (Figure 3.7) suggest that during MIS 5e, site ELT17-9 (FCC ~1-2 %) was located on the edges of the maximum WSIE and site NBP9802-04 (FCC ~3 %) was located near the mean WSIE until 126 ± 2.7 ka, when the winter sea-ice limit retreated. Compared to the modern September sea-ice extent (Figures 3.1 & 3.10), the FCC abundances (Figure 3.10) indicate a southward shift in sea-ice cover for the central Pacific sector during MIS 5e. FCC abundances in core MD03-2603 show strong similarity between the mid and late MIS 5e intervals and the surface sediments (Figure 3.10). The greater WSIE reduction in the Atlantic sector compared to the Pacific and Indian sectors supports the pattern of the simulated MIS 5e WSIE minimum in Holloway et al. (2017).

The *E. antarctica* abundances are highest in cores TPC290 and TPC288 (5.5 % and 5.8 % respectively), whilst the Indian and Pacific sector cores have low abundances throughout MIS 5e (average 2.6 %) and the modern (average 1.5 %) (Figure 3.9). Higher *E. antarctica* abundances in the Atlantic sector cores when compared to the Pacific and Indian sector cores (Figure 3.9), are likely linked to greater influence of iceberg flux from the Weddell Sea than the other Antarctic embayments (Burckle 1984, Allen 2014, Death et al. 2014). The high *E. antarctica* abundances for the early MIS 5e interval in cores TPC290 and TPC288, when compared to surface sediments (Table 3.6 & Figure 3.9), suggest a higher iceberg supply during the deglaciation, which is supported by high accumulation rates of iceberg-rafted debris during this time recorded in Weddell Sea cores from the East Antarctic margin (Diekmann et al. 2003). During the late MIS 5e interval the high *E. antarctica* abundances (6.2 % and 5.1 %, respectively) in cores TPC288 and TPC287 indicate a later period of substantial iceberg flux, which could reflect a poleward migration and/or expansion of the iceberg tracks over the course of MIS 5e. A poleward displacement of the iceberg tracks would support a contraction of the Weddell Gyre (Tournadre et al. 2016) and suggests a southerly shift in the position of the ACC and wind fields (Gladstone et al. 2001). Present day iceberg trajectories support the greater *E. antarctica* abundance in the surface sediment assemblage of core TPC290

when compared with the *E. antarctica* abundance in surface sediment assemblages of cores TPC288 and TPC287 (Silva et al. 2006).

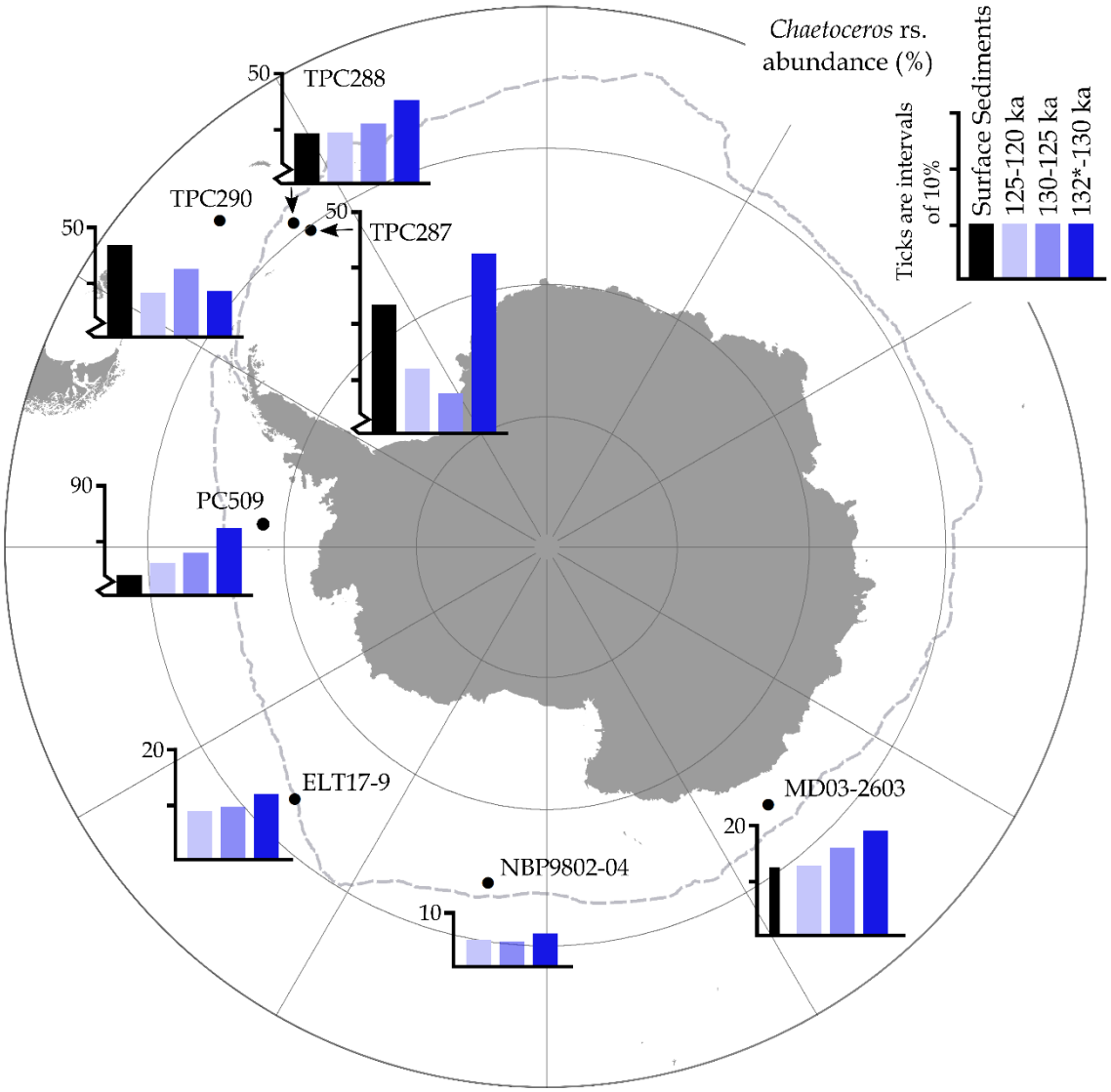

Figure 3.8 Map of *Chaetoceros* rs. abundances in seven marine sediment cores. Modern diatom abundances are marked by black bars and mean abundances during three MIS 5e time slices (early = 132*-130 ka; mid = 130-125 ka; late = 125-120 ka) are indicated by bars with different shades of blue. The thin black bar on the MD03-2603 graph indicates diatom abundances in the surface sediment samples from the nearby IODP Site U1361. The black dots mark the core locations and the grey dashed line is the median modern (1981-2010) September sea-ice extent from Fetterer et al. (2017). * the 132-130 ka time slice includes some samples older than 132 ka in five of the core sites to ensure at that least three samples are included in the average.

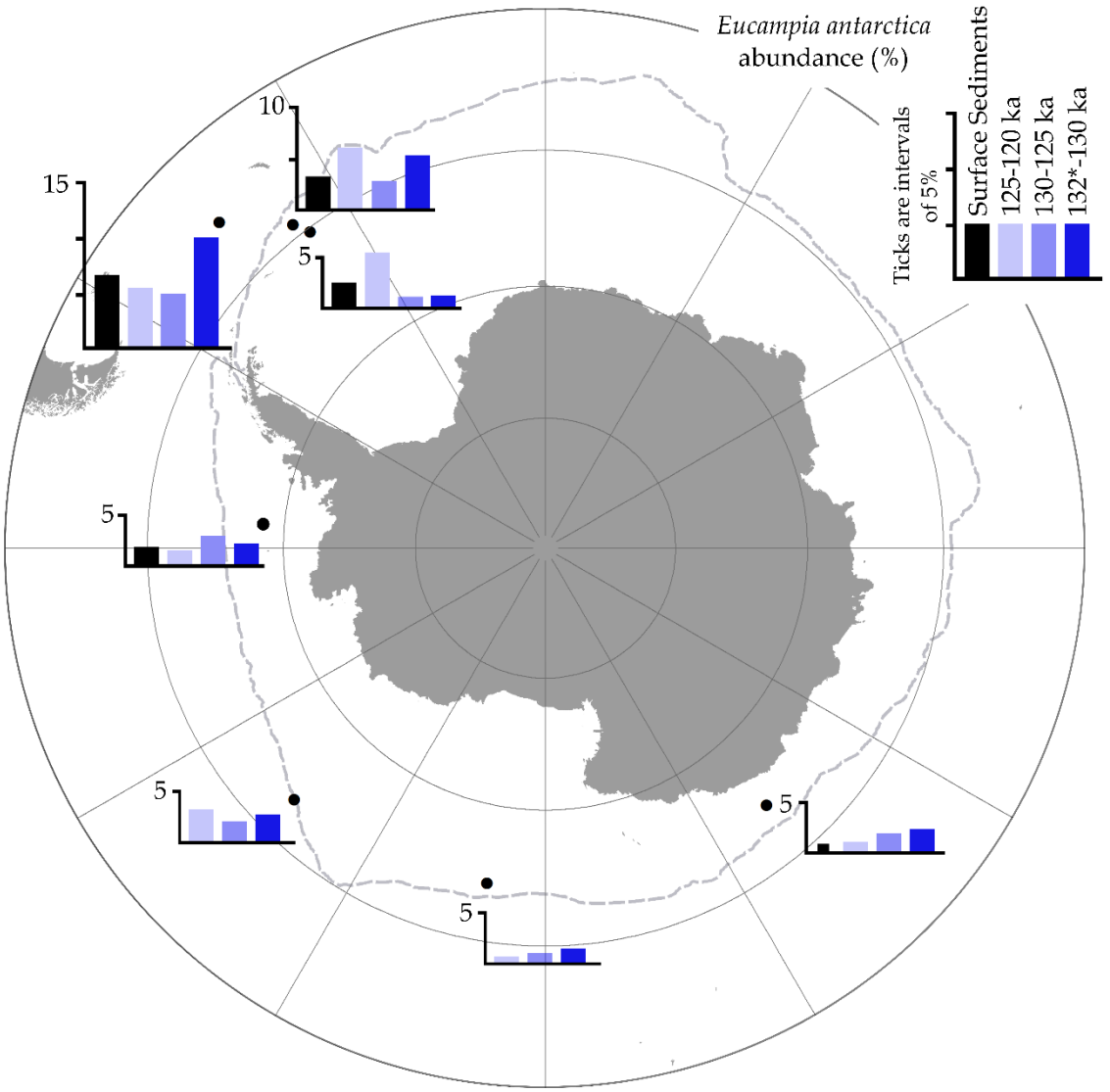

Figure 3.9 Map of *Eucampia antarctica* abundances in seven marine sediment cores. Modern diatom abundances are marked by black bars and mean abundances during three MIS 5e time slices (early = 132*-130 ka; mid = 130-125 ka; late = 125-120 ka) are indicated by bars with different shades of blue. The thin black bar on the MD03-2603 graph indicates diatom abundances in the surface sediment samples from the nearby IODP Site U1361. The black dots mark the core locations and the grey dashed line is the median modern (1981-2010) September sea-ice extent from Fetterer et al. (2017). * the 132-130 ka time slice includes some samples older than 132 ka in five of the core sites to ensure that at least three samples are included in the average.

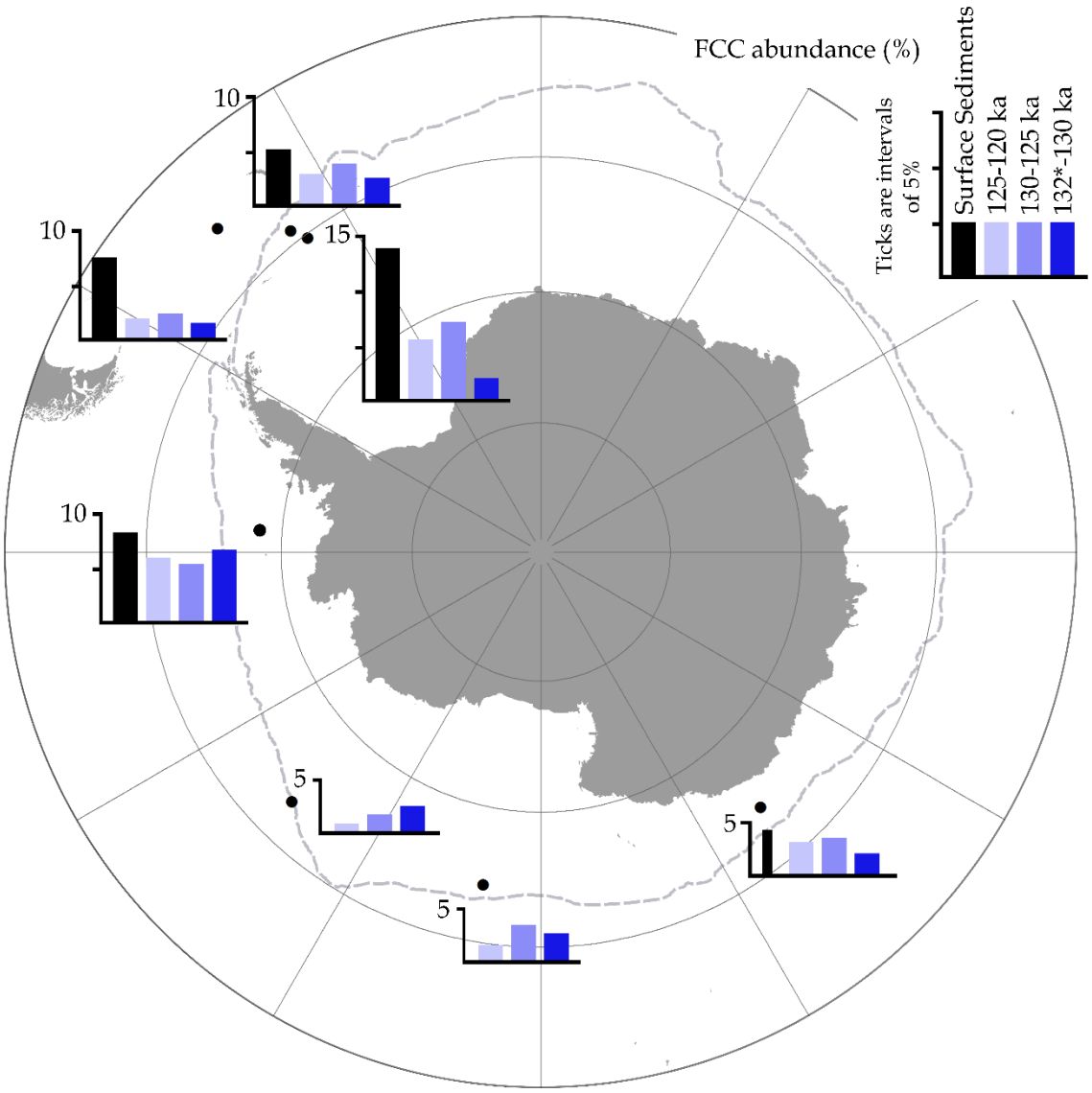

Figure 3.10 Map of FCC abundances in seven marine sediment cores. Modern diatom abundances are marked by black bars and mean abundances during three MIS 5e time slices (early = 132*-130 ka; mid = 130-125 ka; late = 125-120 ka) are indicated by bars with different shades of blue. The thin black bar on the MD03-2603 graph indicates diatom abundances in the surface sediment samples from the nearby IODP Site U1361. The black dots mark the core locations and the grey dashed line is the median modern (1981-2010) September sea-ice extent from Fetterer et al. (2017). * the 132-130 ka time slice includes some samples older than 132 ka in five of the core sites to ensure that at least three samples are included in the average.

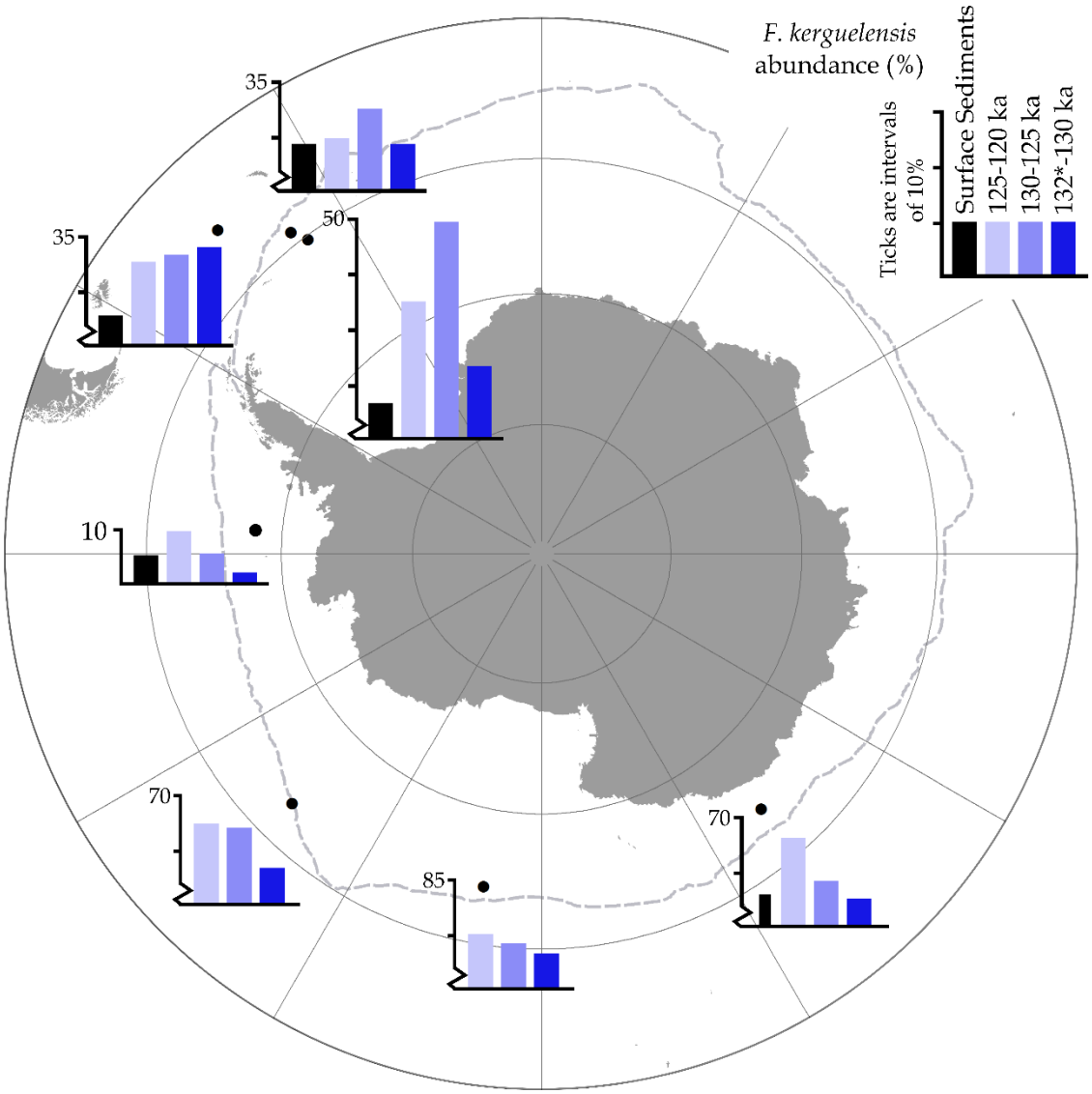

Figure 3.11 Map of *F. kerguelensis* abundances in seven marine sediment cores. Modern diatom abundances are marked by black bars and mean abundances during three MIS 5e time slices (early = 132*-130 ka; mid = 130-125 ka; late = 125-120 ka) are indicated by bars with different shades of blue. Thin black bars on the MD03-2603 graphs indicate diatom abundances in the surface sediment samples from the nearby IODP Site U1361. The black dots mark the core locations and the grey dashed line is the median modern (1981-2010) September sea-ice extent from Fetterer et al. (2017). * the 132-130 ka time slice includes some samples older than 132 ka in five of the core sites to ensure that at least three samples are included in the average.

3.4.3 Environmental heterogeneity during MIS 5e

Peaks in *A. tabularis* abundance (~2 %) at ~127.5 ka in cores MD03-2603 and NBP9802-04 (Figures 3.6 & 3.7) and the increased *A. tabularis* abundance between 126-124 ka and 121-120 ka in core TPC290 (Figure 3.5) could be related to higher SSTs and a more southerly Polar Front than the modern. Poleward migration of the Polar Front in the Atlantic sector during MIS 5e has been

concluded from previously published proxy reconstructions (Nürnberg et al. 1997, Bianchi & Gersonde 2002, Howe et al. 2002, Kemp et al. 2010, Chadwick et al. 2020). Unlike NBP9802-04 and MD03-2603, the ELT17-9 and PC509 records have very low *A. tabularis* abundances throughout MIS 5e (Figure 3.7) which suggests that, if there was a southerly migration in the Polar Front during MIS 5e, it did not occur homogenously across the Pacific and Indian sectors. Heterogeneous frontal migration during MIS 5e is supported by Chadwick et al. (2020), and is also evident for the modern SO (Freeman et al. 2016). It could be caused by the 'pinning' of fronts by bathymetric features in some regions, which will impede their migration (Nghiem et al. 2016).

The higher *R. antennata* f. *semispina* abundances in the most southerly Atlantic cores (TPC288 and TPC287, Figure 3.5) during the interval 126-120 ka indicate that the edge of the mean WSIE was closer to both sites during this interval than during the rest of MIS 5e (Crosta et al. 2005) and also indicate increased surface meltwater stratification (Allen et al. 2005). This increased meltwater stratification could have resulted either from the annual melting at the mean WSIE (Armand & Leventer 2003) or the melting associated with high iceberg flux indicated by the elevated *E. antarctica* abundances (Figures 3.5 & 3.9), with the high global sea level after 126 ka (Kopp et al. 2013) supporting a large reduction in global land ice volume at this time. The abundances of *E. antarctica,* FCC and *R. antennata* f. *semispina* during MIS 5e document clear environmental differences between the largely stable conditions in the Pacific and Indian sectors (Figures 3.6 & 3.7) and the more variable conditions in the southerly Atlantic sector cores (TPC288 and TPC287, Figure 3.5). FCC abundances likely indicates an early (~130-129 ka) WSIE minimum at sites TPC288 and TPC287. This is consistent with the FCC records for cores MD03-2603 and PC509 (Figures 3.6 & 3.7) but the substantial re-expansion of WSIE at ~127-126 ka is only seen in the Atlantic sector records (Figure 3.5). In the Indian sector, the similarity between MIS 5e and surface sample FCC abundances in core MD03-2603 (Figure 3.10) could be due to the influence of an Australian-Antarctic Basin Gyre regulating the position of the WSIE along the Adélie Land margin in East Antarctica (McCartney & Donohue 2007, Carter et al. 2008).

3.5 Conclusions and wider implications

The early (~130 ± 2.6 ka) reduction in WSIE and increase in SSTs at the start of MIS 5e for the two most southerly Atlantic sector cores (TPC288 and TPC287, Figure 3.5), coupled with the indication of a poleward contraction of the Weddell Gyre have large implications for the region and further afield. The downwelling of dense water masses in the Weddell Sea is a key component in the formation of Antarctic Bottom Water (Orsi et al. 2002), which helps drive global ocean overturning circulation (Brix & Gerdes 2003). Reduced WSIE, with a winter sea-ice edge located further south than its modern position, resulted from less sea ice formation in coastal polynyas and from less

advection to the north by winds and subsequent Ekman transport. This, in turn, suggests less brine rejection which may lead to a subsequent decrease in the rates of deep and bottom water mass production along the Antarctic Coast as well as a warming of the abyssal waters (Bouttes et al. 2010, Ferrari et al. 2014, Marzocchi & Jansen 2019). Warmer surface and abyssal waters in the Weddell Sea would imply accelerated basal melting of ice shelves and increased grounding line retreat of marine terminating ice streams in the region, which in turn would induce substantial mass loss from the Antarctic ice sheets (Pollard & DeConto 2009, DeConto & Pollard 2016). This increased melting and ice sheet mass loss may account for the sea ice resurgence (Merino et al. 2018) and increased iceberg discharge (Liu et al. 2015) inferred from cores TPC288 and TPC287 after 127 ka (Figure 3.5). Surface water freshening from glacial meltwater input has also been linked to a reduction in the formation rates of Antarctic Bottom water, causing further warming of the abyssal ocean (Fogwill et al. 2015, Lago & England 2019).

The possible southerly shifts in the Polar Front near sites NBP9802-04 and MD03-2603 and the poleward contraction of the Weddell Gyre south of site TPC287 suggest a poleward migration of the ACC during MIS 5e, as previously discussed in Chapter 2.6.3. A more southerly ACC causes increased advection of relatively warm ACC water masses, such as Circumpolar Deep Water, onto the Antarctic continental shelf (Fogwill et al. 2014, Spence et al. 2017). These warm upwelling ACC water masses contribute to the melting of glacial ice (Hellmer et al. 2012), similar to what is observed today in the Amundsen-Bellingshausen Sea sectors of West Antarctica (Rignot et al. 2019). A southern shift of the ACC would also have caused a poleward movement of the precipitation field and storm tracks (Liu & Curry 2010). A poleward migration of the precipitation field near site MD03-2603 would result in drier conditions across Southern Australia (Saunders et al. 2012) as seen in the modern day (CSIRO 2018).

Warming and reduced WSIE in the Weddell Sea could also have a substantial impact on the SO biosphere. At present day, the Weddell Sea has the highest area-normalised primary productivity rates in the SO (Vernet et al. 2019). Reduced sea-ice extent and increased glacial meltwater during MIS 5e likely promoted greater primary productivity, as observed today (de Jong et al. 2012, Kahru et al. 2016). In contrast, Antarctic krill (*Euphausia superba*), a key trophic intermediary in the modern SO (Knox 2006), prefer lower temperature waters (Siegel & Watkins 2016, Atkinson et al. 2017). A repeat of warmer MIS 5e-like conditions in the future SO will therefore likely cause a substantial reduction in the habitat and abundances of Antarctic krill and impact the populations of megafauna that rely on them (Hill et al. 2013), as can be seen at present in the rapidly warming northern region of the West Antarctic Peninsula (Montes-Hugo et al. 2009). A WSIE reduction in the Weddell Sea like during MIS 5e, would also have damaging impacts for modern day sea-ice obligate species, e.g. Emperor Penguins (Jenouvrier et al. 2005).

The largely stable environmental conditions at the Pacific sector sites, especially ELT17-9, during MIS 5e (Figure 3.7) suggest that this region may be more resilient to future changes. This is consistent with the observations that modern WSIE in this region is strongly influenced by the topography and bathymetry through the pinning of fronts and currents (Nghiem et al. 2016). Greater stability of the WSIE in the Pacific sector would have resulted in protection of ice shelves, such as the Ross ice Shelf, and maintained their buttressing effect for grounded ice, similar to what is seen in present day Greenland (Walter et al. 2012). This could also have substantial implications for the stability of the West Antarctic Ice Sheet (WAIS) during MIS 5e, with no evidence in the PC509 record (Figure 3.7) of substantial glacial meltwater flux originating from glaciers draining the Bellingshausen Sea sector of the WAIS (Gardner et al. 2018).

It is clear that, similarly to the present day (Hobbs et al. 2016, Parkinson 2019); changes to the SO during MIS 5e were not spatially and temporally homogeneous. Some of the climatic variability during MIS 5e is due to the difference in the topographic characteristics and oceanographic conditions, with the stability in the Pacific and East Indian sectors likely due to bathymetry pinning and the stability of the Australian-Antarctic Basin gyre, respectively. This variation in the controls on and magnitude of changes in the Antarctic and SO climate system are important factors to be included into model simulations of future warming. MIS 5e is a valuable 'laboratory' for understanding how the Antarctic and SO region responds to a warmer climate, especially for regions like the Weddell Sea where climatic trends during MIS 5e diverge from what is observed in the present day (Purich et al. 2016, Parkinson 2019).

Chapter 4 Reconstructing Antarctic Winter Sea-ice Extent during MIS 5e

4.1 Introduction

The bulk of this chapter is presented in: Chadwick M., Allen C.S., Sime L.C., Crosta X. & Hillenbrand C.-D. 2022. Reconstructing Antarctic winter sea-ice extent during Marine Isotope Stage 5e. *Climate of the Past*, **18**: 129-146.

Following the qualitative reconstruction of Southern Ocean (SO) palaeoenvironmental conditions during MIS 5e in Chapter 3, this chapter presents quantitative estimates of September sea-ice concentrations (SIC) and summer sea-surface temperatures (SSSTs) from nine marine sediment cores. The quantitative reconstructions of winter sea-ice extent (WSIE) are obtained using a Modern Analog Technique (MAT) diatom transfer function and are compared to qualitative reconstructions of WSIE to answer the following questions:

- Did the minimum WSIE occur synchronously throughout the SO during MIS 5e?
- Was the WSIE minimum concurrent with the peak Antarctic air temperatures at 128 ka?
- Were the patterns in MIS 5e sea-ice change consistent between SO sectors?

4.2 Materials and methods

4.2.1 Core sites

The nine marine sediment cores (Figure 4.1) for which MIS 5e WSIE and SSSTs are reconstructed are detailed in Table 4.1. Eight of these cores are also detailed in Chapter 3, with core ANTA91-8 the additional record. These cores were all chosen as they contain >20 cm thick intervals of diatom-rich MIS 5e sediments and are located further south than almost all existing MIS 5e sea ice records (Figure 2.1).

Table 4.1 (next page) Details of the core location and recovery information for the nine marine sediment cores analysed in this chapter. Cores are ordered by sector (Atlantic-Indian-Pacific) and then latitude. *For each of the three TPC cores (TPC290, TPC288 and TPC287), the trigger core (TC) and piston core (PC) were spliced together to produce a composite record.

Core	Latitude (°S), Longitude (°E)	Water depth (m)	Cruise, Year	Ship	Core length (cm)
TPC290	55.55, -45.02	3826	JR48, 2000	*RRS James Clark Ross*	1179*
TPC288	59.14, -37.96	2864	JR48, 2000	*RRS James Clark Ross*	940*
TPC287	60.31, -36.65	1998	JR48, 2000	*RRS James Clark Ross*	615*
MD03-2603	64.28, 139.38	3320	MD130, 2003	*R/V Marion DuFresne II*	3033
U1361A	64.41, 143.89	3459	IODP Exp. 318, 2010	*JOIDES Resolution*	38800
ELT17-9	63.08, -135.12	4935	ELT17, 1965	*R/V Eltanin*	2018
NBP9802-04	64.20, -170.08	2696	PA9802, 1998	*RV/IB Nathaniel B. Palmer*	740
PC509	68.31, -86.03	3559	JR179, 2008	*RRS James Clark Ross*	989
ANTA91-8	70.78, 172.83	2383	ANTA91, 1990	*R/V Cariboo*	511

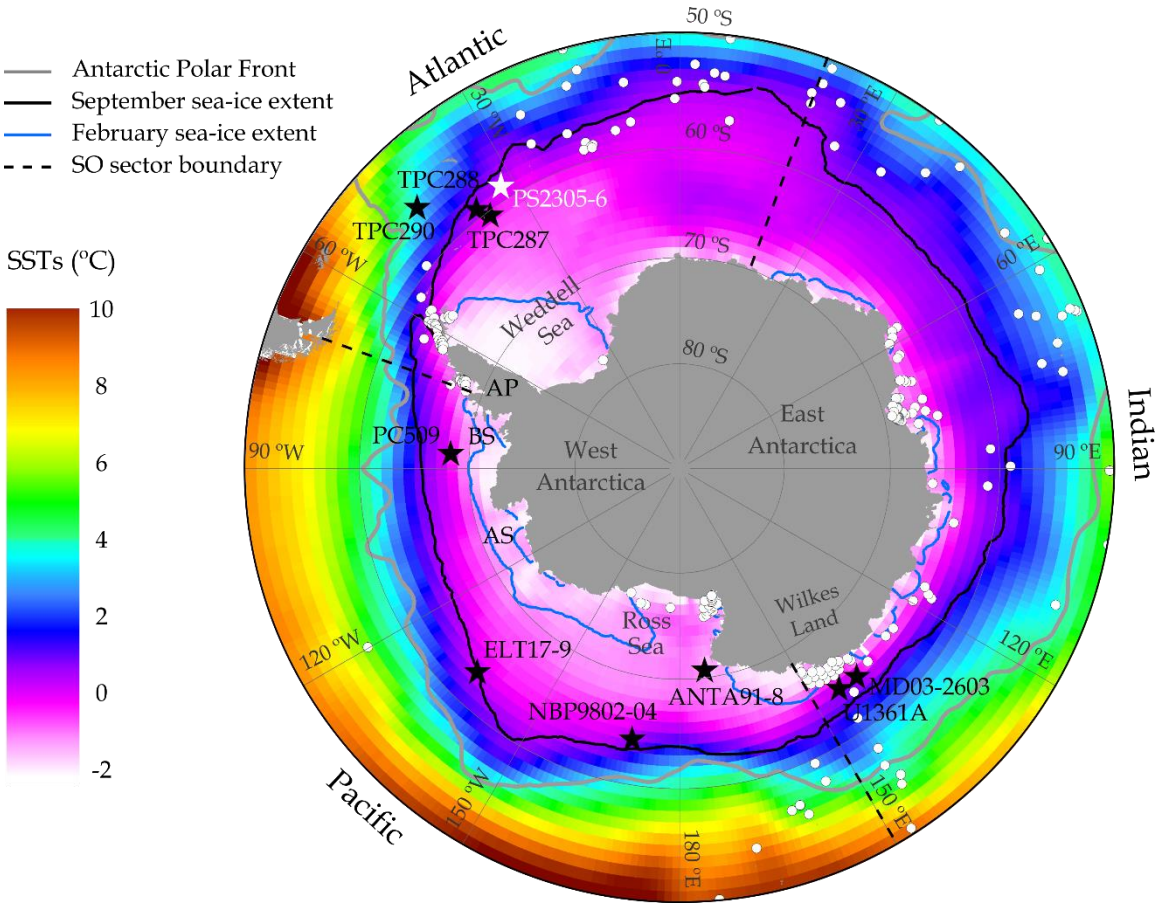

Figure 4.1 Map of core locations (black stars – this thesis, white star - Bianchi & Gersonde (2002)) with the modern (1981-2010) mean annual SSTs (COBE-SST2 dataset provided by the NOAA PSL, Boulder, Colorado, USA (https://psl.noaa.gov/)) and modern (1981-2010) median September and February sea-ice extents (data from Fetterer et al. (2017)). The black solid line is the September sea-ice extent (15 % cover) and the blue solid line is the February sea-ice extent (15 % cover). White dots mark the locations of surface sediment

samples (located south of 50 °S) used as a modern reference dataset for the Modern Analog Technique transfer function. The grey solid line is the position of the modern Antarctic Polar Front (Trathan et al. 2000). The black dashed lines mark the boundaries between the three SO sectors (Atlantic, Indian and Pacific). AP – Antarctic Peninsula, BS – Bellingshausen Sea, AS – Amundsen Sea.

4.2.2 Diatom counts

For the diatom assemblage data, microscope slides were produced and counted using the method detailed in Chapter 3.2.2. Complete MIS 5e diatom assemblage counts for all nine cores are available from the Polar Data Centre (Chadwick & Allen 2021a, b, c, d, e, f, g, h, i). The combined relative abundance of *Fragilariopsis curta* and *F. cylindrus* (FCC) is used as a qualitative indicator of winter sea-ice (WSI) presence (Gersonde & Zielinski 2000, Gersonde et al. 2005) (detailed in Chapter 1.3).

4.2.3 Modern Analog Technique (MAT)

September SICs and SSSTs (January to March) are estimated by applying the MAT transfer function to the MIS 5e diatom assemblages. The MAT compares the relative abundances of 33 diatom species in each MIS 5e sample to the abundances of the same species in a modern reference dataset composed of 257 surface sediment samples (modern analogs) from the SO (Figure 4.1). Modern conditions for each surface sediment sample are interpolated on a 1° x 1° grid, with SSSTs from the World Ocean Atlas 2013 (Locarnini et al. 2013) and September SIC from the numerical atlas of Schweitzer (1995). The MAT was implemented using the "bioindic" R-package (Guiot & de Vernal 2011), with chord distance used to select the 5 most similar modern analogs to each MIS 5e assemblage. A cut-off threshold, above which any analogs are deemed too dissimilar to the MIS 5e sample, is fixed as the first quartile of random distances determined by a Monte Carlo simulation of the reference dataset (Simpson 2007). The MAT257-33-5 (based on 257 reference samples, 33 taxa and up to 5 analogs) utilised in this thesis is an evolution of the MAT195-33-5 detailed in Crosta et al. (1998), with the addition of a further 62 surface sediment samples (Figure 4.1). The incremental evolutions of this transfer function over the last 20 years have yielded robust SST and sea-ice reconstructions when compared alongside other proxies within the same cores (Shemesh et al. 2002, Crosta et al. 2004, Nair et al. 2019, Ghadi et al. 2020, Civel-Mazens et al. 2021).

Quantitative estimates of September SIC and SSSTs are produced for each MIS 5e sample from a distance-weighted average of the climate values associated with the selected analogs. The reconstructed SSSTs have a Root Mean Square Error of Prediction (RMSEP) of 1.09 °C and an R^2 of 0.96, and the reconstructed September SIC have a RMSEP of 9 % and an R^2 of 0.93. The reconstructed September SIC and SSST for each MIS 5e sample only use analogs below the

dissimilarity threshold and therefore could be reconstructed from fewer than 5 analogs in some samples. It is also possible to get no-analog conditions, where none of the reference surface sediment samples are similar enough to a MIS 5e sample, and it is therefore not possible to reconstruct September SIC and SSST for this MIS 5e sample.

Core	SO sector	Chronology for MIS 5e	Chronological uncertainty (ka)
TPC290	Atlantic	Correlating MS from TPC290 to EDC ice core dust record combined with *C. davisiana* abundances (Pugh et al. 2009)*	± 2.58
TPC288	Atlantic	Correlating MS from TPC288 to EDC ice core dust record combined with *C. davisiana* abundances (Pugh et al. 2009)	± 2.59-2.64
TPC287	Atlantic	Correlating MS from TPC287 to MS from core TPC288 (Chapter 3.3.2, Figure 3.3)	± 2.57-2.65
MD03-2603	Indian	Correlating Ba/Al and Ba/Ti ratios from MD03-2603 to LR04 benthic oxygen isotope stack combined with diatom biostratigraphy (Presti et al. 2011)	± 2.55-2.56
U1361A	Indian	Correlating Ba/Al ratios and lithological changes to the LR04 benthic oxygen isotope stack combined with LOD *H. karstenii* (Wilson et al. 2018)	± 2.62-2.70
ELT17-9	Pacific	Combined abundance stratigraphies of *E. antarctica* and *C. davisiana* on SPECMAP age scale (Chase et al. 2003)	± 2.51
NBP9802-04	Pacific	Correlating MS from NBP9802-04 to EDC ice core dust record combined with LOD *H. karstenii* (Williams 2018)	± 2.68
PC509	Pacific	Correlating wet bulk density (= proxy mirroring biogenic opal content) from PC509 to the LR04 benthic oxygen isotope stack (Chapter 3.3.3, Figure 3.4)	± 2.59-2.65
ANTA91-8	Pacific	Correlating MS from ANTA91-8 to the LR04 benthic oxygen isotope stack combined with LCO *Rouxia leventerae* (Chapter 4.3.2, Figure 4.2)	± 2.60

Table 4.2 Summary of the location and chronologies for the nine sediment cores analysed in this chapter. Cores are ordered by sector (Atlantic-Indian-Pacific) and then latitude. LOD: Last Occurrence Datum, LCO: Last Common Occurrence. *For core TPC290 the chronology has been slightly adjusted from the published record of Pugh et al. (2009) by shifting the Termination II tiepoint to better align the magnetic susceptibility (MS) record with the dust record of the EDC ice core (Allen C.S. unpublished).

4.3 Age models

4.3.1 Published chronologies

Six of the sediment cores presented in this chapter have previously published age models, summarised in Table 4.2. Five of these chronologies are detailed in Chapter 3.3.1, with the addition of the chronology for IODP Hole U1361A, which is based on the correlation of sediment Ba/Al ratios

and lithological changes to the LR04 benthic foraminifera $\delta^{18}O$ stack, alongside the Last Occurrence Datum of *H. karstenii* (Wilson et al. 2018). The new chronologies for cores TPC287 and PC509 are detailed in Chapters 3.3.2 and 3.3.3, respectively, and all chronologies are translated onto the EDC3 chronology, as discussed in Chapter 3.3.1.

Chronological uncertainties for the MIS 5e ages of samples in this chapter are shown in Table 4.2 and are calculated as explained in Chapter 3.3.1.

4.3.2 ANTA91-8 chronology

The chronology for core ANTA91-8 was constructed by aligning the magnetic susceptibility (MS) to the LR04 benthic foraminifera $\delta^{18}O$ stack (Lisiecki & Raymo 2005) using the AnalySeries software (Paillard et al. 1996). Increased supply of terrigenous glacigenic detritus from the Antarctic continent to its margins and increased dust input from Patagonia and Australia to the pelagic SO during glacial periods resulted in higher MS values during glacial periods than interglacial periods (Bareille et al. 1994, Walter et al. 2000, Pugh et al. 2009). Tie points were selected in the MS record at the boundaries of MIS stages and sub-stages (Figure 4.2 & Table 4.3). Ages for the MIS 5 sub-stage boundaries are from Govin et al. (2009), and the ages are translated from the LR04 chronology onto the EDC3 chronology.

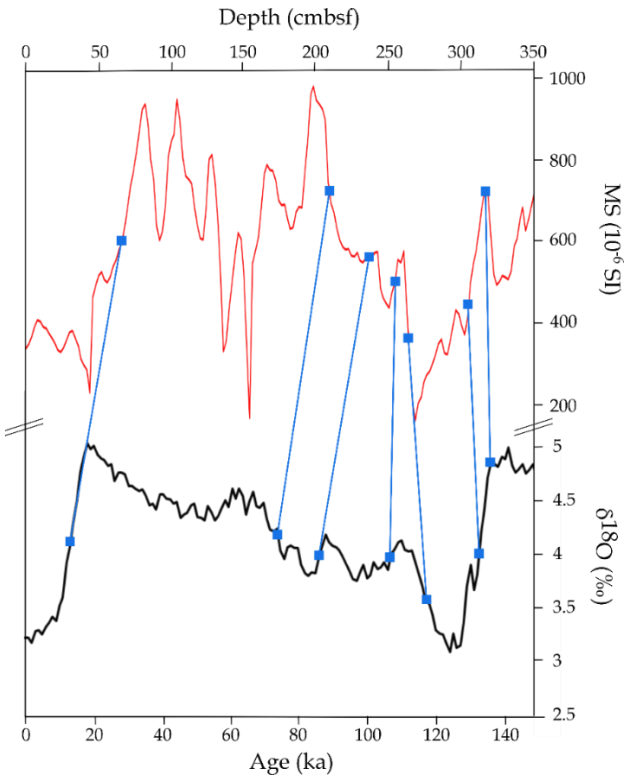

Figure 4.2 Alignment between the MS from core ANTA91-8 (red) and the LR04 benthic $\delta^{18}O$ stack (black) using the AnalySeries software (Paillard et al. 1996). Blue squares and connecting lines mark tiepoints between the records.

ANTA91-8 depth (mbsf)	LR04 age (ka)	MIS stage/sub-stage boundary
0.65	14	1-2
2.09	71	4-5a
2.39	83	5a-b
2.55	105	5c-d
2.65	116	5d-e
3.05	131.5	5e-6
3.17	136	-

Table 4.3 Tiepoints for ANTA91-8 chronology. The MS record for ANTA91-8 is aligned to the LR04 benthic stack using the AnalySeries software (Paillard et al. 1996).

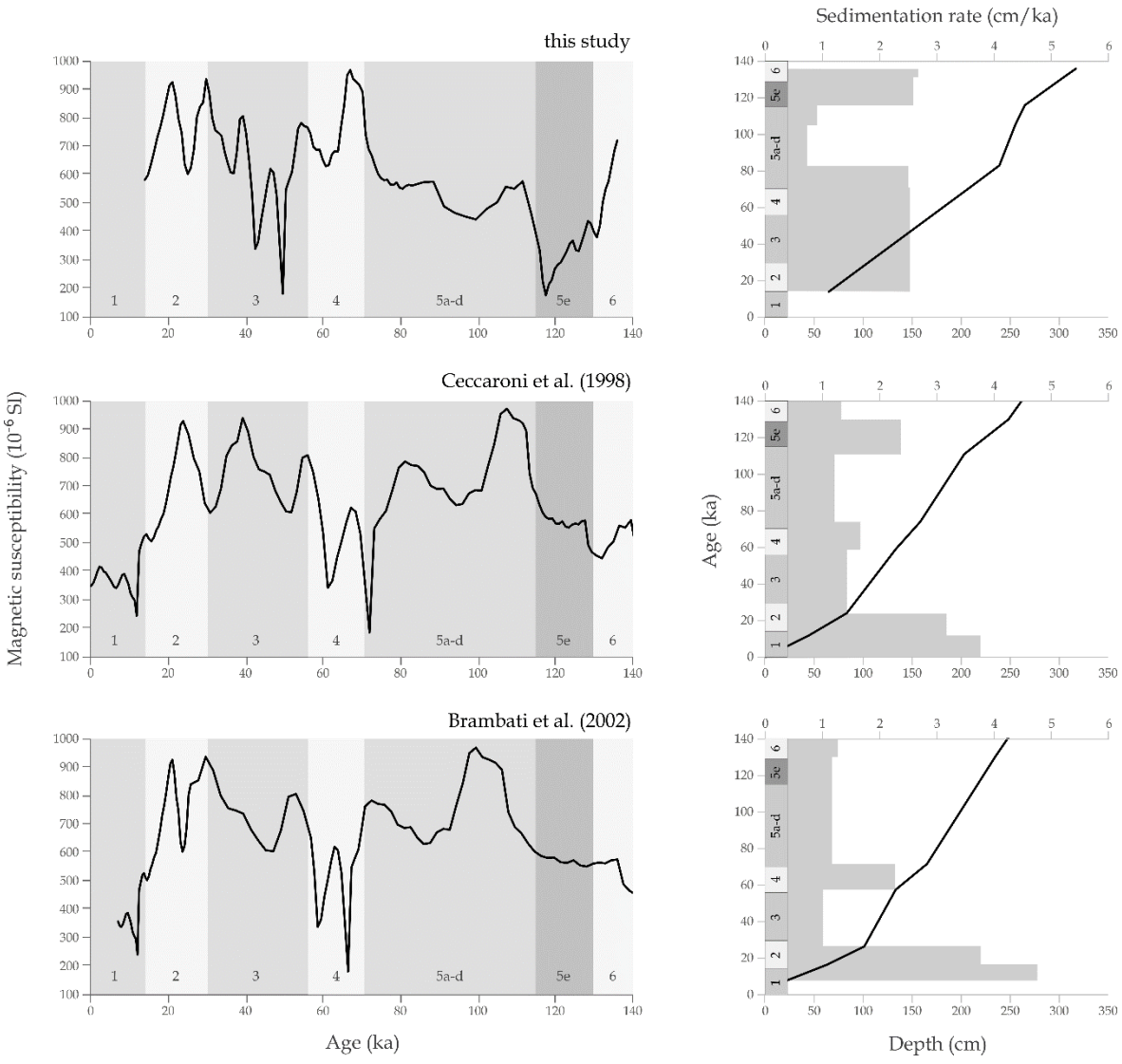

Figure 4.3 Graphs of MS against age (**LHS**) and age-depth plots (**RHS**) for the three alternative age models for core ANTA91-8. The top row is the age model detailed in Chapter 4.3.2, the middle row is the age model from Ceccaroni et al. (1998) and the bottom row is the age model from Brambati et al. (2002). The grey shading on the **RHS** plots indicate the sedimentation rates and MIS stages are shown along the y-axes. Grey background shading on the **LHS** graphs indicate the MIS stages.

The chronology for core ANTA91-8 presented here differs from chronologies previously published by Ceccaroni et al. (1998) and Brambati et al. (2002), who – on the basis of ^{230}Thorium measurements, subsequently adjusted by matching maxima in palaeo-productivity proxies to peak interglacials – placed MIS 5e ~50 cm higher than in my age model (Figure 4.3). My new chronology assigns the broad MS minimum from 2.65-3.05 mbsf, that comprises a peak in organic carbon content (Ceccaroni et al. 1998), to MIS 5e. In contrast, both the Ceccaroni et al. (1998) and Brambati et al. (2002) age models placed this MS minimum within MIS 6 (Figure 4.3), resulting in inexplicably high accumulation rates of productivity proxies during this glacial period (Ceccaroni et al. 1998). My new chronology is corroborated by the diatom species *Rouxia leventerae* which occurs in abundances <1 % in ANTA91-8 samples between 2.72 and 3.14 mbsf (Chadwick & Allen 2021a). If the sediments in this depth interval were deposited during MIS 6, as suggested by the Ceccaroni et al. (1998) and Brambati et al. (2002) age models, then the *R. leventerae* abundances in the corresponding samples should be >1 % (Zielinski et al. 2002).

4.4 Results

The September SIC values, reconstructed using the MAT transfer function, and the FCC relative abundances are presented for the 132-120 ka in all nine sediment cores (Figure 4.4). This interval is chosen to capture the sea-ice signature from both the end of glacial Termination II and during 'peak' MIS 5e. SSST data, also reconstructed using MAT, is presented over the same time interval alongside the cumulative relative abundance of the eight tropical/subtropical diatom species and groups according to Romero et al. (2005) (Figure 4.5).

4.4.1 Sea ice

In the Atlantic sector, the three cores (TPC290, TPC288 and TPC287) display a N-S increasing trend in mean FCC relative abundances (2.1 ± 0.7 %, 3.1 ± 2.2 % and 4.7 ± 3.6 %) and Sept. SICs (19 ± 17 %, 25 ± 18 % and 33 ± 20 %). All three cores have low FCC relative abundances (1.2 ± 0.5 %) and Sept. SICs (8.8 ± 4.6 %) during the 131-130 ka interval, with cores TPC288 and TPC287 both reaching their minimum MIS 5e Sept. SIC and FCC values at this time (Figure 4.4). Following this interval of low Sept. SIC and FCC values, all three cores show an increase to their maximum Sept. SICs (58 ± 5 %) and FCC relative abundances (9 ± 5 %) at 127-126 ka (Figure 4.4). After 126 ± 2.6 ka core TPC290 displays a gradual decline in both FCC relative abundance and Sept. SIC to minimum values at 121-120 ka (Figure 4.4). In contrast, core TPC287 maintains high Sept. SICs (51 ± 3 %) throughout the 126-120 ka period as well as high (6.2 ± 1.8 %) FCC relative abundances, although they are lower than the 126 ± 2.6 ka peak of ~15 % (Figure 4.4). Core TPC288 maintains, relative to the ~130 ± 2.6 ka minimum and ~126 ± 2.6 ka maximum, intermediate FCC (2.9 ± 0.6 %) and Sept. SIC (22 ± 15 %)

values throughout the 126-120 ka interval, however the Sept. SICs are much more variable than in TPC287 (Figure 4.4).

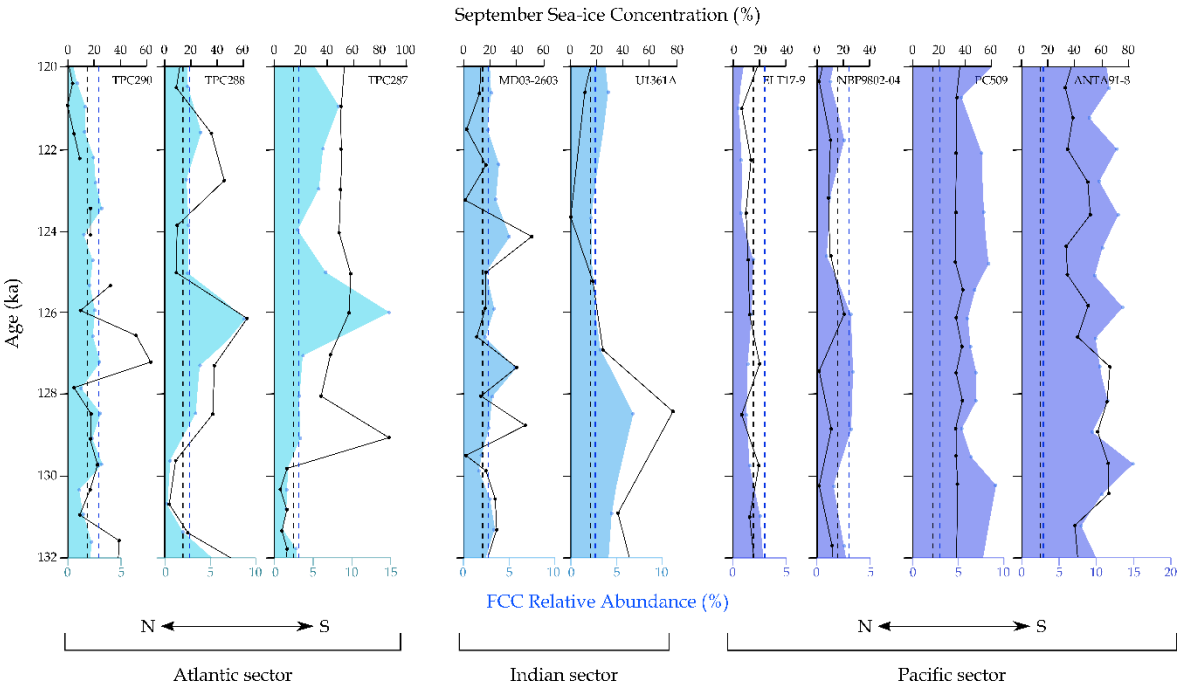

Figure 4.4 Downcore September SICs, determined using the MAT, and FCC relative abundances for the 132-120 ka interval in nine marine sediment cores. The blue shading indicates the FCC relative abundance, with the colour saturation varying between SO sectors. The solid black lines indicate the September SICs with the gaps in the TPC290 record caused by two samples being too dissimilar from all modern reference samples, so that the latter cannot be considered analogs. Dashed lines mark the mean WSIE thresholds of 3 % FCC abundance (blue lines) and 15 % sept. SIC (black lines). Within each SO sector cores are arranged from north to south.

All three Atlantic sector cores (TPC290, TPC288 and TPC287) have a strong match ($p = 0.05$, $p < 0.01$ and $p < 0.01$ respectively) between the FCC and Sept. SIC variations, with the notable exception of the TPC287 sample at ~129 ± 2.6 ka which has a very high Sept. SIC (86 %) but a relatively low FCC relative abundance (3.4 %). The only pronounced difference between the diatom species assemblage in this sample compared to neighbouring depths is a substantially higher relative abundance of *F. separanda* (Chadwick & Allen 2021f), a species known to achieve highest abundances in modern sediments overlain by WSI above 60 % (Armand et al. 2005). There was also only a single modern analog identified for this sample and so it is likely that the high *F. separanda* relative abundance (~9 %) has biased the MAT reconstruction towards colder conditions with a greater SIC than the conditions reflected by the rest of the diatom species assemblage for that sample. Thus, the reconstructed Sept. SIC for this sample is disregarded from the analysis. There are two MIS 5e samples in TPC290 (at 124.7 ± 2.6 ka and 122.8 ± 2.6 ka) for which none of the

reference surface sediment samples were below the dissimilarity threshold (see Chapter 4.2.3 for details) and thus no MAT estimate of Sept. SIC (or SSST) is given for those samples.

The two Indian sector cores (MD03-2603 and U1361A) have similar average MIS 5e FCC relative abundances (3.2 ± 1 % and 3.9 ± 1.5 %) to each other but the average Sept. SIC (19 ± 15 % and 27 ± 25 %) is nearly 10 % higher in U1361A. However, the MIS 5e variability in Sept. SIC within each core is greater than this difference between the two cores. Core MD03-2603 has three Sept. SIC maxima of >40 % during MIS 5e, at 124.1 ± 2.6 ka, 127.3 ± 2.6 ka and 128.8 ± 2.6 ka, as well as three minima of <5 % at 121.5 ± 2.6 ka, 123.3 ± 2.6 ka and 129.5 ± 2.6 ka (Figure 4.4). Contrastingly, the nearby core from Hole U1361A (Figure 4.1) has a maximum in MIS 5e Sept. SIC (76.4 %) at 128.4 ± 2.7 ka and a minimum (0 %) at 123.7 ± 2.7 ka (Figure 4.4). Together these two records suggest that the greatest MIS 5e Sept. SICs in the Indian sector occurred during the 129-127 ka interval and the minimum was at 123.5-121 ka (Figure 4.4).

Unlike the Atlantic and Indian sectors, the four cores from the Pacific sector (ELT17-9, NBP9802-04, PC509 and ANTA91-8) have low variability in their FCC relative abundances (1.4 ± 0.6 %, 2.3 ± 1 %, 5.8 ± 0.9 % and 11 ± 1.9 %) and Sept. SICs (13 ± 4 %, 8.4 ± 5.7 %, 34 ± 2 % and 48 ± 11 %) throughout MIS 5e, with no pronounced maxima or minima (Figure 4.4). The northernmost Pacific sector core, ELT17-9, has the lowest average MIS 5e FCC relative abundance (1.4 ± 0.6 %) but the more southerly core NBP9802-04 has the lowest average MIS 5e Sept. SIC (8.4 ± 5.7 %). The two most southerly Pacific sector cores (PC509 and ANTA91-8) have the highest average MIS 5e Sept. SICs and FCC relative abundances of all the cores analysed for this study.

4.4.2 Sea-surface temperatures

For the Atlantic sector cores the average MIS 5e SSSTs (3.2 ± 1.9 °C, 2.7 ± 1.6 °C and 2.2 ± 1.5 °C) show an inverse trend to Sept. SICs with higher values in more northerly cores. Both TPC288 and TPC287 have their highest MIS 5e SSSTs during the 131-129 ka interval (5 °C and 4.3 °C, respectively) followed by a SSST minimum at ~126 ± 2.6 ka (0.1 °C and 0.6 °C, respectively) (Figure 4.5). In contrast, the warmest MIS 5e SSSTs for TPC290 occur in the youngest part of the record, with an average of 6 °C in the 122-120 ka period (Figure 4.5). The relative abundance of subtropical diatoms in core TPC290 shows a good consistency ($p < 0.01$, $R^2 = 0.51$) with the SSST pattern during MIS 5e, with the highest relative abundances (1.6 ± 0.8 %) after 126 ± 2.6 ka (Figure 4.5). In the southernmost Atlantic sector core, TPC287, there is a very poor match between MIS 5e SSSTs and subtropical diatom relative abundances ($p = 0.3$, $R^2 = 0.11$). This lack of correlation is likely due to the scarcity of subtropical diatoms at this site throughout MIS 5e, as can also be seen in modern

surface sediments (Chadwick 2020), and thus a single valve can create a relative abundance peak that may be largely unrelated to the SSST trends.

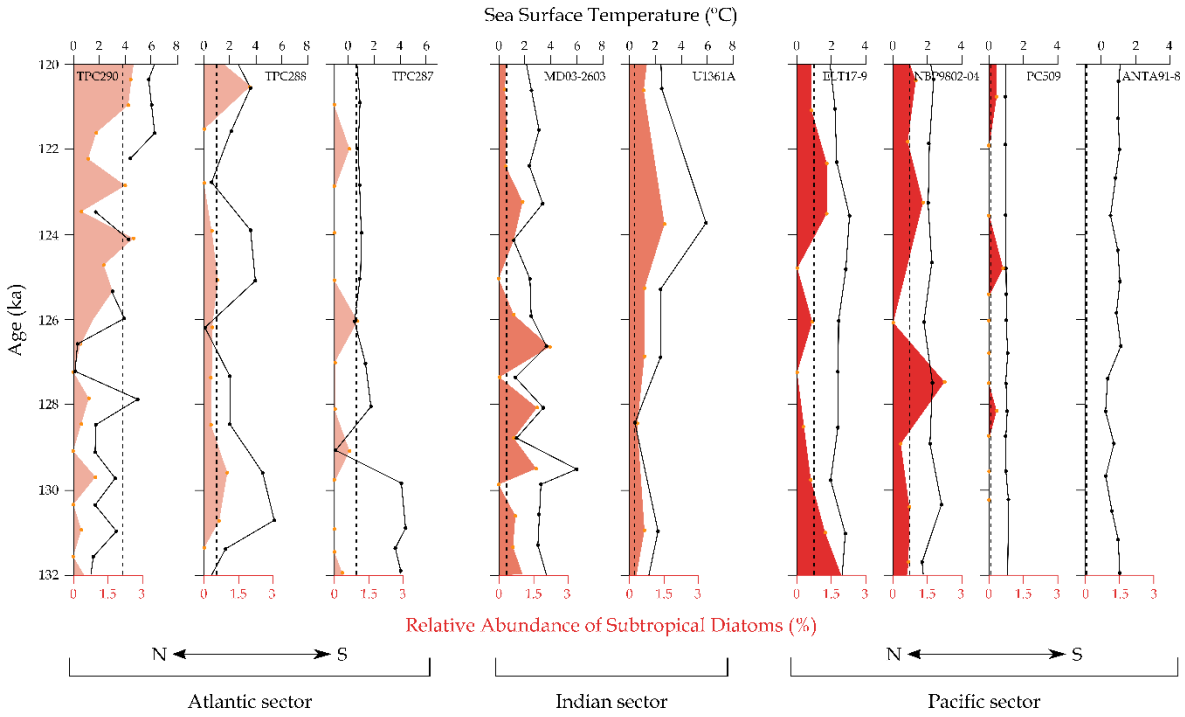

Figure 4.5 Downcore summer (January to March) SSTs, determined using the MAT, and the relative abundance of all tropical/subtropical diatom species (Romero et al. 2005) for the 132-120 ka interval in nine marine sediment cores. The red shading indicates the relative abundance of subtropical diatom species, with the colour saturation varying between SO sectors. The solid black lines indicate SSSTs, with the gaps in the TPC290 record caused by two samples being too dissimilar from all modern reference samples, so that the latter cannot be considered as analogs. Black dashed lines mark the modern SSSTs at each core site (Hersbach et al. 2019). Within each SO sector cores are arranged from north to south.

The Indian sector cores have similar average SSSTs (2.8 ± 1.1 °C and 2.4 ± 1.7 °C). However, unlike for the Sept. SICs (Figure 4.4), the MIS 5e SSST minima and maxima in cores MD03-2603 and U1361A occur at different times (Figure 4.5). SSSTs in core U1361A fall to a minimum of 0.7 °C at ~128 ± 2.7 ka before rising to a maximum of 5.9 °C at ~124 ± 2.7 ka. In contrast, SSSTs in core MD03-2603 reach an early peak of 5.9 °C at ~129.5 ± 2.6 ka and have minima of ~1 °C at 124.1 ± 2.6 ka, 127.3 ± 2.6 ka and 128.8 ± 2.6 ka (Figure 4.5). Both MD03-2603 and U1361A show a strong coherence between the MIS 5e SSSTs and the subtropical diatom abundance ($p = 0.02$, $R^2 = 0.34$ and $p < 0.01$, $R^2 = 0.98$ respectively).

In the Pacific sector cores, SSSTs are largely consistent throughout MIS 5e, with averages of 2.5 ± 0.3 %, 2.2 ± 0.3 %, 1.03 ± 0.03 % and 0.8 ± 0.3 % (Figure 4.5). Although there is very little variation in MIS 5e SSSTs in all four records, both core NBP9802-04 and core PC509 reveal maximum SSSTs (2.8 °C and 1.1 °C, respectively) at ~130 ± 2.7 ka (Figure 4.5). None of the Pacific sector cores show

a strong match between MIS 5e SSSTs and the relative abundance of subtropical diatom species. For the more southerly core PC509 this poor correlation ($p = 0.65$, $R^2 = 0.02$) is likely caused by the same scarcity of subtropical diatoms as for core TPC287 in the Atlantic sector.

4.5 Discussion

Both the Sept. SICs and FCC relative abundances indicate substantial differences in the pattern of MIS 5e WSIE change between the three SO sectors, most notably between the Atlantic and Pacific sectors. In all three Atlantic sector records, the FCC relative abundances and Sept. SICs indicate year-round open marine conditions and thus a poleward contraction of the mean WSIE (FCC <3 % (Gersonde & Zielinski 2000) and Sept. SIC <15 % (Zwally et al. 2002)) during the 131-130 ka interval. This minimum is succeeded by a re-expansion of sea ice to a maximum extent in the 127-126 ka interval when all three core sites were covered by WSI. An early minimum in MIS 5e WSIE succeeded by a maximum ~4 ka later is a consistent, but offset, pattern as the FCC relative abundance in nearby core PS2305-6 (Figures 2.8 & 4.1, Chapter 2.5.2) (Bianchi & Gersonde 2002).

I cannot rule out that the apparent retreat in Atlantic sector sea ice to a minimum during Termination II followed by a sea-ice expansion coincident with peak Antarctic air temperatures is an artefact caused by chronological uncertainties, with the WSIE minimum actually occurring alongside the peak Antarctic air temperatures at ~128 ± 1.5 ka (Parrenin et al. 2013a, Holloway et al. 2017). However, a genuine early (i.e., before 130 ka) retreat in Atlantic sector sea ice would also be consistent with most of the Termination II and MIS 5e records from this sector analysed by Bianchi & Gersonde (2002). Model experiments by Menviel et al. (2010) have demonstrated that during early MIS 5e the release of vast quantities of glacial meltwater into the surface waters of the Antarctic Zone (the region south of the Antarctic Polar Front) caused by Antarctic ice sheet deglaciation, especially the potential partial or total loss of the West Antarctic Ice Sheet (WAIS), would have led to SST reduction and equatorward sea-ice expansion. Importantly, this meltwater injection into the SO, which is supported by the observation of meltwater "spikes" characterizing planktic foraminifera $\delta^{18}O$ data in cores from the Weddell Sea continental margin during glacial-interglacial transitions (Grobe et al. 1990), would also have resulted in a warming of subsurface waters that, in turn, would have triggered further ocean-forced melting of the ice-sheet grounding zones, especially of the predominantly marine-based WAIS, thus kick starting a positive feedback loop (Menviel et al. 2010, Bronselaer et al. 2018). Because of their location within "Iceberg Alley", a main pathway of Antarctic icebergs travelling with the clockwise Weddell Gyre from the southern Weddell Sea Embayment into the Scotia Sea (Weber et al. 2014), core TPC290 and especially cores TPC287 and TPC288 can be expected to be particularly sensitive for recording such meltwater supply.

In fact, the MIS 5e WSIE maximum in the Atlantic sector records coincides, within chronological uncertainty, with higher global sea level (Kopp et al. 2013) and evidence for increased meltwater flux in the Weddell Sea (Chapter 3.4.3), which both indicate substantial mass loss from the Antarctic ice sheets, consistent with findings of major ice loss in the Weddell Sea sector during MIS 5e (Turney et al. 2020a). Higher glacial meltwater fluxes associated with increased ice-sheet loss could therefore be a major driver of the WSIE expansion in the Atlantic sector records as fresh surface waters are stratified from the underlying waters and are therefore able to cool more rapidly and freeze (Bintanja et al. 2013, Merino et al. 2018). The peak in FCC abundance in core TPC287 at 126 ± 2.6 ka is primarily a peak in the abundance of *F. cylindrus* (Chadwick & Allen 2021f). *F. cylindrus* generally dominates water column diatom assemblages in both ice-covered (Burckle et al. 1987) and marginal sea-ice zones (Kang & Fryxell 1992, 1993, Kang et al. 1993). The occurrence of high modern *F. cylindrus* abundances in marginal sea-ice zones indicates that this species is not purely associated with sea-ice, from which it might have been seeded when retreating, but also strongly affiliated with sea-ice melt and strong surface stratification (Kang & Fryxell 1993, Cremer et al. 2003, von Quillfeldt 2004). The peak in *F. cylindrus* abundances at 126 ± 2.6 ka in core TPC287, separate from any notable increase in *F. curta* abundance, therefore supports an increased glacial meltwater signal at this time.

The discrepancy between Sept. SICs and FCC relative abundances at ~127 ± 2.6 ka in core TPC290 (Figure 4.4) is likely due to increased *Chaetoceros* rs. abundance at this time (Chadwick & Allen 2021h). This *Chaetoceros* rs. abundance increase is also observed in the nearby core PS2305-6 (Bianchi & Gersonde 2002) and is inferred to be caused by higher meltwater and iceberg flux at this time (Crosta et al. 1997, Bianchi & Gersonde 2002). For core TPC290, there is a scarcity of modern analogs from the Scotia Sea region (Gersonde et al. 2005) and thus, the high *Chaetoceros* rs. abundances in MIS 5e samples are associated with modern analogs from sites along the Antarctic Peninsula, where SICs are greater than in the Scotia Sea.

Atlantic sector SSSTs reach their maxima during Termination II before a substantial drop coincident with the peak Antarctic air temperatures in ice cores (Parrenin et al. 2013a). As with the down-core Sept. SIC profiles, this offset may result from chronological uncertainties, with the highest SSSTs actually occurring alongside peak Antarctic air temperatures at ~128 ± 1.5 ka. However, air temperature and SST reconstructions from the Antarctic Peninsula and Scotia Sea have shown that during Termination I temperatures peaked at higher values than during the Holocene (Mulvaney et al. 2012, Xiao et al. 2016), thus, my records could indicate an equivalent early warming during Termination II for this region. Also, if the high air temperatures at ~128 ± 1.5 ka caused substantial Antarctic ice sheet loss, then the cold SSSTs in my ice-sheet proximal records at this time could, as

discussed above, actually reflect major input of cold and fresh meltwater not recorded in cores further north.

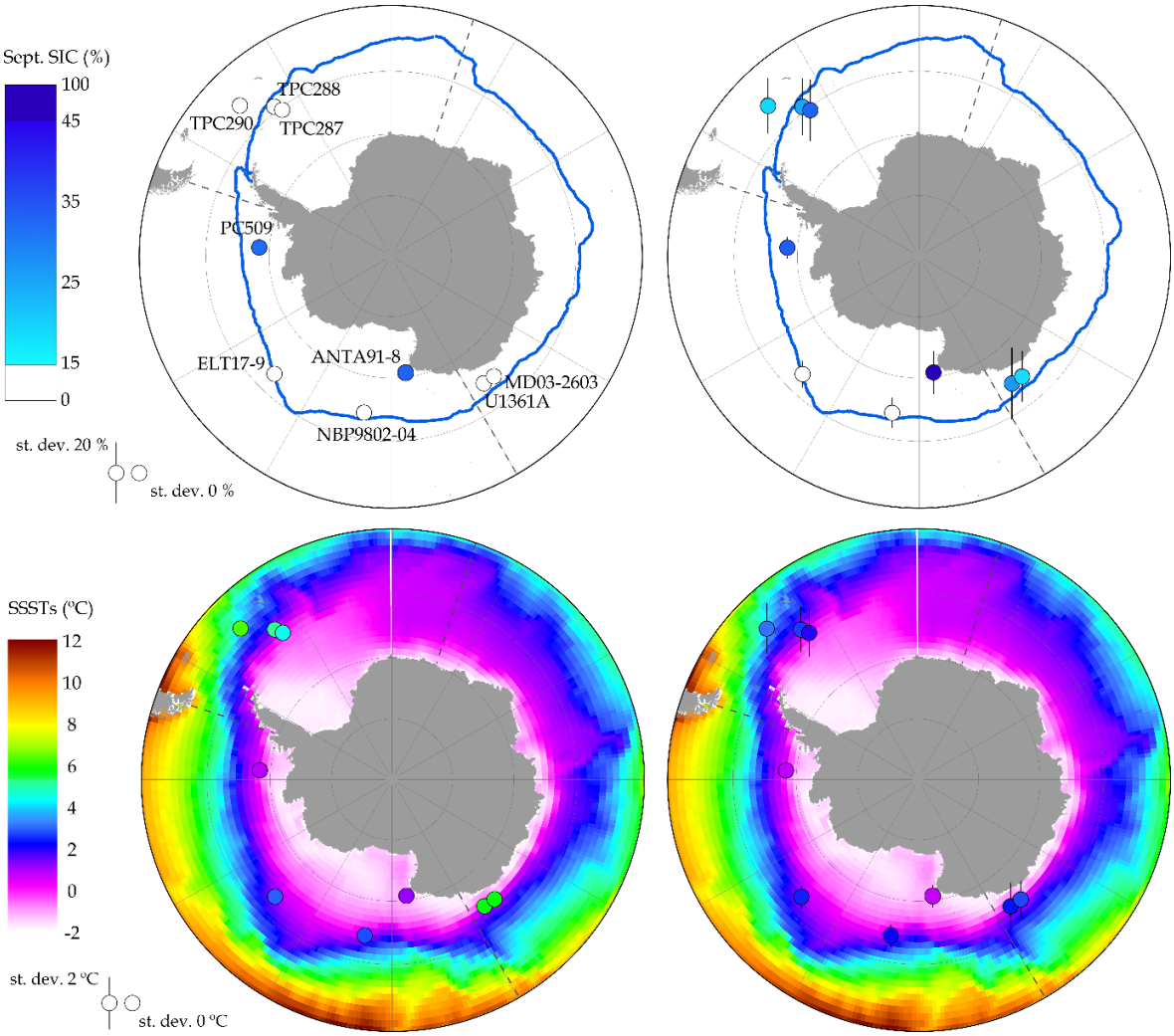

Figure 4.6 Maps of MIS 5e SSSTs and Sept. SICs for the nine core sites compared with the modern conditions. On all maps the SO sector boundaries are marked with dashed lines. **Top left:** Minimum MIS 5e Sept. SIC for each core site (coloured circles) compared to the modern (1981-2010) 15 % September sea-ice extent (blue line) (Fetterer et al. 2017). **Top right:** Average MIS 5e Sept. SIC (coloured circles) and standard deviations (vertical bars) for each core site compared to the modern (1981-2020) 15 % September sea-ice extent (blue line) (Fetterer et al. 2017). **Bottom left:** Maximum MIS 5e SSST for each core site (coloured circles) compared to modern (Jan-Mar, 1980-2019) SSSTs (Hersbach et al. 2019). **Bottom right:** Average MIS 5e SSST (coloured circles) and standard deviation (vertical bars) for each core site compared to modern (Jan-Mar, 1980-2019) SSSTs (Hersbach et al. 2019). Core data is given in Table 4.4.

In the Indian sector, core MD03-2603 has an average MIS 5e Sept. SIC (25 ± 18 %) and FCC relative abundance (3.2 ± 1 %) indicative of a location just south of the mean WSIE (Figures 4.4 & 4.6) but with multiple maxima and minima contributing to the high variability. MIS 5e Sept. SICs and FCC relative abundances in the nearby core U1361A indicate that it was located within the seasonal sea-ice zone from 132-126 ka before the mean WSIE retreated to the south of this location (Figures 4.4

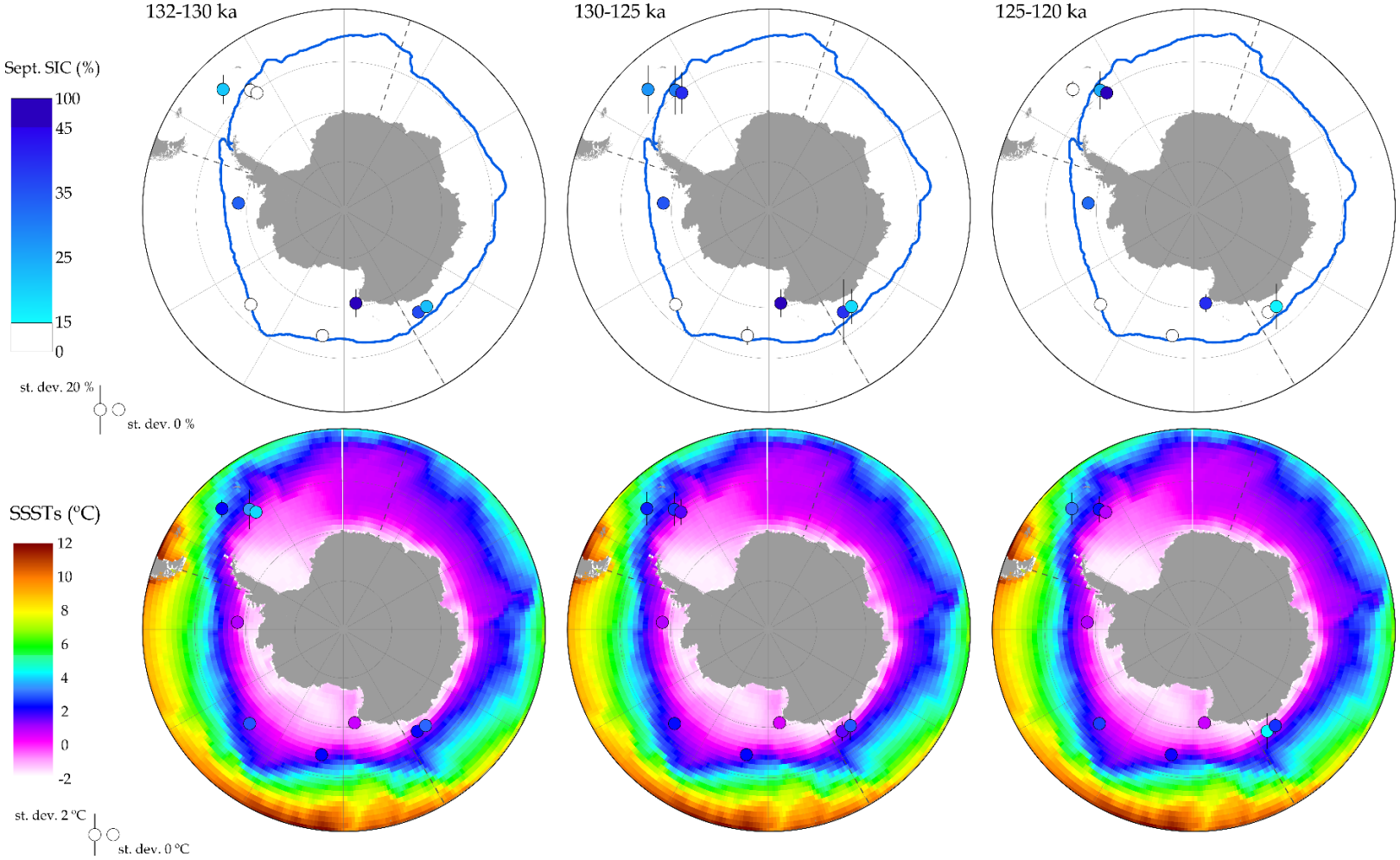

Figure 4.7 Expansion of the maps in the RHS of Figure 4.6 with average values (coloured circles) and standard deviations (vertical bars) for Sept. SICs (upper row) and SSSTs (lower row) given for three time slices: 132-130 ka, 130-125 ka and 125-120 ka (see Chapter 3.4.2 for details on choice of time intervals).

Core	Minimum Sept. SIC (%)	Age of Sept. SIC min (ka)	Maximum SSST (°C)	Age of SSST max (ka)	Mean Sept. SIC ± st. dev. (%)	Mean SSST ± st. dev. (°C)	Modern Sept. SIC (%)	Modern SSST (°C)
TPC290	0.0	120.97 ± 2.58	6.2	121.60 ± 2.58	19.4 ± 17.2	3.2 ± 1.9	0	3.9
TPC288	3.9	130.70 ± 2.59	5.4	130.70 ± 2.59	24.8 ± 18.2	2.7 ± 1.6	71	1.1
TPC287	5.2	130.36 ± 2.57	4.5	130.86 ± 2.57	33.0 ± 20.4	2.2 ± 1.5	87	0.6
MD03-2603	0.0	129.50 ± 2.56	5.9	129.50 ± 2.56	18.9 ± 15.2	2.8 ± 1.1	88	0.6
U1361A	0.0	123.71 ± 2.70	5.9	123.71 ± 2.70	27.2 ± 24.6	2.6 ± 1.6	92	0.4
ELT17-9	6.9	128.52 ± 2.51	3.0	123.52 ± 2.51	12.6 ± 4.4	2.5 ± 0.3	14	1.1
NBP9802-04	1.4	130.29 ± 2.68	2.8	130.29 ± 2.68	8.4 ± 5.7	2.2 ± 0.3	66	1.1
PC509	32.7	129.52 ± 2.59	1.1	130.20 ± 2.59	34.1 ± 1.9	1.0 ± 0.0	90	0.1
ANTA91-8	34.0	124.31 ± 2.60	1.1	126.61 ± 2.60	47.8 ± 11.8	0.8 ± 0.3	96	-0.9

Table 4.4 MIS 5e minimum and mean Sept. SICs and maximum and mean SSSTs for the nine analysed marine sediment cores. The ages for the minimum Sept. SIC and maximum SSST are also given. Modern (1981-2010) Sept. SICs are from Fetterer et al. (2017) and modern (1980-2019) SSSTs are from Hersbach et al. (2019).

& 4.7). The different patterns in MIS 5e Sept. SIC and SSSTs between cores MD03-2603 and U1361A are likely due to the different age resolution of the samples, with two of the Sept. SIC maxima in MD03-2603 occurring in the 129-127 ka interval coincident with the U1361A Sept. SIC maximum, and likewise, two of the Sept. SIC minima in MD03-2603 occurring in the 124-121 ka period concurrent with the minimum Sept. SIC in core U1361A (Figure 4.4). The different age resolution of samples in MD03-2603 and U1361A is primarily due to the lower sedimentation rate (Table 4.2) at site U1361A, and thus a sample from this core spans more time than in core MD03-2603.

None of the Pacific sector cores show pronounced minima or maxima in their MIS 5e FCC and Sept. SIC records (Figure 4.4), indicating a less variable WSIE in this sector compared to the Atlantic and Indian sectors (Figure 4.4). The Pacific sector cores PC509 and ANTA91-8 are also the only cores in this study which are covered by WSI for the entirety of MIS 5e (Figures 4.4 & 4.6). The position of these cores south of the mean WSIE throughout MIS 5e is significant as they are the first published marine records from within the seasonal sea ice zone and able to constrain the poleward limit of the MIS 5e minimum WSIE (Chapter 2). Cores ELT17-9 and NBP9802-04 are the only records in this study with average MIS 5e Sept. SICs <15 % (Figure 4.6), indicating they were located north of the mean WSIE for the majority of the 132-120 ka period, with core ELT17-9 having been located closer to the MIS 5e mean WSIE. The FCC relative abundances for cores ELT17-9 and NBP9802-04 also indicate that both were located on average north of the mean WSIE during MIS 5e (Figure 4.4) but suggest that core NBP9802-04 was located closer to the MIS 5e mean WSIE.

The reconstructed MIS 5e Sept. SICs for site ELT17-9 are higher than for site NBP9802-04 (Figure 4.4) which is likely related to the higher abundance of *Chaetoceros* rs. in core ELT17-9 when compared to core NBP9802-04 (Chadwick & Allen 2021b, d). The *Chaetoceros* rs. group is associated with both WSI (Armand et al. 2005) and meltwater stratification (Crosta et al. 1997), and high abundances of *Chaetoceros* rs. in Ross Sea sediments deposited during past interglacial periods have been linked to increased upwelling and subsequent meltwater stratification within the Ross Sea Gyre (Kim et al. 2020). The high *Chaetoceros* rs. abundance in core ELT17-9 during MIS 5e could therefore indicate an north-eastward shift of the Ross Sea gyre from its modern day position (Dotto et al. 2018) and an accompanying displacement of meltwater circulation (Merino et al. 2016) and the WSI edge in the Pacific sector. It is also possible that the reduced Pacific sector WSIE during MIS 5e is associated with earlier seasonal sea-ice retreat during the austral spring and a longer open-ocean season, promoting a stronger spring bloom signal, of which the *Chaetoceros* group is a major component (Leventer 1991).

The average MIS 5e SSSTs in the nine cores are ~1-2 ^{o}C warmer than the modern SSSTs (Figure 4.6), consistent with the SST anomalies presented in Chadwick et al. (2020) and Capron et al. (2014).

However, the SSST records in the Atlantic and Indian sectors have large variability with maximum SSSTs that are 2-4 °C higher than the MIS 5e average SSSTs (Figure 4.6). Maximum MIS 5e SSSTs in the Atlantic and Indian sectors were therefore ~3-5 °C warmer than modern SSSTs (Figure 4.6), which is a much larger SSST anomaly than in the Antarctic Zone (south of the Antarctic Polar Front) records presented in Figure 2.7, and marks a ~5° poleward shift in SSST isotherms relative to the present. Unlike the Atlantic and Indian sectors, the Pacific sector core records indicate low variability in MIS 5e SSSTs with peak values 0-2 °C warmer than present (Figure 4.6) marking a poleward shift in SSST isotherms of <3°.

Within their chronological uncertainties (Table 4.2), cores TPC288, TPC287, MD03-2603, ELT17-9, NBP9802-04 and PC509 all reach minimum MIS 5e Sept. SICs synchronously (Table 4.4) and coincident with the peak in Antarctic air temperatures and minimum in EPICA Dome C (EDC) sea-salt sodium flux (Na_{ss}) at ~128 ± 1.5 ka (Wolff et al. 2006, Holloway et al. 2017). The two Indian sector core records reach a minimum MIS 5e WSIE (and maximum SSST in core U1361A) ~4.5 ka after the Na_{ss} minimum in Antarctic ice cores, outside of the combined chronological uncertainties of the sediment cores (Table 4.2) and AICC2012 ice core chronology (Bazin et al. 2013b). Although the duration of the SSST maximum, and accompanying WSIE minimum, in core MD03-2603 is short, it occurs within chronological error of the maximum air temperatures in Antarctic ice cores (Figures 4.4 & 4.5).

Satellite era trends in Antarctic winter SIC (Hobbs et al. 2016) are largely consistent with the patterns observed during MIS 5e. Northern Weddell Sea winter SIC has declined by 5-10 % per decade in the satellite era (Hobbs et al. 2016) indicating a sensitivity to warming consistent with the early retreat of MIS 5e sea ice in this region. Similarly, winter SICs in the Pacific sector have remained stable, or even slightly increased, during the satellite era (Hobbs et al. 2016) which is in agreement with the stability of the Pacific sector WSIE throughout MIS 5e. In recent decades, Bellingshausen Sea summer sea ice has decreased, whilst WSIE has stayed stable (Hobbs et al. 2016, Parkinson 2019). The MIS 5e Sept. SICs and SSSTs (as a proxy for summer sea ice) imply that the MIS 5e WSIE in the Bellingshausen Sea is similar to the modern but the summer sea-ice extent was reduced. The western Ross Sea is a region in which the modern and MIS 5e trends differ, with recent winter SIC increases of 10-15 % per decade contrasting with the MIS 5e WSIE reduction observed at site NBP9802-04.

4.6 Conclusions and wider implications

During MIS 5e the three SO sectors display heterogeneous responses in WSIE and SSSTs, which may guide predictions of the impact of future warming on the Antarctic region. The prominent early

(131-130 ka) minimum in WSIE and coinciding maximum in SSSTs for the two southerly Atlantic sector cores (TPC288 and TPC287, Figure 4.4) is associated with a mean WSI edge located at least 3-5° south of its modern position. This substantial reduction in WSIE and seasonal sea-ice cover would have reduced brine rejection and likely decreased the rates of deep and bottom water formation in the Weddell Sea, causing a warming of the abyssal waters (Bouttes et al. 2010, Marzocchi & Jansen 2019). Deep water warming would have promoted the basal melting and retreat of Weddell Sea ice shelves and marine terminating ice streams, causing substantial Antarctic ice sheet mass loss (Hellmer et al. 2012, Rignot et al. 2019, Wahlin et al. 2021). I hypothesise that substantial mass loss from the Weddell Sea sector of the WAIS (Turney et al. 2020a) drove the Atlantic sector WSI resurgence at ~126 ± 2.6 ka, as suggested by the model experiments of Menviel et al. (2010), and contributed to the global sea-level rise at this time (Kopp et al. 2013, Sime et al. 2019).

Variations in the WSIE and SSST records between the Indian sector cores MD03-2603 and U1361A are due to the differences in sampling resolution, with the MD03-2603 record indicating multiple relatively short duration WSIE and SSST oscillations during MIS 5e. The U1361A record seems to present an averaged signal of these oscillations with a greater frequency of warm periods with reduced WSIE after 125 ± 2.7 ka. Along the modern Wilkes Land margin the Antarctic Circumpolar Current (ACC) flows much closer to the continent than in other regions (Tamsitt et al. 2017) and the MIS 5e record in core MD03-2603 could therefore suggest multiple intervals when the ACC was displaced to the south of its modern position. A southerly shift of the ACC would increase the advection of warmer Circumpolar Deep Water onto the Antarctic continental shelf (Fogwill et al. 2014), promoting periods of high basal melting and ice sheet retreat in Wilkes Land during MIS 5e, as supported by Wilson et al. (2018).

In contrast to the Atlantic and Indian sectors, the Pacific sector records indicate a more stable WSIE throughout MIS 5e. The MIS 5e Sept. SIC records of cores ELT17-9 and NBP9802-04 indicate a poleward shift in the mean WSI edge by at least 2° of latitude relative to the modern. The PC509 record indicates a southerly shift in the mean WSI edge by <2° latitude. This highlights a seemingly greater resilience of sea ice in the Bellingshausen Sea with the WSI edge having remained north of 68 °S throughout MIS 5e. In the modern Pacific sector the WSIE is strongly constrained by the southern extent of the ACC and the configuration of the Ross Gyre (Benz et al. 2016, Nghiem et al. 2016). An uneven poleward constriction of the ACC across the Pacific sector during MIS 5e could therefore help explain the differing WSI retreat in this region, with greater poleward migration of the ACC and reduction in the extent of the Ross Gyre in the western Pacific sector than in the eastern Pacific sector. However, unlike in the Indian sector, there is no evidence for millennial-scale migration of the ACC across the Pacific sector. The stable and persistent WSIE in the Pacific sector

during MIS 5e may have protected ice shelves in the Ross, Amundsen and Bellingshausen seas which buttressed ice grounded further upstream (Massom et al. 2018). This buttressing may have acted as a stabilising factor preventing total loss of the WAIS during MIS 5e, with the majority of its deep subglacial basins terminating in the Ross, Amundsen and Bellingshausen Seas (Gardner et al. 2018).

Similarly to the modern SO (Parkinson 2019), WSIE trends during MIS 5e show both spatial and temporal heterogeneity. The greater MIS 5e WSIE reduction in the Atlantic sector compared to the Pacific sector is consistent with recent model simulations (Holloway et al. 2017). Most of the core records in this study reach their minimum WSIE synchronously, within chronological uncertainties, with the 128 ± 1.5 ka minimum in Antarctic ice core Na_{ss} flux (Wolff et al. 2006), with only cores TPC290 and U1361A indicating a later WSIE minimum (Figure 4.4 & 4.7). The stability of the Pacific sector WSIE is likely due to the bathymetric pinning of the ACC limiting the possible poleward displacement of the ACC during MIS 5e. The apparent high sensitivity of Weddell Sea WSIE, and seeming resilience of Bellingshausen Sea WSIE, to warmer than present climates is unexpected from the recent observational trends (Hobbs et al. 2016, Parkinson 2019) and highlights the importance of reconstructing palaeoenvironmental conditions around Antarctica during past warm periods, such as MIS 5e, for understanding how the Antarctic and SO regions respond to warmer climates on longer than decadal timescales.

Chapter 5 Model-data Comparison of Antarctic Winter Sea-ice Extent and Southern Ocean Sea-surface Temperatures during MIS 5e

5.1 Introduction

The bulk of this chapter is presented in: Chadwick M., Sime L.C., Allen C.S., Guarino M.-V. & Oliver K.I.C. 2022. Model-data comparison of Antarctic winter sea-ice extent and Southern Ocean sea-surface temperatures during Marine Isotope Stage 5e. *Earth & Planetary Science Letters*, **in review**.

Model simulations of the Peak MIS 5e climate at 127 ka are a part of the Coupled Model Intercomparison Project (CMIP6) and Paleoclimate Modelling Intercomparison Project (PMIP4) (Otto-Bliesner et al. 2017). Analysis of the short (50-100 years) orbitally forced CMIP6-PMIP4 ensembles indicate that these simulations exhibit Southern Ocean (SO) summer $SSTs_{model}$ (SSSTs) which were ~0.5 ^{o}C cooler during Peak MIS 5e than the preindustrial (PI) and that there was <10 % reduction in winter sea-ice extent (WSIE) at 127 ka relative to the PI (Otto-Bliesner et al. 2021). These simulation results are a poor match for published Peak MIS 5e proxy records from SO marine sediment cores, which indicate a $SSST_{proxy}$ warming of 0-5 ^{o}C relative to the PI (Capron et al. 2017, Otto-Bliesner et al. 2021). The SO model-data discrepancy is hypothesised to be due to the absence of the Heinrich 11 (H11) meltwater event in CMIP6-PMIP4 Tier 1 simulations (Otto-Bliesner et al. 2021). However, it should also be noted that model-data comparisons of MIS 5e Antarctic WSIE have been limited by the location of most published marine sediment core records, which are located north of the modern WSIE, and likely also north of the 127 ka WSIE (Holloway et al. 2017, Chadwick et al. 2020).

Published syntheses of proxy records from SO marine sediment cores indicate Peak MIS 5e $SSSTs_{proxy}$ were between 0 and 5 ^{o}C warmer than the present and PI, with this warming anomaly decreasing towards the South Pole (Capron et al. 2017, Chadwick et al. 2020). The most southerly cores in Capron et al. (2017) and Chadwick et al. (2020) have $SSST_{proxy}$ anomalies for Peak MIS 5e of <1.5 ^{o}C (40 ^{o}W – 40 ^{o}E), but there are no MIS 5e marine records located south of the modern Antarctic Polar Front for most of the SO (80 ^{o}E – 40 ^{o}W). Whilst most proxy records of Antarctic sea ice are located too far north to precisely constrain the Peak MIS 5e $WSIE_{proxy}$, the results in Chapter 4 suggests that the winter sea-ice (WSI) edge was located 1-2^{o} south of its modern position in the Pacific sector and >5^{o} south of its modern position in the Atlantic sector.

This chapter presents Peak MIS 5e Antarctic September sea-ice concentrations (SIC_{model}) and SO $SSSTs_{model}$ from the latest UK fully-coupled HadGEM3-GC3.1 (hereafter HadGEM3) numerical simulations, both with and without the H11 meltwater event (Guarino et al. 2022, *in review*), and from the H11 meltwater-hosed HadCM3 numerical simulations in Holloway et al. (2018). These model outputs are compared with diatom transfer function estimates of September SIC_{proxy} and $SSSTs_{proxy}$ from nine marine sediment cores (Chapter 4) to answer the following:

- How much warmer were SO $SSSTs_{proxy}$ during Peak MIS 5e compared to PI observations? And does this match previous proxy record syntheses from Capron et al. (2017) and Chadwick et al. (2020)?
- Is H11 meltwater forcing necessary to explain these new proxy data?
- Can we tell if state of the art models are capable of accurately simulating the conditions depicted by these new proxy data?

5.2 Materials and methods

5.2.1 Numerical simulations

HadGEM3 is a global coupled atmosphere-land-ocean-ice model which combines the Unified Model atmosphere model (Walters et al. 2017), the JULES land surface model (Walters et al. 2017), the NEMO ocean model (Madec et al. 2019) and the CICE sea-ice model (Ridley et al. 2018). The atmosphere and land components of the HadGEM3 simulations utilise a horizontal grid spacing of ~135 km on a regular latitude-longitude grid with 85 vertical (pressure) levels and the ocean and sea-ice components employ an orthogonal curvilinear grid with a 1^{o} resolution (reduced to 0.33^{o} near the equator) and 75 vertical levels. The HadGEM3 model simulations analysed here are part of the CMIP6-PMIP4 model intercomparison project. The PI control run is presented in Menary et al. (2018) and uses a constant 1850 climate forcing (see Menary et al. (2018) for further details).

The standard Peak MIS 5e run (hereafter referred to as LIG_HG) is presented in Guarino et al. (2020) and the H11 run is presented in Guarino et al. (2022, *in review*). They were run using the protocol described in Otto-Bliesner et al. (2017) for Tier 1 and Tier 2 PMIP4 simulations. The Peak MIS 5e climate was simulated by forcing the HadGEM3 model with constant last interglacial orbital and greenhouse gas boundary conditions (see Guarino et al. (2022, *in review*) for further details). In the H11 run the H11 meltwater event is simulated by adding a constant freshwater flux, equal to 0.2 Sv, evenly across the North Atlantic between 50 and 70 ^{o}N. The H11 simulation was run for 250 years with the climatological averages from the final 100 years (150-250 years) presented here (hereafter referred to as H11(250)_HG).

The HadCM3 simulations are presented in Holloway et al. (2018), with 0.25 Sv freshwater forcing to the North Atlantic applied for 1600 years. The climatological averages for years 150-250 of the model run (hereafter referred to as H11(250)_HC) are used, to match the length of the run performed for HadGEM3, and the last 100 years (1500-1600 years)(hereafter referred to as H11(1600)_HC), to examine how $SSSTs_{model}$ and $SICs_{model}$ have evolved after a longer period of H11 type forcing. The atmosphere model component within HadCM3 has a horizontal resolution of 3.75° longitude by 2.5° latitude and 19 vertical levels and the ocean model component has a horizontal resolution of 1.25° and 20 vertical levels (Gordon et al. 2000).

Peak MIS 5e $SSSTs_{model}$ (average January to March) are presented as anomalies relative to the PI control runs whereas September $SICs_{model}$ are presented as absolute values for Peak MIS 5e. All HadGEM3 and HadCM3 model output presented in this chapter are available from the JASMIN group workspace (https://gws-access.jasmin.ac.uk/public/pmip4/EPSL_Chadwicketal_2022/).

5.2.2 Marine sediment cores

Modern Analog Technique diatom transfer function estimates of Peak MIS 5e September $SICs_{proxy}$ and $SSSTs_{proxy}$ from nine marine sediment cores (detailed in Table 4.1) are compared to model output. The transfer function methodology is detailed in Chapter 4.2.3 and the data for all the cores is available from Chadwick et al. (2021). Reconstructed September $SICs_{proxy}$ have a RMSEP of 0.09 and $SSSTs_{proxy}$ have a RMSEP of 1.1 °C. For PI $SSSTs_{proxy}$ at each core site the average January-March SST_{proxy} from 1870-1900 was calculated from the HadISST1 dataset (Rayner et al. 2003). The average $SSST_{proxy}$ and September SIC_{proxy} in the 130-128 ka interval is considered to represent Peak MIS 5e conditions. This time interval is chosen as it is within the chronological uncertainty (±2 ka) of both the peak $\delta^{18}O$ in the EPICA Dome C ice core record at ~128 ka (Sime et al. 2009) and the termination of the H11 meltwater event at 130 ka (Marino et al. 2015).

5.3 Results

5.3.1 $SSST_{model}$ anomalies

In both the LIG_HG and H11(250)_HG simulations the pattern of $SSST_{model}$ anomalies for Peak MIS 5e relative to the PI is very similar (Figure 5.1a & b). Both runs show a cooling (0-1 °C) in the Atlantic sector (70 °W – 20 °E) and a warming (0-1.5 °C) in the Indian sector (20 – 150 °E) during Peak MIS 5e relative to the PI, with both trends more pronounced in the H11(250)_HG run (Figure 5.1b). In the Pacific sector (150 °E – 70 °W), both the LIG_HG and H11(250)_HG simulations show a warming (0-1 °C) in the eastern region (120 – 70 °W) and a cooling (0-0.5 °C) in the western region, south of

the modern WSIE (150 °E – 150 °W) but have diverging trends in the central area (150 – 120 °W) where the LIG_HG run has a warming of up to 1 °C and the H11(250)_HG run has a mixture of warming and cooling, all by less than 0.5 °C (Figure 5.1a & b).

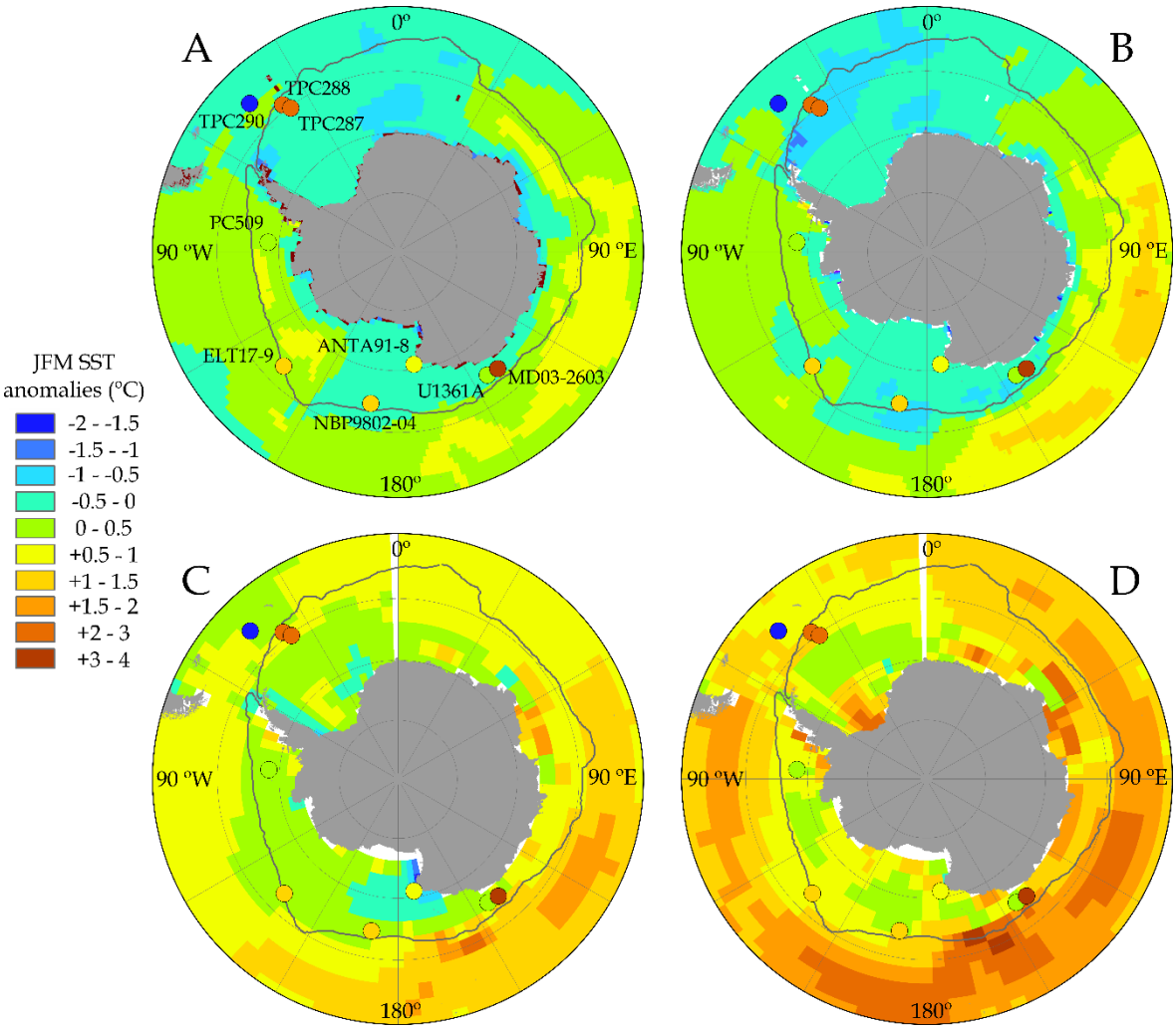

Figure 5.1 Maps of summer (JFM) SST_{model} anomalies for Peak MIS 5e relative to the PI. **A** - LIG_HG. **B** - H11(250)_HG. **C** - H11(250)_HC (Holloway et al. 2018). **D** - H11(1600)_HC (Holloway et al. 2018). Coloured circles on all maps represent the JFM SST_{proxy} anomalies in nine marine sediment cores (Table 2). The grey line on all maps marks the modern (1981-2010) median September sea-ice extent (Fetterer et al. 2017).

The H11(250)_HC and H11(1600)_HC simulations both have greater warming trends than either of the LIG_HG or H11(250)_HG runs, with only a few localised areas of cooling in the H11(250)_HC run and none in H11(1600)_HC run (Figure 5.1c & d). In the H11(250)_HC run the area north of the modern WSIE had largely warmed by 0.5-1.5 °C, whereas the region within the modern WSIE was mostly less than 0.5 °C warmer than PI (Figure 5.1c). In the H11(1600)_HC run the $SSST_{model}$ anomalies have increased throughout the SO relative to the H11(250)_HC run, with the region within the modern WSIE mainly 0.5-1.5 °C warmer than PI and the area to the north of the modern

WSIE largely showing 1-3 °C warming (Figure 5.1d). Similarly to the LIG_HG and H11(250)_HG simulations, both the H11(250)_HC and H11(1600)_HC simulations have the greatest Peak MIS 5e warming in the 90-170 °E region, north of 60 °S (Figure 5.1c & d).

	TPC290	TPC288	TPC287	ELT17-9	NBP9802-04	MD03-2603	U1361A	PC509	ANTA91-8
$SSST_{proxy}$ anomaly (°C)	-1.70	+2.65	+2.75	+1.24	+1.43	+3.13	+0.04	+0.24	+1.00
LIG_HG $SSST_{model}$ anomaly (°C)	-0.03	-0.19	-0.31	+0.19	-0.32	-0.19	-0.20	+0.24	-0.10
H11(250)_HG $SSST_{model}$ anomaly (°C)	-0.16	-0.50	-0.78	-0.03	-0.55	-0.50	-0.66	-0.03	-0.13
H11(250)_HC $SSST_{model}$ anomaly (°C)	+0.45	+0.65	+0.65	+0.35	+0.05	+0.55	+0.45	+0.15	-0.15
H11(1600)_HC $SSST_{model}$ anomaly (°C)	+0.95	+0.75	+0.75	+0.85	+0.35	+0.95	+0.25	+0.55	+0.45
September SIC_{proxy}	0.19	0.23	0.22	0.13	0.11	0.19	0.63	0.34	0.62
LIG_HG September SIC_{model}	0.00	0.71	0.89	0.00	0.67	0.93	0.93	0.73	0.96
H11(250)_HG September SIC_{model}	0.00	0.79	0.94	0.01	0.80	0.94	0.94	0.85	0.95
H11(250)_HC September SIC_{model}	0.00	0.42	0.42	0.66	0.96	0.94	0.95	0.47	0.97
H11(1600)_HC September SIC_{model}	0.00	0.22	0.22	0.17	0.94	0.93	0.94	0.19	0.97

Table 5.1 Diatom transfer function values and model output for Peak MIS 5e September $SICs_{model/proxy}$ and $SSST_{model/proxy}$ anomalies (Peak MIS 5e – PI) for nine marine sediment core locations. Model output is given for LIG_HG and H11(250)_HG (Guarino et al. 2022, *in review*) and for H11(250)_HC and H11(1600)_HC (Holloway et al. 2018). Diatom transfer function values for Peak MIS 5e are an average of the 130-128 ka interval and are presented in Chapter 4.

5.3.2 $SSST_{proxy}$ anomalies

With the exception of core TPC290, the sediment cores all indicate warmer conditions during Peak MIS 5e than the PI (Table 5.1 & Figure 5.1). The four Pacific sector cores (ELT17-9, NBP9802-04, PC509 and ANTA91-8) have $SSST_{proxy}$ anomalies of less than 1.5 °C, with the more southerly two (PC509 and ANTA91-8) showing a warming of less than 1 °C (Table 5.1). The nearby cores TPC288 and TPC287 in the Atlantic sector have similar $SSST_{proxy}$ anomalies to each other, whereas, in the Indian sector, the proximally located cores MD03-2603 and U1361A have very different $SSST_{proxy}$

anomalies to each other, with the $SSST_{proxy}$ anomaly for core MD03-2603 more than 3 °C warmer than the anomaly in core U1361A (Table 5.1 & Figure 5.1).

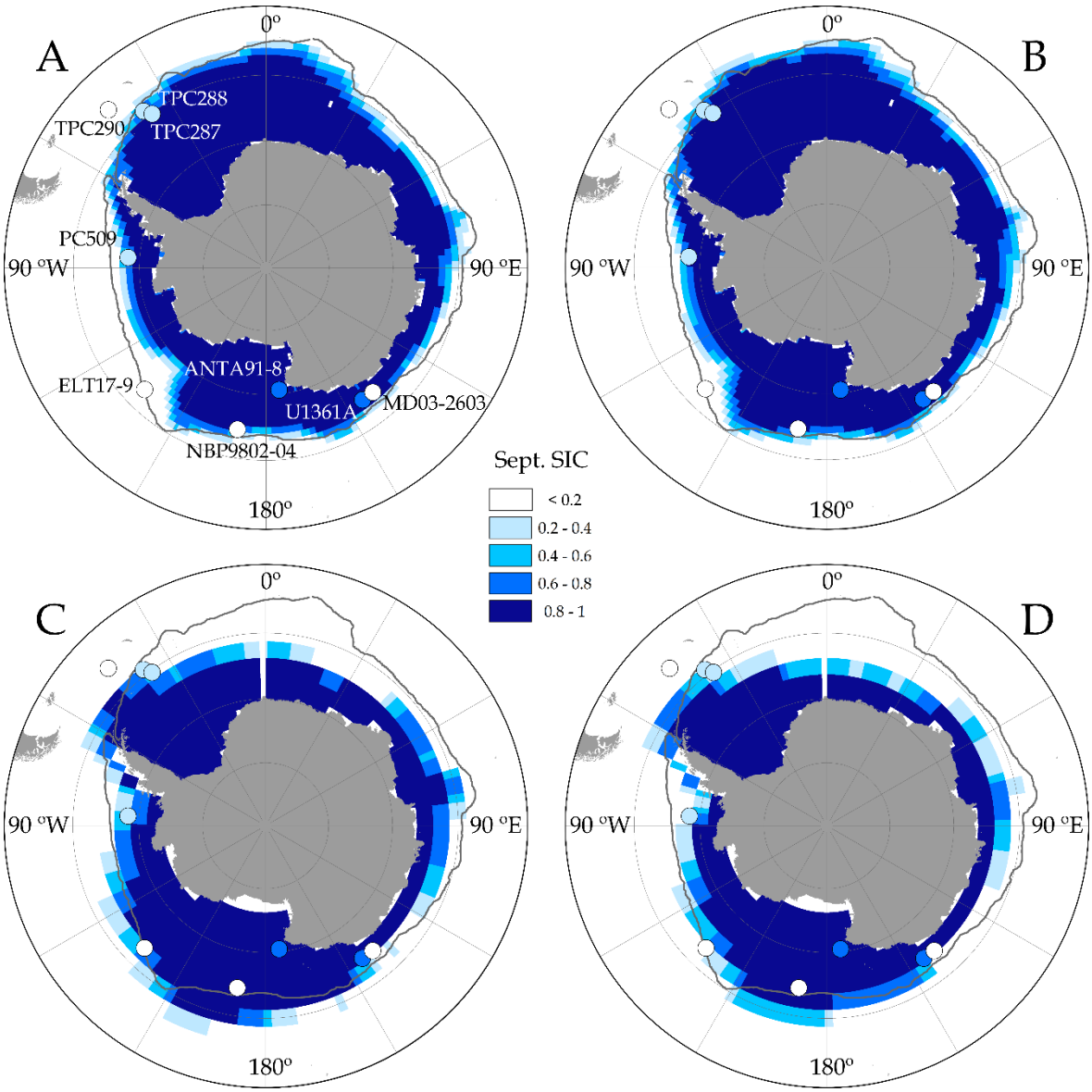

Figure 5.2 Maps of September $SICs_{model}$ for Peak MIS 5e. **A -** LIG_HG. **B** - H11(250)_HG. **C** - H11(250)_HC (Holloway et al. 2018). **D** - H11(1600)_HC (Holloway et al. 2018). Coloured circles on all maps represent the September $SICs_{proxy}$ in nine marine sediment cores (Chadwick et al. 2021). The grey line on all maps marks the modern (1981-2010) median September sea-ice extent (Fetterer et al. 2017).

Within the ±1.1 °C uncertainty on the diatom transfer function $SSST_{proxy}$ values, the Peak MIS 5e – PI $SSST_{proxy}$ anomalies in all Pacific sector cores (ELT17-9, NBP9802-04, PC509 and ANTA91-8) match the H11(1600)_HC run (Table 5.1 & Figure 5.1d). Proxy data for core PC509 also matches the other three model outputs in this study (Table 5.1) and the proxy data in both cores ELT17-9 and ANTA91-8 matches the LIG_HG run (Table 5.1). The transfer function Peak MIS 5e $SSST_{proxy}$ anomaly in core U1361A also matches, within uncertainty, the values from all four model runs (Table 5.1). The transfer function $SSST_{proxy}$ anomalies in cores TPC290, TPC288, TPC287 and MD03-2603 do not

match with any of the model outputs considered here, with cores TPC288, TPC287 and MD03-2603 >2 °C warmer than all the models and core TPC290 >1.5 °C cooler than all the models (Table 5.1).

5.3.3 September $SICs_{model}$

The patterns of September $SICs_{model}$ are very similar between the LIG_HG and H11(250)_HG simulations (Figure 5.2a & b), with the main difference a greater $WSIE_{model}$ in the H11(250)_HG run in the Pacific sector region 150-120 °W and in the Weddell Sea to the east of the Antarctic Peninsula (Figure 5.2b). The H11(250)_HC and H11(1600)_HC simulations both have a reduced $WSIE_{model}$ compared to the LIG_HG and H11(250)_HG runs, most notably in the eastern Weddell Sea (30 °W – 30 °E) where the WSI edge is >5 ° latitude further south than either of the LIG_HG or H11(250)_HG runs (Figure 5.2c & d). In the H11(1600)_HC run, the September $SICs_{model}$ are reduced compared to H11(250)_HC run, with the WSI edge 2-5 ° latitude further poleward in the H11(1600)_HC run (Figure 5.2d).

5.3.4 September $SICs_{proxy}$

Within the ±0.09 uncertainty on the transfer function September SIC_{proxy} values, the Peak MIS 5e September $SICs_{proxy}$ for most of the cores (TPC290, NBP9802-04, MD03-2603, U1361A, PC509 and ANTA91-8) do not match any of the model runs (Table 5.1, Figure 5.2). The proxy data in cores TPC288, TPC287 and ELT17-9 only matches the H11(1600)_HC simulation (Table 5.1). The pattern of September $SICs_{model}$ in the H11(1600)_HC simulation is also the best match with the transfer function values in the sediment cores (Figure 5.2d), with the greatest discrepancy the expansion of western Pacific sector (150 °E – 150 °W) $WSIE_{model}$, relative to the modern, in the H11(1600)_HC run, compared with the $WSIE_{proxy}$ reduction evident in the sediment core data (Figure 5.2d).

5.4 Discussion

5.4.1 $SSST_{model/proxy}$ anomalies

For the Pacific sector core sites (ELT17-9, NBP9802-04, PC509 and ANTA91-8) the best model-data match for $SSST_{model/proxy}$ anomalies is with the H11(1600)_HC run (Table 5.1 & Figure 5.1d), suggesting that the region south of 60 °S in this sector was largely 0.5-1 °C warmer than PI during Peak MIS 5e (Figure 5.1d). This $SSST_{model}$ anomaly is consistent with the more southerly SO core sites in Capron et al. (2017) and Chadwick et al. (2020) and suggests that the region south of the Antarctic Circumpolar Current (ACC) warmed less than the rest of the SO during MIS 5e. The better

match between the proxy data and the H11(1600)_HC simulation than between the proxy data and the H11(250)_HC simulation supports the need to run meltwater-hosed simulations for a longer duration than the 250 years in both the H11(250)_HG and H11(250)_HC runs.

The colder-than-PI Peak MIS 5e $SSST_{proxy}$ in core TPC290 is anomalous when compared to the nearby Atlantic sector cores TPC288 and TPC287, both of which are warmer during Peak MIS 5e than the PI (Figure 5.1 & Table 5.1). The cold Peak MIS 5e $SSST_{proxy}$ in core TPC290 is likely a result of high abundances of the diatom group *Chaetoceros* resting spores (rs.) during MIS 5e (Chadwick & Allen 2021h). This diatom group is associated with meltwater stratification (Crosta et al. 1997) and WSI (Armand et al. 2005) and is found in highest present day abundances along the Antarctic Peninsula. Therefore the high *Chaetoceros* rs. abundances in core TPC290 MIS 5e samples are likely to be misattributed to the colder conditions along the Antarctic Peninsula than to the Scotia Sea, where there are no modern samples in the transfer function reference dataset (Gersonde et al. 2005, Ferry et al. 2015a).

All the model runs in this study indicate warmer conditions at core site MD03-2603 than the nearby U1361A (Table 5.1), but none of them have a difference of more than 0.8 ^{o}C, whereas the transfer function $SSST_{proxy}$ anomalies are >3 ^{o}C warmer at core site MD03-2603 than U1361A (Table 5.1). The colder conditions around core U1361A could be due to increased melting of the Wilkes subglacial basin during MIS 5e (Wilson et al. 2018). The shelf bathymetry would likely funnel any colder glacial meltwaters towards U1361A rather than MD03-2603, promoting the difference in $SSST_{model/proxy}$ anomalies. However, this does not explain why the $SSST_{proxy}$ anomaly for core MD03-2603 is still >2 ^{o}C greater than any of the model results.

None of the model runs considered here recreate the ~2.7 ^{o}C $SSST_{proxy}$ anomaly in the Atlantic sector cores TPC288 and TPC287 (Table 5.1 & Figure 5.1). This discrepancy could be due to the meltwater hosed simulations not being run for enough years to get an equivalent warming signature. It could also be as a result of a poleward constriction of the northern limb of the Weddell Gyre not being recreated in the model runs. A constriction of the Weddell Gyre, as predicted by multiple CMIP5 models for warmer than present conditions (Wang 2013), would displace warm (>1.5 ^{o}C) ACC surface waters to the south during Peak MIS 5e, causing larger positive $SSST_{proxy}$ anomalies at cores TPC288 and TPC287 than if both cores had remained bathed by Weddell Sea surface waters during Peak MIS 5e.

The >2 ^{o}C $SSST_{proxy}$ anomalies in cores TPC288, TPC287 and MD03-2603 are greater than previously published $SSST_{proxy}$ anomalies from the region south of the Antarctic Polar Front (Capron et al. 2017, Chadwick et al. 2020) and contrasts with the pattern of decreased $SSST_{proxy}$ anomalies closer to the South Pole. The largest $SSST_{proxy}$ anomalies in the Capron et al. (2017) and Chadwick et al. (2020)

syntheses were found in cores that were bathed by different surface water masses during MIS 5e compared to present/PI (Chadwick et al. 2020). The small (<1.5 ^{o}C) $SSST_{proxy}$ anomalies in the most southerly records from Capron et al. (2017) and Chadwick et al. (2020) were therefore due to these records coming from cores that are within the same oceanographic zone during MIS 5e as during both the present and PI (Chadwick et al. 2020). The >2 ^{o}C $SSST_{proxy}$ anomalies in cores TPC288, TPC287 and MD03-2603 are likely due to these cores being bathed by different surface water masses during MIS 5e compared to the PI, caused by either changes in gyre extent, in the case of cores TPC288 and TPC287, or by movement of ACC fronts, in the case of core MD03-2603 (Chapter 4.6). Comparing the $SSST_{proxy}$ anomalies in the Atlantic and Indian sectors with the Pacific sector shows that there is strong longitudinal heterogeneity in $SSST_{proxy}$ anomalies in addition to the latitudinal heterogeneity identified by Chadwick et al. (2020).

5.4.2 September $SICs_{model/proxy}$

In the western Pacific (Ross Sea) sector all the model runs appear to overestimate Peak MIS 5e $WSIE_{model}$, with the H11(250)_HC and H11(1600)_HC runs even indicating an expansion in $WSIE_{model}$ relative to the modern (Figure 5.2c & d). The eastern Pacific sector has better model-data agreement, especially for the H11(250)_HG and H11(1600)_HC runs (Figure 5.2b & d). The shape of modern Pacific sector WSIE is strongly influenced by the position of the ACC and the shape and position of the Ross Sea Gyre (Nghiem et al. 2016), with the proxy data indicating a poleward movement of the ACC and contraction of the Ross Sea Gyre in the western Pacific sector which is less apparent in the models.

A similar poleward contraction of the Weddell Gyre during MIS 5e, as previously hypothesised with the $SSST_{proxy}$ anomalies in cores TPC288 and TPC287 (Chapter 5.4.1), would also help explain the shape of the $WSIE_{model}$ in the H11(250)_HC and H11(1600)_HC runs (Figure 5.2c & d), with a longitudinal constriction of the Weddell Gyre during MIS 5e also supported by proxy data from the western Indian sector (Ghadi et al. 2020). The shape of the eastern Indian sector $WSIE_{model}$ in the H11(250)_HC and H11(1600)_HC simulations in the proximity of cores MD03-2603 and U1361A (Figure 5.2c & d) is consistent with the greater Peak MIS 5e September SIC_{proxy} reconstructed for core U1361A than for core MD03-2603. High glacial meltwater flux can promote increased WSIE (Merino et al. 2018) and the shape of the eastern Indian sector WSIE therefore supports a large release of glacial meltwater from the Wilkes subglacial basin during MIS 5e (Wilson et al. 2018), which was channelled towards core U1361A rather than core MD03-2603, as discussed in Chapter 5.4.1. Many of the estimates of Peak MIS 5e September SIC_{proxy} have a good visual similarity to the models (Figure 5.2) but do not match the models within the transfer function uncertainty (Table 5.1). This discrepancy is due to the steep gradient in SIC fraction between 0.2 and 0.8 (Figure 5.2)

and therefore small variations in the position of the WSI edge can make a large difference to the Peak MIS 5e September $SIC_{model/proxy}$ at most of the core sites.

5.5 Conclusions

Comparing four HadGEM3 and HadCM3 simulations of Peak MIS 5e September $SICs_{model}$ and $SSST_{model}$ anomalies to diatom transfer function estimates at nine marine sediment core sites, show that the best match with the proxy data is provided by the H11(1600)_HC simulation. This simulation has good agreement with Peak MIS 5e – PI $SSST_{proxy}$ anomalies in the Pacific sector and with Peak MIS 5e September $SICs_{proxy}$ in the Atlantic sector (Figure 5.1d, Figure 5.2d & Table 5.1). The better model-data agreement for the H11(1600)_HC run than for the H11(250)_HC run supports the importance of including longer duration North Atlantic meltwater hosing in future models of Peak MIS 5e climate. The importance of meltwater hosing duration also suggests that the poor match between the proxy data and the H11(250)_HG simulation is due to the short run length and that the H11(250)_HG output is more reflective of the conditions at ~133 ka (Marino et al. 2015, Holloway et al. 2018) than 130-128 ka.

In the Pacific sector, both the proxy data and the H11(1600)_HC run indicate a Peak MIS 5e $SSST_{model/proxy}$ warming of ~0.5-1 ^{o}C relative to the PI and a relatively small reduction in the Peak MIS 5e $WSIE_{model/proxy}$ compared to the modern (Figure 5.2d). However, the proxy data for the western Pacific sector indicates a greater $WSIE_{proxy}$ reduction during Peak MIS 5e than any of the model runs (Figure 5.2). Both the proxy data and the H11(1600)_HC simulation indicate a greater reduction in Peak MIS 5e $WSIE_{model/proxy}$ in the Atlantic sector than in the Pacific sector, especially in the eastern Atlantic sector (Figure 5.2d). However, the Peak MIS 5e $SSST_{proxy}$ anomalies in the Atlantic sector cores TPC288 and TPC287 are >1.9 ^{o}C greater than any of the model outputs (Figure 5.1 & Table 5.1). The model-data discrepancies in both western Pacific sector $WSIE_{model/proxy}$ and Atlantic sector $SSST_{model/proxy}$ anomalies are suggested to be due to poleward contractions in the Ross and Weddell Gyres, respectively, which are not fully realised in the models. A CMIP3 and CMIP5 model ensemble by Wang (2013) identified that subpolar gyre areal extent displays a diverse response to warmer-than-present climatic conditions, with trends varying from a 23 x 10^{10} m^2/decade decrease to a 69 x 10^{10} m^2/decade increase between models.

In the eastern Indian sector both the H11(1600)_HC simulation and proxy data indicate that the more easterly core U1361A had a cooler $SSST_{model/proxy}$ anomaly and greater September $SIC_{model/proxy}$ during Peak MIS 5e than core MD03-2603 (Figure 5.1d, Figure 5.2d & Table 5.1). This difference supports the hypothesis that increased melting of the Wilkes subglacial basin occurred during MIS 5e (Wilson et al. 2018) with the cold and fresh glacial meltwaters channelled by shelf bathymetry

and the ACC over core U1361A, but not core MD03-2603, promoting increased $WSIE_{model/proxy}$ and reduced $SSST_{model/proxy}$ anomalies at the former.

The response of the Atlantic Meridional Overturning Circulation (AMOC) to H11 meltwater input in HadGEM3 simulations is almost immediate, with an abrupt decrease in AMOC within 25 years. The AMOC strength reaches a new equilibrium after 150 years, however associated heat changes continue after this time (Guarino et al. 2022, *in review*). As the AMOC weakens, less heat is transported northward. Surface waters of the North Atlantic cool for around 50-80 years, with deeper waters taking longer to reach a new equilibrium (Guarino et al. 2022, *in review*). These changes in advective heat transport may take 1000s of years to produce stable temperature anomalies in deep water output with the North Atlantic (Guarino et al. 2022, *in review*). Slow diffusive heat transfer across the ACC also causes a ~200 (or more) year lag between H11 freshwater input to the North Atlantic and the onset of (possible) Southern Ocean warming south of the ACC (Pedro et al. 2018). This slow diffusive heat transfer across the ACC also means that after 250 years of the H11 meltwater-forced HadGEM3 simulation, whilst the Southern Ocean north of the ACC is still warming at a linear rate (Guarino et al. 2022, *in review*), south of the ACC there is not yet evidence of significant warming. This suggests that longer duration model runs are required to establish the full Southern Ocean warming anomaly induced by H11-induced AMOC weakening.

Running the meltwater hosed H11(250)_HG simulation for a longer duration, ideally 3-4 ka (Marino et al. 2015), is crucial for investigating how well the latest simulations match with the Peak MIS 5e conditions reconstructed from marine sediment cores. Whilst the existing evidence suggests that H11 meltwater forcing is required to get a match between the models and proxy data, the current model run-duration is too short for us to know whether state of the art models are capable of matching the Peak MIS 5e conditions evidenced by the proxy data. Of particular interest in the analysis of longer HadGEM3 runs would be to assess whether the model would resolve the greater reduction in the Atlantic sector $WSIE_{model/proxy}$ seen in both sediment core data (Chapters 3 & 4) and previous models (Holloway et al. 2017, Holloway et al. 2018) but absent from either the LIG_HG or H11(250)_HG simulations (Figure 5.2a & b).

Chapter 6 Conclusions and Future Work

This thesis aimed to reconstruct the palaeoenvironmental conditions in the Southern Ocean (SO) during MIS 5e with the main focus on the spatial and temporal patterns of winter sea-ice (WSI) change during this period. By analysing marine sediment cores located further south than previous publications (Chapter 2), extra insight has been gained into the winter sea-ice extent (WSIE) during MIS 5e and the processes that drive/influence changes in WSIE. Because MIS 5e represents a 'process analogue' for a future warmer climate (Chapter 1.2) my conclusions are important to understand the dynamics and impacts of Antarctic sea ice in a warmer climate to improve the model accuracy for future anthropogenic warming simulations.

A synthesis of the new MIS 5e palaeoenvironmental reconstructions and model comparisons for each SO sector are presented before a discussion of potential future work to address outstanding questions.

6.1 Atlantic sector

The proxy records indicate minimum WSIE and maximum sea-surface temperatures (SSTs) in the Atlantic sector occur early (130-128 ka) during MIS 5e and coincident, within chronological uncertainty, with the peak Antarctic air temperatures and minimum sea-salt sodium flux in Antarctic ice cores (Chapter 2 & Chapter 4). At this time there is also a peak in austral winter insolation which suggests that short, mild austral winters may help drive a reduction in Atlantic sector WSIE (Chapter 2). Both the WSI edge and the fronts of the Antarctic Circumpolar Current (ACC) were located more than 3-5 ^{o} further south than their modern position in the Atlantic sector (Chapter 2 & Chapter 4). There is also evidence of a poleward contraction of the Weddell Gyre early during MIS 5e, with core TPC287 located north of the Weddell Gyre after ~130 ka (Chapter 3).

A contraction of the Weddell Gyre would promote the advection of relatively warm Circumpolar Deep Water onto the continental shelf (Fogwill et al. 2014) and a reduced WSIE would reduce brine rejection and may decrease rates of deep and bottom water formation in the Weddell Sea, causing a warming of abyssal waters (Marzocchi & Jansen 2019). Warmer shelf waters would promote the basal melting of ice shelves and marine terminating ice streams in the Weddell Sea causing their retreat and substantial Antarctic ice sheet mass loss (Hellmer et al. 2012, Wahlin et al. 2021).

Substantial ice sheet mass loss at ~126 ka caused an increased flux of both meltwater and icebergs into the Weddell Sea and promoted the re-expansion of WSIE through surface stratification (Chapter 3). This meltwater release is also coincident with an increased global sea-level, further

supporting the magnitude of the freshwater release from Antarctic ice sheets at 126-124 ka. An outstanding question is whether the majority of this ice sheet mass loss came from a collapse of the West Antarctic Ice Sheet (WAIS) or whether an East Antarctic subglacial basin (e.g. Recovery Basin) could be the primary source.

The latest model simulations do not show the MIS 5e SST warming and WSI retreat in the SW Atlantic sector, even with the inclusion of Heinrich 11 (H11) meltwater hosing in the North Atlantic (Chapter 5). However, the H11 event likely lasted for ~3-4 ka (Marino et al. 2015), whereas the current HadGEM3 simulations are only run for up to 250 years and therefore longer simulation run times could resolve this discrepancy.

6.2 Indian sector

Both WSIE and SSTs from proxy records in the Indian sector display millennial-scale variability (Chapter 4), with a SST maximum (WSIE minimum) occurring in the 130-128 ka interval (Chapter 2 & Chapter 4), concurrent with the maximum SSTs (minimum WSIE) and Antarctic air temperatures (sea-salt sodium flux) observed in the Atlantic sector records and Antarctic ice core records, respectively. Within this millennial-scale variability, there appears to be a greater frequency of intervals with high SSTs and reduced WSIE after 124 ka (Chapter 4). In the eastern Indian sector the average WSIE during MIS 5e is similar, although slightly reduced, compared to the modern day (Chapter 3), indicating that the long term position of the WSI edge in this region is largely resilient under warmer climates but with short duration retreat and advance events at the millennial-scale.

Along the modern day Wilkes Land margin the ACC flows much closer to the coast than in other regions of Antarctica (Figure 1.2) and experiences high variability in modern frontal positions (Kim & Orsi 2014). This variability in ACC frontal positions and flow-path could explain the millennial-scale variability in WSIE and SSTs for core MD03-2603, with periods of reduced WSIE and higher SSTs caused by poleward migration of the ACC (Chapter 4). Intervals when the ACC was located further south would also have had more southerly precipitation fields, causing drier conditions across Southern Australia (Liu & Curry 2010, Saunders et al. 2012), as can be seen in the present day (CSIRO 2018) in a trend that is likely to be further exacerbated by future warming.

Poleward shifts of the ACC during MIS 5e could also promote advection of Circumpolar Deep Water onto the Antarctic continental shelf, as in the Atlantic sector (Chapter 6.1), and drive intervals of increased basal melting of the Wilkes subglacial basin. The cold glacial meltwater produced by this melting would be funnelled by local shelf bathymetry towards core U1361A but not core MD03-2603, accounting for the cooler SSTs and increased WSIE recorded in core U1361A compared with MD03-2603 (Chapter 5).

6.3 Pacific sector

Unlike in the Atlantic and Indian sectors, both WSIE and SSTs in the Pacific sector display low variability throughout MIS 5e, especially in the cores located south of the modern Antarctic Polar Front (Chapter 3 & Chapter 4). There are no prominent minima or maxima in WSIE or SSTs for the more southerly cores during MIS 5e, but multiple of the more northerly cores reach peak SSTs late (after 123 ka) in MIS 5e, although these late maxima are likely due to local oceanographic influences (Chapter 2). In the central and western Pacific sector the MIS 5e WSI edge was located >2 ° south of its modern position whereas in the Bellingshausen Sea region the WSI edge was displaced <2 ° south of its modern position during MIS 5e (Chapter 4). This greater WSIE reduction in the western Pacific sector compared to the eastern Pacific sector is not reproduced in the MIS 5e simulation from state of the art climate models (Chapter 5).

In the modern Pacific sector, the WSIE is strongly influenced by the position of the ACC (Nghiem et al. 2016) and heterogeneous southerly displacement of the ACC during MIS 5e could explain the differential retreat of the WSI edge across the Pacific sector (Chapter 3 & Chapter 4). Bathymetric pinning of the ACC on the Pacific-Antarctic Ridge during MIS 5e limits the retreat of the WSI edge in the Pacific sector compared to the Atlantic and Indian sectors and also restricts the millennial-scale migrations seen in the Indian sector WSI and SST records.

The relatively stable WSIE in the Bellingshausen Sea during MIS 5e (Chapter 4) and a dearth of evidence for substantial meltwater flux in this region (Chapter 3), in contrast to the Atlantic sector, suggests that there was no major outflow of glacial meltwater into the Bellingshausen Sea from the WAIS during MIS 5e. Therefore, if the WAIS did collapse, as hypothesised (Pollard & DeConto 2009), during MIS 5e then the surviving ice sheet configuration would likely be more consistent with the pattern in Clark et al. (2020) than in DeConto & Pollard (2016), with ice sheet retreat dominantly discharged through the Weddell Sea and Amundsen Sea outflow glaciers and ice streams.

6.4 Discussion of potential future work

In this thesis I have identified both spatial and temporal heterogeneity in the responses of Antarctic WSI and SO SSTs to the warmer-than-present conditions during MIS 5e. However, there are still several outstanding gaps in our knowledge/understanding that would benefit from targeted future work:

1. Identifying which spatial gaps in the circum-Antarctic reconstruction of MIS 5e WSIE are the most important to target for new WSI reconstructions.

2. Further testing of whether state of the art climate models are able to accurately reproduce proxy reconstructions of MIS 5e WSIE and SSTs.
3. Investigating whether the spatial patterns and trends in WSIE during MIS 5e are maintained across a full glacial-interglacial cycle and/or are consistent with older warm periods.

Despite the substantial improvements made in this thesis, there are still regions of the SO, especially 30 ^{o}W – 120 ^{o}E, where the MIS 5e minimum WSIE remains poorly constrained. Whilst a general increase in the number of MIS 5e sea-ice records from south of the Antarctic Polar Front will clearly help further constrain WSIE there are specific regions of the SO that are of particular interest. One of these regions is the eastern Atlantic sector (20 ^{o}W – 20 ^{o}E), the major outflow of the Weddell Gyre (Vernet et al. 2019), where model simulations reconstruct very dissimilar WSIEs during MIS 5e (Chapter 5) and there is evidence of Weddell Gyre contraction during MIS 5e (Ghadi et al. 2020). In this region ACC fronts also display low modern variability (Kim & Orsi 2014) and as such, any changes in front position during MIS 5e relative to their present position would be more significant than in regions with high modern seasonal and interannual front variability. The Weddell Sea is a particularly critical region for reconstructing and understanding MIS 5e sea-ice dynamics because it is a major site of Antarctic Bottom Water formation and has the highest area-normalised primary productivity rates in the present day SO (Vernet et al. 2019).

Another important region for further investigation is the Amundsen Sea, where additional records would help elucidate whether the WSI in this region is as resilient to warming as in the rest of the Pacific sector and whether there was significant glacial meltwater flux from the WAIS into the Amundsen Sea during MIS 5e. A limitation to investigating the Amundsen Sea region is that diatom assemblages in marine sediment cores from this area correspond to environmental conditions found further to the north (Konfirst et al. 2012), suggesting a poleward transport of diatoms to these cores that prevents accurate reconstruction of past environmental changes. Poleward transport of diatoms during their downward flux to the seafloor can be modelled using Lagrangian particle analysis to predict the most likely origin point for those diatoms (Monroy et al. 2017, van Sebille et al. 2018). This would allow for the reconstructed environmental conditions at a core site to be compared with the modern conditions at the most probable surface ocean origin point. However, this technique is complicated by any changes in transport over time, specifically, it is unlikely that the transport pathways active during interglacial periods are the same as during glacial periods.

Ideally, new MIS 5e sea-ice records would be sought from more proximal locations to the Antarctic continent, along the slope and rise. This would both introduce southerly constraints on the position of the MIS 5e WSI edge and help constrain the MIS 5e summer sea-ice extent. However, cores

located more proximally to the continent, especially upon the shelf, are more likely to have been overridden by ice sheets during the Last Glacial Maximum and reworked the sediments deposited during MIS 5e. Also, as discussed in Chapter 1.3, cores located under higher WSI concentrations (>75 %) are biased by substantial dissolution of the diatom assemblage, limiting the ability to accurately reconstruct the environmental conditions. Cores that are under heavy WSI cover and located proximally to the continent also have less reliable stratigraphies due to the low input and preservation of biogenic material as well as hiatuses caused by Antarctic ice sheet growth over the shelf.

Alongside, new sea-ice records for MIS 5e, records from other proxies should be considered to test the impacts on ocean circulation from the reconstructed WSIE changes during MIS 5e (Chapters 2-5). The reduction in deep- and bottom-water mass formation as a result of a reduced WSIE, and the subsequent slowing in global ocean circulation, can be investigated using authigenic uranium, as a proxy for bottom-water oxygenation (Hayes et al. 2014), sortable silt, as a proxy for bottom water flow speeds (Williams et al. 2021), and the isotopic ratio of neodymium, as a proxy for the source region of deep- and bottom-water masses (Williams et al. 2021). The hypothesised slowdown in SO circulation and shallowing and slowdown in Atlantic Meridional Overturning Circulation during MIS 5e would be expected to cause a decrease in bottom-water oxygenation and flow speeds, causing an increase in authigenic uranium (Hayes et al. 2014) and a fining of the sortable silt average grain size. Reduced ocean circulation would also inhibit mixing in the abyssal ocean and likely cause an increase in the isotopic ratio of neodymium to more radiogenic values.

Ideally, new marine sediment core records to investigate the SO WSIE during MIS 5e would be located within the seasonal sea-ice zone and preserve >50 cm of sediment covering the end of Termination II and the peak of MIS 5e, equating to an average sedimentation rate of >4 cm/ka. The bulk of the sediment would be a diatomaceous ooze but with sufficient carbonate material to allow for a benthic $\delta^{18}O$ record to be reconstructed, despite the paucity of carbonate-bearing sediments south of 50 ^{o}S and deeper than 3500 m in the SO (Dutkiewicz et al. 2015). Correlating a benthic $\delta^{18}O$ record to the LR04 stack gives a more precise chronology than utilising the correlation of the sediment core magnetic susceptibility record to the EDC ice core dust record because it provides tiepoints within MIS 5, whereas the EDC dust record has no notable variations between 130 and 70 ka. Alongside the $\delta^{18}O$ correlation, the ideal core chronology would also incorporate biostratigraphic markers (e.g. *Rouxia leventerae* (Zielinski et al. 2002), *Hemidiscus karstenii* (Burckle et al. 1978)) and elemental ratios such as Ba/Ti, a proxy for biological productivity that could help distinguish MIS 5e from other MIS 5 substages.

Another gap in our knowledge/understanding, identified in Chapter 5, is whether state of the art climate models are able to reproduce the MIS 5e WSIE and SSTs reconstructed from the sediment core records. The latest Peak MIS 5e simulations are a poor match to SO proxy data (Chapter 5 & Otto-Bliesner et al. (2021)) but were only run for up to 1600 years with North Atlantic H11 meltwater forcing included, with the majority run for a much shorter duration. Longer (~3-4 ka) simulation run lengths, incorporating an H11 meltwater event, are required to further test whether the latest model physics can reconstruct the MIS 5e environmental conditions evident in the proxy data. It is also important to run future model simulations incorporating meltwater release from the Antarctic ice sheet, especially in the Weddell Sea region where I have interpreted a high iceberg and meltwater flux during MIS 5e (Chapter 3). This Antarctic ice sheet meltwater release would be expected to initially cause an increase in MIS 5e WSIE, as seen in the Atlantic sector sea-ice records in Chapter 4, before being outweighed by the influence of warming sea-surface and atmospheric temperatures. Modern Southern Hemisphere sea-ice dynamics in climate models also likely need improving given they are not able to reliably recreate even the general trends in Antarctic sea-ice cover (Rosenblum & Eisenman 2017).

A third gap in our knowledge is whether the differing WSI sensitivities and patterns between the three SO sectors during MIS 5e are maintained throughout a full glacial-interglacial cycle or during other older warm periods. Analysing long duration sea-ice records from across the SO can help investigate if the more dynamic WSIE in the Atlantic sector and the seeming resilience of Pacific sector WSIE are features of a full glacial-interglacial cycle. Further back in time, MIS 11c (~395-430 ka) provides an opportunity to test how the behaviour of Antarctic sea ice compares between MIS 5e and a previous exceptionally warm interglacial (Berger et al. 2016). However, investigating older time periods than MIS 5e is limited by the applicability of the diatom transfer function further back in time than ~135 ka due to increasing abundances of extinct diatom species (e.g. *R. leventerae*) for which there are no modern analog assemblages to compare to. Additionally, uncertainties in the configuration of Antarctic ice sheets and global ocean circulation during older time intervals further limits our ability to investigate climatic feedbacks and forcings during other, older interglacials.

The importance of investigating SO WSI variations and their relationship to other environmental variables has been identified by multiple PAGES scientific working groups (e.g. CLIVASH2k (Thomas et al. 2019), C-SIDE (Chadwick et al. 2019)). The targeted work of these groups will expand our understanding of past changes in SO sea ice and, combined with my work on MIS 5e, help to constrain the predicted impacts of future anthropogenic warming on Southern Hemisphere and global climate.

Bibliography

Abbott M.R., Richman J.G., Letelier R.M. & Bartlett J.S. 2000. The spring bloom in the Antarctic Polar Frontal Zone as observed from a mesoscale array of bio-optical sensors. *Deep-Sea Research II*, **47**: 3285-3314.

Abernathey R.P., Cerovecki I., Holland P.R., Newsom E., Mazloff M. & Talley L.D. 2016. Water-mass transformation by sea ice in the upper branch of the Southern Ocean overturning. *Nature Geoscience*, **9** (8): 596-601.

Allen C.S. 2014. Proxy development: a new facet of morphological diversity in the marine diatom *Eucampia antarctica* (Castracane) Mangin. *Journal of Micropalaeontology*, **33** (2): 131-142.

Allen C.S., Pike J., Pudsey C.J. & Leventer A. 2005. Submillennial variations in ocean conditions during deglaciation based on diatom assemblages from the southwest Atlantic. *Paleoceanography*, **20** (2): 1-16.

Armand L. & Leventer A. 2003. Palaeo Sea Ice Distribution - Reconstruction and Palaeoclimatic Significance. In: *Sea Ice: An Introduction to its Physics, Chemistry, Biology and Geology***:** 333-372.

Armand L. & Leventer A. 2010. Palaeo sea ice distribution and reconstruction derived from the geological records. In: *Sea Ice, 2nd edition*, Thomas D.N. & Dieckmann G.S. Eds. Wiley-Blackwell**:** 469-529.

Armand L.K., Crosta X., Romero O. & Pichon J.-J. 2005. The biogeography of major diatom taxa in Southern Ocean sediments: 1. Sea ice related species. *Palaeogeography, Palaeoclimatology, Palaeoecology*, **223** (1-2): 93-126.

Armand L.K. & Zielinski U. 2001. Diatom species of the genus *Rhizosolenia* from Southern Ocean sediments: distribution and taxonomic notes. *Diatom research*, **16** (2): 259-294.

Atkinson A., Hill S.L., Pakhomov E.A., Siegel V., Anadon R., Chiba S., Daly K.L., Downie R., Fielding S., Fretwell P., Gerrish L., Hosie G.W., Jessopp M.J., Kawaguchi S., Krafft B.A., Loeb V., Nishikawa J., Peat H.J., Reiss C.S., Ross R.M., Quetin L.B., Schmidt K., Steinberg D.K., Subramaniam R.C., Tarling G.A. & Ward P. 2017. KRILLBASE: a circumpolar database of Antarctic krill and salp numerical densities, 1926–2016. *Earth System Science Data*, **9** (1): 193-210.

Bakker P., Masson-Delmotte V., Martrat B., Charbit S., Renssen H., Gröger M., Krebs-Kanzow U., Lohmann G., Lunt D.J., Pfeiffer M., Phipps S.J., Prange M., Ritz S.P., Schulz M., Stenni B., Stone E.J. & Varma V. 2014. Temperature trends during the Present and Last Interglacial periods – a multi-model-data comparison. *Quaternary Science Reviews*, **99**: 224-243.

Barbara L., Crosta X., Leventer A., Schmidt S., Etourneau J., Domack E. & Massé G. 2016. Environmental responses of the Northeast Antarctic Peninsula to the Holocene climate variability. *Paleoceanography*, **31** (1): 131-147.

Bareille G., Grousset F.E., Labracherie M., Labeyrie L.D. & Petit J.-R. 1994. Origin of detrital fluxes in the southeast Indian Ocean during the last climatic cycles. *Paleoceanography*, **9** (6): 799-819.

Barrows T.T., Juggins S., De Deckker P., Calvo E. & Pelejero C. 2007. Long-term sea surface temperature and climate change in the Australian-New Zealand region. *Paleoceanography*, **22** (2): PA2215.

Bazin L., Landais A., Lemieux-Dudon B., Toyé Mahamadou Kele H., Veres D., Parrenin F., Martinerie P., Ritz C., Capron E., Lipenkov V., Loutre M.F., Raynaud D., Vinther B., Svensson A.,

Rasmussen S.O., Severi M., Blunier T., Leuenberger M., Fischer H., Masson-Delmotte V., Chappellaz J. & Wolff E. 2013a. Carbon dioxide composite data on AICC2012 chronology. *PANGAEA*.

Bazin L., Landais A., Lemieux-Dudon B., Toyé Mahamadou Kele H., Veres D., Parrenin F., Martinerie P., Ritz C., Capron E., Lipenkov V., Loutre M.F., Raynaud D., Vinther B., Svensson A., Rasmussen S.O., Severi M., Blunier T., Leuenberger M., Fischer H., Masson-Delmotte V., Chappellaz J. & Wolff E. 2013b. An optimized multi-proxy, multi-site Antarctic ice and gas orbital chronology (AICC2012): 120-800 ka. *Climate of the Past*, **9** (4): 1715-1731.

Beans C., Hecq J.H., Koubbi P., Vallet C., Wright S. & Goffart A. 2008. A study of the diatom-dominated microplankton summer assemblages in coastal waters from Terre Adélie to the Mertz Glacier, East Antarctica (139°E–145°E). *Polar Biology*, **31** (9): 1101-1117.

Becquey S. & Gersonde R. 2003. A 0.55-Ma paleotemperature record from the Subantarctic zone: Implications for Antarctic Circumpolar Current development. *Paleoceanography*, **18** (1): 1014-1028.

Belkin I.M. & Gordon A.L. 1996. Southern Ocean fronts from the Greenwich meridian to Tasmania. *Journal of Geophysical Research: Oceans*, **101** (C2): 3675-3696.

Benz V., Esper O., Gersonde R., Lamy F. & Tiedemann R. 2016. Last Glacial Maximum sea surface temperature and sea-ice extent in the Pacific sector of the Southern Ocean. *Quaternary Science Reviews*, **146**: 216-237.

Bereiter B., Eggleston S., Schmitt J., Nehrbass-Ahles C., Stocker T.F., Fischer H., Kipfstuhl S. & Chappellaz J. 2015. Revision of the EPICA Dome C CO_2 record from 800 to 600 kyr before present. *Geophysical Research Letters*, **42** (2): 542-549.

Berger A., Crucifix M., Hodell D.A., Mangili C., McManus J.F., Otto-Bliesner B.L., Pol K., Raynaud D., Skinner L.C., Tzedakis P.C., Wolff E.W., Yin Q., Abe-Ouchi A., Barbante C., Brovkin V., Cacho I., Capron E., Ferretti P., Ganopolski A., Grimalt J.O., Honisch B., Kawamura K., Landais A., Margari V., Martrat B., Masson-Delmotte V., Mokeddem Z., Parrenin F., Prokopenko A.A., Rashid H. et al. 2016. Interglacials of the last 800,000 years. *Reviews of Geophysics*, **54** (1): 162-219.

Beyens L. & Denys L. 1982. Problems in diatom analysis of deposits: Allochtonous valves and fragmentation. *Geologie en Mijnbouw*, **61**: 159-162.

Bianchi C. & Gersonde R. 2002. The Southern Ocean surface between Marine Isotope Stages 6 and 5d: Shape and timing of climate changes. *Palaeogeography, Palaeoclimatology, Palaeoecology*, **187**: 151-177.

Biastoch A., Boning C.W., Schwarzkopf F.U. & Lutjeharms J.R. 2009. Increase in Agulhas leakage due to poleward shift of Southern Hemisphere westerlies. *Nature*, **462** (7272): 495-498.

Bintanja R., van Oldenborgh G.J., Drijfhout S.S., Wouters B. & Katsman C.A. 2013. Important role for ocean warming and increased ice-shelf melt in Antarctic sea-ice expansion. *Nature Geoscience*, **6** (5): 376-379.

Bouttes N., Paillard D. & Roche D.M. 2010. Impact of brine-induced stratification on the glacial carbon cycle. *Climate of the Past*, **6** (5): 575-589.

Boyd P.W., Crossley A.C., DiTullio G.R., Griffiths F.B., Hutchins D.A., Queguiner B., Sedwick P.N. & Trull T.W. 2001. Control of phytoplankton growth by iron supply and irradiance in the subantarctic Southern Ocean: Experimental results from the SAZ Project. *Journal of Geophysical Research: Oceans*, **106** (C12): 31573-31583.

Brambati A., Melis R., Quaia T. & Salvi G. 2002. Late Quaternary climatic changes in the Ross Sea area, Antarctica. In: *Antarctica at the close of a Millenium*, Gamble J.A., Skinner D.N.B. & Henrys S. Eds. Proceedings Volume 8th International Symposium on Antarctic Earth Sciences, Royal Society of New Zealand Bulletin**:** 359-364.

Brathauer U. 1996. Radiolarians as indicators for Quaternary climatic changes in the Southern Ocean (Atlantic Sector). *Reports on Polar Research*, **216**: 1-163.

Brathauer U. & Abelmann A. 1999. Late Quaternary variations in sea surface temperatures and their relationship to orbital forcing recorded in the Southern Ocean (Atlantic sector). *Paleoceanography*, **14** (2): 135-148.

Brathauer U., Abelmann A., Gersonde R., Niebler H.-S. & Futterer D.K. 2001. Calibration of *Cycladophora davisiana* events versus oxygen isotope stratigraphy in the subantarctic Atlantic Ocean - a stratigraphic tool for carbonate-poor Quaternary sediments. *Marine Geology*, **175**: 167-181.

Brix H. & Gerdes R. 2003. North Atlantic Deep Water and Antarctic Bottom Water: Their interaction and influence on the variability of the global ocean circulation. *Journal of Geophysical Research: Oceans*, **108** (C2): 3022.

Bronselaer B., Winton M., Griffies S.M., Hurlin W.J., Rodgers K.B., Sergienko O.V., Stouffer R.J. & Russell J.L. 2018. Change in future climate due to Antarctic meltwater. *Nature*, **564** (7734): 53-58.

Burckle L.H. 1984. Ecology and paleoecology of the marine diatom *Eucampia antarctica* (Castr.) Mangin. *Marine Micropaleontology*, **9**: 77-86.

Burckle L.H. & Burak R.W. 1995. Relative abundance of *Eucampia antarctica* as a close proxy to $\delta^{18}O$ in upper Quaternary sediments of the Southern Ocean. In: *Landscapes and Life: Studies in Honour of Urve Miller*, Robertsson A.M. Ed., Cons. de L'Eur., Rixensart, Belgium**:** 15-22.

Burckle L.H. & Cirilli J. 1987. Origin of diatom ooze belt in the Southern Ocean; implications for late Quaternary paleoceanography. *Micropaleontology*, **33** (1): 82-86.

Burckle L.H., Clarke D.B. & Shackleton N.J. 1978. Isochronous last-abundant-appearance datum (LAAD) of the diatom *Hemidiscus karstenii* in the sub-Antarctic. *Geology*, **6**: 243-246.

Burckle L.H., Jacobs S.S. & McLaughlin R.B. 1987. Late austral spring diatom distribution between New Zealand and the Ross Ice Shelf, Antarctica: hydrography and sediment correlations. *Micropaleontology*, **33**: 74-81.

Burckle L.H. & Mortlock R. 1998. Sea-ice extent in the Southern Ocean during the Last Glacial Maximum: another approach to the problem. *Annals of Glaciology*, **27**: 302-304.

Burckle L.H., Robinson D. & Cooke D. 1982. Reappraisal of sea-ice distribution in Atlantic and Pacific sectors of the Southern Ocean at 18,000 yr BP. *Nature*, **299** (5882): 435-437.

Busch W.H. 1991. Analysis of wet-bulk density and sediment color cycles in Pliocene-Pleistocene sediments of the Owen Ridge (Site 722) and Oman Margin (Site 728). In: *Proceedings of the Ocean Drilling Program, Scientific Results*, Prell W.J. & Niitsuma N. Eds., College Station, TX (Ocean Drilling Program). **117:** 239-253.

Capron E., Govin A., Feng R., Otto-Bliesner B.L. & Wolff E.W. 2017. Critical evaluation of climate syntheses to benchmark CMIP6/PMIP4 127 ka Last Interglacial simulations in the high-latitude regions. *Quaternary Science Reviews*, **168**: 137-150.

Capron E., Govin A., Stone E.J., Masson-Delmotte V., Mulitza S., Otto-Bliesner B., Rasmussen T.L., Sime L.C., Waelbroeck C. & Wolff E.W. 2014. Temporal and spatial structure of multi-millennial temperature changes at high latitudes during the Last Interglacial. *Quaternary Science Reviews*, **103**: 116-133.

Carter L., McCave I.N. & Williams M.J.M. 2008. Circulation and Water Masses of the Southern Ocean: A Review. In: *Developments in Earth & Environmental Sciences*, Florindo F. & Siegert M. Eds. Elsevier, Amsterdam. **8:** 85-114.

Ceccaroni L., Frank M., Frignani M., Langone L., Ravaioli M. & Mangini A. 1998. Late Quaternary fluctuations of biogenic component fluxes on the continental slope of the Ross Sea, Antarctica. *Journal of Marine Systems*, **17**: 515-525.

Cefarelli A.O., Ferrario M.E., Almandoz G.O., Atencio A.G., Akselman R. & Vernet M. 2010. Diversity of the diatom genus *Fragilariopsis* in the Argentine Sea and Antarctic waters: morphology, distribution and abundance. *Polar Biology*, **33** (11): 1463-1484.

Chadwick M. 2020. Southern Ocean surface sediment diatom abundances. *Mendeley Data*.

Chadwick M. 2022. Age-model tiepoints for cores DSDP 594, MD88-770, MD02-2488, MD84-551, ODP site 1094, SO136-003, PS1768-8, PS2102-2 and MD97-2120. *Mendeley Data*.

Chadwick M. & Allen C.S. 2021a. Marine Isotope Stage 5e diatom assemblages in marine sediment core ANTA91-8 (-70.78 °N, 172.83 °E, Cruise ANTA91) - VERSION 2. *NERC EDS UK Polar Data Centre*.

Chadwick M. & Allen C.S. 2021b. Marine Isotope Stage 5e diatom assemblages in marine sediment core ELT17-9 (-63.08 °N, -135.12 °E, Cruise ELT17). *UK Polar Data Centre, Natural Environment Research Council, UK Research & Innovation*.

Chadwick M. & Allen C.S. 2021c. Marine Isotope Stage 5e diatom assemblages in marine sediment core MD03-2603 (-64.28 °N, 139.38 °E, Cruise MD130) *UK Polar Data Centre, Natural Environment Research Council, UK Research & Innovation*.

Chadwick M. & Allen C.S. 2021d. Marine Isotope Stage 5e diatom assemblages in marine sediment core NBP9802-04 (-64.20 °N, -170.08 °E, Cruise PA9802) *UK Polar Data Centre, Natural Environment Research Council, UK Research & Innovation*.

Chadwick M. & Allen C.S. 2021e. Marine Isotope Stage 5e diatom assemblages in marine sediment core PC509 (-68.31 °N, -86.03 °E, Cruise JR179). *UK Polar Data Centre, Natural Environment Research Council, UK Research & Innovation*.

Chadwick M. & Allen C.S. 2021f. Marine Isotope Stage 5e diatom assemblages in marine sediment core TPC287 (-60.31 °N, -36.65 °E, Cruise JR48) *UK Polar Data Centre, Natural Environment Research Council, UK Research & Innovation*.

Chadwick M. & Allen C.S. 2021g. Marine Isotope Stage 5e diatom assemblages in marine sediment core TPC288 (-59.14 °N, -37.96 °E, Cruise JR48) *UK Polar Data Centre, Natural Environment Research Council, UK Research & Innovation*.

Chadwick M. & Allen C.S. 2021h. Marine Isotope Stage 5e diatom assemblages in marine sediment core TPC290 (-55.55 °N, -45.02 °E, Cruise JR48). *UK Polar Data Centre, Natural Environment Research Council, UK Research & Innovation*.

Chadwick M. & Allen C.S. 2021i. Marine Isotope Stage 5e diatom assemblages in marine sediment core U1361A (-64.41 °N, 143.89 °E, IODP Exp. 318) *UK Polar Data Centre, Natural Environment Research Council, UK Research & Innovation*.

Chadwick M., Allen C.S. & Crosta X. 2021. MAT estimates of MIS 5e September sea-ice concentrations and summer SSTs. *PANGAEA*.

Chadwick M., Allen C.S., Sime L.C. & Hillenbrand C.D. 2020. Analysing the timing of peak warming and minimum winter sea-ice extent in the Southern Ocean during MIS 5e. *Quaternary Science Reviews*, **229**: 106134.

Chadwick M., Jones J., Lawler K.-A., Prebble J., Kohfeld K.E. & Crosta X. 2019. Understanding glacial-interglacial changes in Southern Ocean sea ice. *Past Global Changes Magazine*, **27** (2): 86.

Chase Z., Anderson R.F., Fleisher M.Q. & Kubik P.W. 2003. Accumulation of biogenic and lithogenic material in the Pacific sector of the Southern Ocean during the past 40,000 years. *Deep-Sea Research Part II: Topical Studies in Oceanography*, **50** (3-4): 799-832.

Chase Z., Kohfeld K.E. & Matsumoto K. 2015. Controls on biogenic silica burial in the Southern Ocean. *Global Biogeochemical Cycles*, **29**: 1599-1616.

Civel-Mazens M., Crosta X., Cortese G., Michel E., Mazaud A., Ther O., Ikehara M. & Itaki T. 2021. Antarctic Polar Front migrations in the Kerguelen Plateau region, Southern Ocean, over the past 360 kyrs. *Global and Planetary Change*, **202**: 103526.

Clark P.U., He F., Golledge N.R., Mitrovica J.X., Dutton A., Hoffman J.S. & Dendy S. 2020. Oceanic forcing of penultimate deglacial and last interglacial sea-level rise. *Nature*, **577** (7792): 660-664.

Cortese G., Dunbar G.B., Carter L., Scott G., Bostock H., Bowen M., Crundwell M., Hayward B.W., Howard W., Martínez J.I., Moy A., Neil H., Sabaa A. & Sturm A. 2013. Southwest Pacific Ocean response to a warmer world: Insights from Marine Isotope Stage 5e. *Paleoceanography*, **28** (3): 585-598.

Cremer H., Roberts D., McMinn A., Gore D. & Melles M. 2003. The Holocene Diatom Flora of Marine Bays in the Windmill Islands, East Antarctica. *Botanica Marina*, **46** (1): 82-106.

Crosta X., Pichon J.-J. & Labracherie M. 1997. Distribution of *Chaetoceros* resting spores in modern peri-Antarctic sediments. *Marine Micropaleontology*, **29**: 283-299.

Crosta X., Pichon J.J. & Burckle L.H. 1998. Application of modern analog technique to marine Antarctic diatoms: Reconstruction of maximum sea-ice extent at the Last Glacial Maximum. *Paleoceanography*, **13** (3): 284-297.

Crosta X., Romero O., Armand L.K. & Pichon J.-J. 2005. The biogeography of major diatom taxa in Southern Ocean sediments: 2. Open ocean related species. *Palaeogeography, Palaeoclimatology, Palaeoecology*, **223** (1-2): 66-92.

Crosta X., Sturm A., Armand L. & Pichon J.-J. 2004. Late Quaternary sea ice history in the Indian sector of the Southern Ocean as recorded by diatom assemblages. *Marine Micropaleontology*, **50** (3-4): 209-223.

CSIRO. 2018. State of the Climate. Australia, Bureau of Meteorology, 1-24.

de Jong J., Schoemann V., Lannuzel D., Croot P., de Baar H. & Tison J.-L. 2012. Natural iron fertilization of the Atlantic sector of the Southern Ocean by continental shelf sources of the Antarctic Peninsula. *Journal of Geophysical Research: Biogeosciences*, **117**: G01029.

Death R., Wadham J.L., Monteiro F., Le Brocq A.M., Tranter M., Ridgwell A., Dutkiewicz S. & Raiswell R. 2014. Antarctic ice sheet fertilises the Southern Ocean. *Biogeosciences*, **11** (10): 2635-2643.

DeConto R.M. & Pollard D. 2016. Contribution of Antarctica to past and future sea-level rise. *Nature*, **531** (7596): 591-597.

DeFelice D.R. 1979a. Relative diatom abundance as tool for monitoring winter sea ice fluctuations in southeast Atlantic. *Antarctic Journal of the United States*, **14** (5): 105-106.

DeFelice D.R. 1979b. Surface lithofacies, biofacies, and diatom diversity patterns as models for delineation of climatic change in the southeast Atlantic Ocean. PhD thesis: *Florida State University*.

Deppeler S.L. & Davidson A.T. 2017. Southern Ocean Phytoplankton in a Changing Climate. *Frontiers in Marine Science*, **4**: 40.

Diekmann B., Futterer D., Grobe H., Hillenbrand C.-D., Kuhn G., Michels K., Petschick R. & Pirrung M. 2003. Terrigenous Sediment Supply in the Polar to Temperate South Atlantic: Land-Ocean Links of Environmental Changes during the Late Quaternary. In: *The South Atlantic in the Late Quaternary: Reconstruction of Material Budgets and Current Systems*, Wefer G., Mulitza S. & Ratmeyer V. Eds. Springer-Verlag Berlin**:** 375-399.

Dong S., Sprintall J. & Gille S.T. 2006. Location of the Antarctic Polar Front from AMSR-E Satellite Sea Surface Temperature Measurements. *Journal of Physical Oceanography*, **36**: 2075-2089.

Dotto T.S., Naveira Garabato A., Bacon S., Tsamados M., Holland P.R., Hooley J., Frajka-Williams E., Ridout A. & Meredith M.P. 2018. Variability of the Ross Gyre, Southern Ocean: Drivers and Responses Revealed by Satellite Altimetry. *Geophysical Research Letters*, **45**: 6195-6204.

Dutkiewicz A., Müller R.D., O'Callaghan S. & Jónasson H. 2015. Census of seafloor sediments in the world's ocean. *Geology*, **43** (9): 795-798.

Dutton A., Carlson A.E., Long A.J., Milne G.A., Clark P.U., DeConto R., Horton B.P., Rahmstorf S. & Raymo M.E. 2015. Sea-level rise due to polar ice-sheet mass loss during past warm periods. *Science*, **349** (6244): aaa4019.

Esper O. & Gersonde R. 2014a. New tools for the reconstruction of Pleistocene Antarctic sea ice. *Palaeogeography, Palaeoclimatology, Palaeoecology*, **399**: 260-283.

Esper O. & Gersonde R. 2014b. Quaternary surface water temperature estimations: New diatom transfer functions for the Southern Ocean. *Palaeogeography, Palaeoclimatology, Palaeoecology*, **414**: 1-19.

Esper O., Gersonde R. & Kadagies N. 2010. Diatom distribution in southeastern Pacific surface sediments and their relationship to modern environmental variables. *Palaeogeography, Palaeoclimatology, Palaeoecology*, **287** (1-4): 1-27.

Favier L., Durand G., Cornford S.L., Gudmundsson G.H., Gagliardini O., Gillet-Chaulet F., Zwinger T., Payne A.J. & Le Brocq A.M. 2014. Retreat of Pine Island Glacier controlled by marine ice-sheet instability. *Nature Climate Change*, **4** (2): 117-121.

Ferrari R., Jansen M.F., Adkins J.F., Burke A., Stewart A.L. & Thompson A.F. 2014. Antarctic sea ice control on ocean circulation in present and glacial climates. *Proc Natl Acad Sci U S A*, **111** (24): 8753-8758.

Ferry A.J., Crosta X., Quilty P.G., Fink D., Howard W. & Armand L.K. 2015a. First records of winter sea ice concentration in the southwest Pacific sector of the Southern Ocean. *Paleoceanography*, **30** (11): 1525-1539.

Ferry A.J., Prvan T., Jersky B., Crosta X. & Armand L.K. 2015b. Statistical modeling of Southern Ocean marine diatom proxy and winter sea ice data: Model comparison and developments. *Progress in Oceanography*, **131**: 100-112.

Fetterer F., Knowles K., Meier W.N., Savoie M. & Windnagel A.K. 2017. Sea Ice Index, Version 3. *Boulder, Colorado USA*. NSIDC: National Snow and Ice Data Center.

Filippova A., Kienast M., Frank M. & Schneider R.R. 2016. Alkenone paleothermometry in the North Atlantic: A review and synthesis of surface sediment data and calibrations. *Geochemistry, Geophysics, Geosystems*, **17** (4): 1370-1382.

Fischer H., Meissner K.J., Mix A.C., Abram N.J., Austermann J., Brovkin V., Capron E., Colombaroli D., Daniau A.-L., Dyez K.A., Felis T., Finkelstein S.A., Jaccard S.L., McClymont E.L., Rovere A., Sutter J., Wolff E.W., Affolter S., Bakker P., Ballesteros-Cánovas J.A., Barbante C., Caley T., Carlson A.E., Churakova O., Cortese G., Cumming B.F., Davis B.A.S., de Vernal A., Emile-Geay J., Fritz S.C. et al. 2018. Palaeoclimate constraints on the impact of 2 °C anthropogenic warming and beyond. *Nature Geoscience*, **11** (7): 474-485.

Fletcher M.S. & Moreno P.I. 2011. Zonally symmetric changes in the strength and position of the Southern Westerlies drove atmospheric CO2 variations over the past 14 k.y. *Geology*, **39** (5): 419-422.

Fogwill C.J., Phipps S.J., Turney C.S.M. & Golledge N.R. 2015. Sensitivity of the Southern Ocean to enhanced regional Antarctic ice sheet meltwater input. *Earth's Future*, **3** (10): 317-329.

Fogwill C.J., Turney C.S.M., Meissner K.J., Golledge N.R., Spence P., Roberts J.L., England M.H., Jones R.T. & Carter L. 2014. Testing the sensitivity of the East Antarctic Ice Sheet to Southern Ocean dynamics: past changes and future implications. *Journal of Quaternary Science*, **29** (1): 91-98.

Forcada J. & Trathan P.N. 2009. Penguin responses to climate change in the Southern Ocean. *Global Change Biology*, **15** (7): 1618-1630.

Freeman N.M., Lovenduski N.S. & Gent P.R. 2016. Temporal variability in the Antarctic Polar Front (2002-2014). *Journal of Geophysical Research: Oceans*, **121**: 7263-7276.

Fryxell G.A. & Prasad A.K.S.K. 1990. *Eucampia antarctica* var. *recta* (Mangin) stat. nov. (Biddulphiaceae, Bacillariophyceae): life stages at the Weddell Sea ice edge. *Phycologia*, **29** (1): 27-38.

Gardner A.S., Moholdt G., Scambos T., Fahnstock M., Ligtenberg S., van den Broeke M. & Nilsson J. 2018. Increased West Antarctic and unchanged East Antarctic ice discharge over the last 7 years. *The Cryosphere*, **12** (2): 521-547.

Garrison D.L., Sullivan C.W. & Ackley S.F. 1986. Sea-ice microbial communities in Antarctica. *Bioscience*, **36**: 243-250.

Gersonde R., Abelmann A., Brathauer U., Becquey S., Bianchi C., Cortese G., Grobe H., Kuhn G., Niebler H.S., Segl M., Sieger R., Zielinski U. & Fütterer D.K. 2003. Last glacial sea surface temperatures and sea-ice extent in the Southern Ocean (Atlantic-Indian sector): A multiproxy approach. *Paleoceanography*, **18** (3): 1061.

Gersonde R., Crosta X., Abelmann A. & Armand L. 2005. Sea-surface temperature and sea ice distribution of the Southern Ocean at the EPILOG Last Glacial Maximum—a circum-Antarctic view based on siliceous microfossil records. *Quaternary Science Reviews*, **24** (7-9): 869-896.

Gersonde R. & Zielinski U. 2000. The reconstruction of late Quaternary Antarctic sea-ice distribution—the use of diatoms as a proxy for sea-ice. *Palaeogeography, Palaeoclimatology, Palaeoecology*, **162**: 263-286.

Ghadi P., Nair A., Crosta X., Mohan R., Manoj M.C. & Meloth T. 2020. Antarctic sea-ice and palaeoproductivity variation over the last 156,000 years in the Indian sector of Southern Ocean. *Marine Micropaleontology*, **160**: 101894.

Gille S.T. 2014. Meridional displacement of the Antarctic Circumpolar Current. *Philos Trans A Math Phys Eng Sci*, **372** (2019): 20130273.

Gladstone R.M., Bigg G.R. & Nicholls K.W. 2001. Iceberg trajectory modeling and meltwater injection in the Southern Ocean. *Journal of Geophysical Research: Oceans*, **106** (C9): 19903-19915.

Goosse H. & Zunz V. 2014. Decadal trends in the Antarctic sea ice extent ultimately controlled by ice–ocean feedback. *The Cryosphere*, **8** (2): 453-470.

Gordon C., Cooper C., C.A. S., Banks H., Gregory J.M., Johns T.C., Mitchell J.F.B. & Wood R.A. 2000. The simulation of SST, sea ice extents and ocean heat transports in a version of the Hadley Centre coupled model without flux adjustments. *Climate Dynamics*, **16**: 147-168.

Govin A., Capron E., Tzedakis P.C., Verheyden S., Ghaleb B., Hillaire-Marcel C., St-Onge G., Stoner J.S., Bassinot F., Bazin L., Blunier T., Combourieu-Nebout N., El Ouahabi A., Genty D., Gersonde R., Jimenez-Amat P., Landais A., Martrat B., Masson-Delmotte V., Parrenin F., Seidenkrantz M.S., Veres D., Waelbroeck C. & Zahn R. 2015. Sequence of events from the onset to the demise of the Last Interglacial: Evaluating strengths and limitations of chronologies used in climatic archives. *Quaternary Science Reviews*, **129**: 1-36.

Govin A., Michel E., Labeyrie L., Waelbroeck C., Dewilde F. & Jansen E. 2009. Evidence for northward expansion of Antarctic Bottom Water mass in the Southern Ocean during the last glacial inception. *Paleoceanography*, **24** (1): PA1202.

Grobe H., Mackensen A., Hubberten H.-W., Spiess V. & Futterer D.K. 1990. Stable isotope record and Late Quaternary sedimentation rates at the Antarctic continental margin In: *Geological History of the Polar Oceans: Arctic versus Antarctic*, Bleil U. & Thiede H. Eds. Kluwer Academic Publishers (Dordrecht)**:** 539-572.

Guarino M.-V., Sime L.C., Schröeder D., Malmierca-Vallet I., Rosenblum E., Ringer M., Ridley J., Feltham D., Bitz C., Steig E.J., Wolff E., Stroeve J. & Sellar A. 2020. Sea-ice-free Arctic during the Last Interglacial supports fast future loss. *Nature Climate Change*, **10** (10): 928-932.

Guarino M.V., Sime L.C., Schroeder D. & Ridley J. 2022, *in review*. The first 250 years of the Heinrich 11 iceberg discharge: Last Interglacial HadGEM3-GC3.1 simulations for CMIP6-PMIP4. *Climate of the Past Discussions [preprint]*.

Guiot J. & de Vernal A. 2011. Is spatial autocorrelation introducing biases in the apparent accuracy of paleoclimatic reconstructions? *Quaternary Science Reviews*, **30** (15-16): 1965-1972.

Haid V. & Timmermann R. 2013. Simulated heat flux and sea ice production at coastal polynyas in the southwestern Weddell Sea. *Journal of Geophysical Research: Oceans*, **118** (5): 2640-2652.

Hall A. 2004. The Role of Surface Albedo Feedback in Climate. *Journal of Climate*, **17**: 1550-1568.

Hall A. & Visbeck M. 2002. Synchronous Variability in the Southern Hemisphere Atmosphere, Sea Ice, and Ocean Resulting from the Annular Mode. *Journal of Climate*, **15**: 3043-3057.

Hasle G.R. 1969. *An analysis of the phytoplankton of the Pacific Southern Ocean: abundance, composition, and distribution during the Brategg Expedition, 1947-1948.*

Hayes C.T., Martinez-Garcia A., Hasenfratz A.P., Jaccard S.L., Hodell D.A., Sigman D.M., Haug G.H. & Anderson R.F. 2014. A stagnation event in the deep South Atlantic during the last interglacial period. *Science*, **346** (6216): 1514-1517.

Hays J.D., Imbrie J. & Shackleton N.J. 1976. Variations in the Earth's Orbit: Pacemaker of the Ice Ages. *Science*, **194**: 1121-1132.

Hellmer H.H., Kauker F., Timmermann R., Determann J. & Rae J. 2012. Twenty-first-century warming of a large Antarctic ice-shelf cavity by a redirected coastal current. *Nature*, **485** (7397): 225-228.

Hersbach H., Bell B., Berrisford P., Biavati G., Horanyi A., Munoz Sabater J., Nicolas J., Peubey C., Radu R., Rozum I., Schepers D., Simmons A., Soci C., Dee D. & Thepaut J.-N. 2019. ERA5 monthly averaged data on single levels from 1980 to 2019. *Copernicus Climate Change Service (C3S) Climate Data Store (CDS)*.

Hill S.L., Phillips T. & Atkinson A. 2013. Potential Climate Change Effects on the Habitat of Antarctic Krill in the Weddell Quadrant of the Southern Ocean. *PLoS One*, **8** (8): e72246.

Hillenbrand C.D., Kuhn G. & Frederichs T. 2009. Record of a Mid-Pleistocene depositional anomaly in West Antarctic continental margin sediments: an indicator for ice-sheet collapse? *Quaternary Science Reviews*, **28** (13-14): 1147-1159.

Hillenbrand C.D., Smith J.A., Hodell D.A., Greaves M., Poole C.R., Kender S., Williams M., Andersen T.J., Jernas P.E., Elderfield H., Klages J.P., Roberts S.J., Gohl K., Larter R.D. & Kuhn G. 2017. West Antarctic Ice Sheet retreat driven by Holocene warm water incursions. *Nature*, **547** (7661): 43-48.

Hiscock M.R., Marra J., Smith W.O., Goericke R., Measures C., Vink S., Olson R.J., Sosik H.M. & Barber R.T. 2003. Primary productivity and its regulation in the Pacific Sector of the Southern Ocean. *Deep-Sea Research Part II: Topical Studies in Oceanography*, **50** (3-4): 533-558.

Hobbs W.R., Massom R., Stammerjohn S., Reid P., Williams G. & Meier W. 2016. A review of recent changes in Southern Ocean sea ice, their drivers and forcings. *Global and Planetary Change*, **143**: 228-250.

Hoffman J.S., Clark P.U., Parnell A.C. & Feng H. 2017. Regional and global sea-surface temperatures during the last interglaciation. *Science*, **355**: 276-279.

Holloway M.D., Sime L.C., Allen C.S., Hillenbrand C.-D., Bunch P., Wolff E. & Valdes P.J. 2017. The spatial structure of the 128 ka Antarctic sea ice minimum. *Geophysical Research Letters*, **44** (21): 11129-11139.

Holloway M.D., Sime L.C., Singarayer J.S., Tindall J.C., Bunch P. & Valdes P.J. 2016. Antarctic last interglacial isotope peak in response to sea ice retreat not ice-sheet collapse. *Nature Communications*, **7**: 12293.

Holloway M.D., Sime L.C., Singarayer J.S., Tindall J.C. & Valdes P.J. 2018. Simulating the 128-ka Antarctic Climate Response to Northern Hemisphere Ice Sheet Melting Using the Isotope-Enabled HadCM3. *Geophysical Research Letters*, **45** (21): 11921-11929.

Howe J.A., Harland R. & Pudsey C.J. 2002. Dinoflagellate cyst evidence for Quaternary palaeoceanographic change in the northern Scotia Sea, South Atlantic Ocean. *Marine Geology*, **191**: 55-69.

Hutchings L., van der Lingen C.D., Shannon L.J., Crawford R.J.M., Verheye H.M.S., Bartholomae C.H., van der Plas A.K., Louw D., Kreiner A., Ostrowski M., Fidel Q., Barlow R.G., Lamont T., Coetzee J., Shillington F., Veitch J., Currie J.C. & Monteiro P.M.S. 2009. The Benguela Current: An ecosystem of four components. *Progress in Oceanography*, **83** (1-4): 15-32.

Hutson W.H. 1980. The Agulhas current during the late Pleistocene: analysis of modern faunal analogs. *Science*, **207**: 64-66.

Huybers P. & Denton G. 2008. Antarctic temperature at orbital timescales controlled by local summer duration. *Nature Geoscience*, **1** (11): 787-792.

Imbrie J., Hays J.D., Martinson D.G., McIntyre A., Mix A.C., Morley J.J., Pisias N.G., Prell W.L. & Shackleton N.J. 1984. The orbital theory of Pleistocene climate: Support from a revised chronology of the marine $\delta^{18}O$ record. In: *Milankovitch and Climate*, Berger A. Ed. **1:** 269-305.

Imbrie J. & Kipp N.G. 1971. A new micropaleontological method for quantitative paleoclimatology: application to a late Pleistocene Caribbean core. In: *The Late Cenozoic Glacial Ages*, Turekian K.K. Ed., Yale University Press, London**:** 71-147.

IPCC. 2014. Climate Change 2014: Synthesis Report. Contribution of Working Groups I, II and III to the Fifth Assessment Report of the Intergovernmental Panel on Climate Change. IPCC, Geneva, Switzerland, 151.

IPCC. 2019. Summary for Policymakers. In: *IPCC Special Report on the Ocean and Cryosphere in a Changing Climate*, Portner H.O., Roberts D.C., Masson-Delmotte V. et al. Eds.**:** 1-36.

Jenkins A., Dutrieux P., Jacobs S., Steig E., Gudmundsson H., Smith J. & Heywood K. 2016. Decadal Ocean Forcing and Antarctic Ice Sheet Response: Lessons from the Amundsen Sea. *Oceanography*, **29** (4): 106-117.

Jenouvrier S., Barbraud C. & Weimerskirch H. 2005. Long-term contrasted responses to climate of two Antarctic seabird species. *Ecology*, **86** (11): 2889-2903.

Kahru M., Lee Z., Mitchell B.G. & Nevison C.D. 2016. Effects of sea ice cover on satellite-detected primary production in the Arctic Ocean. *Biol Lett*, **12** (11): 20160223.

Kanfoush S.L., Hodell D.A., Charles C.D., Janecek T.R. & Rack F.R. 2002. Comparison of ice-rafted debris and physical properties in ODP Site 1094 (South Atlantic) with the Vostok ice core over the last four climatic cycles. *Palaeogeography, Palaeoclimatology, Palaeoecology*, **182**: 329-349.

Kang S.-H. & Fryxell G.A. 1992. *Fragilariopsis cylindrus* (Grunow) Krieger: The most abundant diatom in water column assemblages of Antarctic marginal ice-edge zones *Polar Biology*, **12** (6-7): 609-627.

Kang S.-H. & Fryxell G.A. 1993. Phytoplankton in the Weddell Sea, Antarctica: composition, abundance and distribution in water-column assemblages of the marginal ice-edge zone during austral autumn. *Marine Biology*, **116**: 335-348.

Kang S.-H., Fryxell G.A. & Roelke D.L. 1993. *Fragilariopsis cylindrus* compared with other species of the diatom family Bacillariaceae in Antarctic marginal ice-edge zones. *Nova Hedwigia*, **106**: 335-352.

Kemp A.E.S., Grigorov I., Pearce R.B. & Naveira Garabato A.C. 2010. Migration of the Antarctic Polar Front through the mid-Pleistocene transition: evidence and climatic implications. *Quaternary Science Reviews*, **29** (17-18): 1993-2009.

Kim S., Lee J.I., McKay R.M., Yoo K.-C., Bak Y.-S., Lee M.K., Roh Y.H., Yoon H.I., Moon H.S. & Hyun C.-U. 2020. Late pleistocene paleoceanographic changes in the Ross Sea – Glacial-interglacial variations in paleoproductivity, nutrient utilization, and deep-water formation. *Quaternary Science Reviews*, **239**: 106356.

Kim Y.S. & Orsi A.H. 2014. On the Variability of Antarctic Circumpolar Current Fronts Inferred from 1992–2011 Altimetry*. *Journal of Physical Oceanography*, **44** (12): 3054-3071.

King J. 2014. A resolution of the Antarctic paradox. *Nature*, **505**: 491-492.

Knox G.A. 2006. *Biology of the Southern Ocean*. Marine Biology Series: CRC Press.

Konfirst M.A., Scherer R.P., Hillenbrand C.D. & Kuhn G. 2012. A marine diatom record from the Amundsen Sea - Insights into oceanographic and climatic response to the Mid-Pleistocene Transition in the West Antarctic sector of the Southern Ocean. *Marine Micropaleontology*, **92-93**: 40-51.

Kopp R.E., Simons F.J., Mitrovica J.X., Maloof A.C. & Oppenheimer M. 2009. Probabilistic assessment of sea level during the last interglacial stage. *Nature*, **462** (7275): 863-867.

Kopp R.E., Simons F.J., Mitrovica J.X., Maloof A.C. & Oppenheimer M. 2013. A probabilistic assessment of sea level variations within the last interglacial stage. *Geophysical Journal International*, **193** (2): 711-716.

Labeyrie L., Labracherie M., Gorfti N., Pichon J.J., Vautravers M., Arnold M., Duplessy J.-C., Paterne M., Michel E., Duprat J., Caralp M. & Turon J.-L. 1996. Hydrographic changes of the Southern Ocean (southeast Indian Sector) Over the last 230 kyr. *Paleoceanography*, **11** (1): 57-76.

Lago V. & England M.H. 2019. Projected Slowdown of Antarctic Bottom Water Formation in Response to Amplified Meltwater Contributions. *Journal of Climate*, **32** (19): 6319-6335.

Leventer A. 1991. Sediment trap diatom assemblages from the northern Antarctic Peninsula region. *Deep-Sea Research*, **38** (89): 1127-1143.

Leventer A. 1992. Modern distribution of diatoms in sediments from the George V Coast, Antarctica. *Marine Micropaleontology*, **19**: 315-332.

Leventer A. 1998. The fate of Antarctic "sea ice diatoms" and their use as paleoenvironmental indicators. In: *Antarctic Sea-ice, Biological Processes, Interactions and Variability*, Lizotte M.P. & Arrigo K.R. Eds., Antarctic Research Series, American Geophysical Union, Washington D.C. **73:** 121-137.

Leventer A. & Dunbar R.B. 1988. Recent Diatom Record of McMurdo Sound, Antarctica: Implications for History of Sea Ice Extent. *Paleoceanography*, **3** (3): 259-274.

Lisiecki L.E. & Raymo M.E. 2005. A Pliocene-Pleistocene stack of 57 globally distributed benthic δ18O records. *Paleoceanography*, **20** (1): PA1003.

Liu J. & Curry J.A. 2010. Accelerated warming of the Southern Ocean and its impacts on the hydrological cycle and sea ice. *Proc Natl Acad Sci USA*, **107** (34): 14987-14992.

Liu Y., Moore J.C., Cheng X., Gladstone R.M., Bassis J.N., Liu H., Wen J. & Hui F. 2015. Ocean-driven thinning enhances iceberg calving and retreat of Antarctic ice shelves. *Proc Natl Acad Sci USA*, **112** (11): 3263-3268.

Locarnini R.A., Mishonov A.V., Antonov J.I., Boyer T.P., Garcia H.E., Baranova O.K., Zweng M.M., Paver C.R., Reagan J.R., Johnson D.R., Hamilton M. & Seidov D. 2013. *World Ocean atlas 2013, volume 1: Temperature*. NOAA Atlas NESDIS 81.

Madec G., Bourdalle-Badie R., Chanut J., Clementi E., Coward A., Ethe C., Iovino D., Lea D., Levy C., Lovato T., Martin N., Masson S., Mocavero S., Rousset C., Storkey D., Vancoppenolle M., Mueller S., Nurser G., Bell M. & Samson G. 2019. *NEMO ocean engine*: Notes Du Pole De Modelisation De L'institut Pierre-simon Laplace (IPSL).

Maheshwari M., Singh R.K., Oza S.R. & Kumar R. 2013. An Investigation of the Southern Ocean Surface Temperature Variability Using Long-Term Optimum Interpolation SST Data. *ISRN Oceanography*, **2013**: 1-9.

Marino G., Rohling E.J., Rodriguez-Sanz L., Grant K.M., Heslop D., Roberts A.P., Stanford J.D. & Yu J. 2015. Bipolar seesaw control on last interglacial sea level. *Nature*, **522** (7555): 197-201.

Martinson D.G., Pisias N.G., Hays J.D., Imbrie J., Moore T.C. & Shackleton N.J. 1987. Age Dating and the Orbital Theory of the Ice Ages: Development of a High-Resolution 0 to 300,000-Year Chronostratigraphy. *Quaternary Research*, **27**: 1-29.

Marzocchi A. & Jansen M.F. 2019. Global cooling linked to increased glacial carbon storage via changes in Antarctic sea ice. *Nature Geoscience*, **12**: 1001-1005.

Massom R.A., Scambos T.A., Bennetts L.G., Reid P., Squire V.A. & Stammerjohn S.E. 2018. Antarctic ice shelf disintegration triggered by sea ice loss and ocean swell. *Nature*, **558** (7710): 383-389.

Massom R.A. & Stammerjohn S.E. 2010. Antarctic sea ice change and variability – Physical and ecological implications. *Polar Science*, **4** (2): 149-186.

Masson-Delmotte V., Buiron D., Ekaykin A., Frezzotti M., Gallée H., Jouzel J., Krinner G., Landais A., Motoyama H., Oerter H., Pol K., Pollard D., Ritz C., Schlosser E., Sime L.C., Sodemann H., Stenni B., Uemura R. & Vimeux F. 2011. A comparison of the present and last interglacial periods in six Antarctic ice cores. *Climate of the Past*, **7** (2): 397-423.

Mazloff M.R. 2012. On the Sensitivity of the Drake Passage Transport to Air–Sea Momentum Flux. *Journal of Climate*, **25** (7): 2279-2290.

McCartney M.S. & Donohue K.A. 2007. A deep cyclonic gyre in the Australian - Antarctic Basin. *Progress in Oceanography*, **75**: 675-750.

Meijers A.J.S., Shuckburgh E., Bruneau N., Sallee J.B., Bracegirdle T.J. & Wang Z. 2012. Representation of the Antarctic Circumpolar Current in the CMIP5 climate models and future changes under warming scenarios. *Journal of Geophysical Research: Oceans*, **117**: C12008.

Meinen C.S., Luther D.S., Watts D.R., Chave A.D. & Tracey K.L. 2003. Mean stream coordinates structure of the Subantarctic Front: Temperature, salinity, and absolute velocity. *Journal of Geophysical Research*, **108** (C8): 3263.

Menary M.B., Kuhlbrodt T., Ridley J., Andrews M.B., Dimdore-Miles O.B., Deshayes J., Eade R., Gray L., Ineson S., Mignot J., Roberts C.D., Robson J., Wood R.A. & Xavier P. 2018. Preindustrial Control Simulations With HadGEM3-GC3.1 for CMIP6. *Journal of Advances in Modeling Earth Systems*, **10**: 3049-3075.

Menviel L., Timmermann A., Timm O.E. & Mouchet A. 2010. Climate and biogeochemical response to a rapid melting of the West Antarctic Ice Sheet during interglacials and implications for future climate. *Paleoceanography*, **25** (4): PA4231.

Merino N., Jourdain N.C., Le Sommer J., Goosse H., Mathiot P. & Durand G. 2018. Impact of increasing antarctic glacial freshwater release on regional sea-ice cover in the Southern Ocean. *Ocean Modelling*, **121**: 76-89.

Merino N., Le Sommer J., Durand G., Jourdain N.C., Madec G., Mathiot P. & Tournadre J. 2016. Antarctic icebergs melt over the Southern Ocean: Climatology and impact on sea ice. *Ocean Modelling*, **104**: 99-110.

Miklasz K.A. & Denny M.W. 2010. Diatom sinkings speeds: Improved predictions and insight from a modified Stokes' law. *Limnology and Oceanography*, **55** (6): 2513-2525.

Milillo P., Rignot E., Rizzoli P., Scheuchl B., Mouginot J., Bueso-Bello J. & Prats-Iraola P. 2019. Heterogeneous retreat and ice melt of Thwaites Glacier, West Antarctica. *Science Advances*, **5** (1): eaau3433.

Monroy P., Hernández-García E., Rossi V. & López C. 2017. Modeling the dynamical sinking of biogenic particles in oceanic flow. *Nonlinear Processes in Geophysics*, **24** (2): 293-305.

Montes-Hugo M., Doney S.C., Ducklow H.W., Fraser W., Martinson D., Stammerjohn S.E. & Schofield O. 2009. Recent changes in phytoplankton communities associated with rapid regional climate change along the western Antarctic Peninsula. *Science*, **323** (5920): 1470-1473.

Moore J.K., Abbott M.R. & Richman J.G. 1999. Location and dynamics of the Antarctic Polar Front from satellite sea surface temperature data. *Journal of Geophysical Research*, **104** (C2): 3059-3073.

Morlighem M., Rignot E., Binder T., Blankenship D., Drews R., Eagles G., Eisen O., Ferraccioli F., Forsberg R., Fretwell P., Goel V., Greenbaum J.S., Gudmundsson H., Guo J., Helm V., Hofstede C., Howat I., Humbert A., Jokat W., Karlsson N.B., Lee W.S., Matsuoka K., Millan R., Mouginot J., Paden J., Pattyn F., Roberts J., Rosier S., Ruppel A., Seroussi H. et al. 2020. Deep glacial troughs and stabilizing ridges unveiled beneath the margins of the Antarctic ice sheet. *Nature Geoscience*, **13** (2): 132-137.

Mulitza S., Arz H.W., Kemle-von Mucke S., Moos C., Niebler H.-S., Patzold J. & Segl M. 1999. Foraminifera isotopes of sediment core PS1768-8. *PANGAEA*.

Mulvaney R., Abram N.J., Hindmarsh R.C., Arrowsmith C., Fleet L., Triest J., Sime L.C., Alemany O. & Foord S. 2012. Recent Antarctic Peninsula warming relative to Holocene climate and ice-shelf history. *Nature*, **489** (7414): 141-144.

Nair A., Mohan R., Crosta X., Manoj M.C., Thamban M. & Marieu V. 2019. Southern Ocean sea ice and frontal changes during the Late Quaternary and their linkages to Asian summer monsoon. *Quaternary Science Reviews*, **213**: 93-104.

Neil H.L., Carter L. & Morris M.Y. 2004. Thermal isolation of Campbell Plateau, New Zealand, by the Antarctic Circumpolar Current over the past 130 kyr. *Paleoceanography*, **19** (4): PA4008.

Nelson C.S., Cooke P.J., Hendy C.H. & Cuthbertson A.M. 1993. Oceanographic and climatic changes over the past 160,000 years at Deep Sea Drilling Project Site 594 off Southeastern New Zealand, Southwest Pacific Ocean. *Paleoceanography*, **8** (4): 435-458.

Neori A. & Holm-Hansen O. 1982. Effect of temperature on rate of photosynthesis in Antarctic phytoplankton. *Polar Biology*, **1**: 33-38.

Nghiem S.V., Rigor I.G., Clemente-Colón P., Neumann G. & Li P.P. 2016. Geophysical constraints on the Antarctic sea ice cover. *Remote Sensing of Environment*, **181**: 281-292.

Niebler H.-S. 1995. Reconstruction of paleo-environmental parameters using stable isotopes and faunal assemblages of planktonic foraminifera in the South Atlantic Ocean. *Reports on Polar Research*, **167**: 1-198.

Nürnberg C.C., Bohrmann G., Schlüter M. & Frank M. 1997. Barium accumulation in the Atlantic sector of the Southern Ocean: Results From 190,000-year records. *Paleoceanography*, **12** (4): 594-603.

Orsi A.H., Johnson G.C. & Bullister J.L. 1999. Circulation, mixing, and production of Antarctic Bottom Water. *Progress in Oceanography*, **43**: 55-109.

Orsi A.H., Smethie Jr. W.M. & Bullister J.L. 2002. On the total input of Antarctic waters to the deep ocean: A preliminary estimate from chlorofluorocarbon measurements. *Journal of Geophysical Research*, **107** (C8): 3122.

Orsi A.H., Whitworth III T. & Nowlin Jr W.D. 1995. On the meridional extent and fronts of the Antarctic Circumpolar Current. *Deep-Sea Research I*, **42** (5): 641-673.

Otto-Bliesner B.L., Braconnot P., Harrison S.P., Lunt D.J., Abe-Ouchi A., Albani S., Bartlein P.J., Capron E., Carlson A.E., Dutton A., Fischer H., Goelzer H., Govin A., Haywood A., Joos F., LeGrande A.N., Lipscomb W.H., Lohmann G., Mahowald N., Nehrbass-Ahles C., Pausata F.S.R., Peterschmitt J.-Y., Phipps S.J., Renssen H. & Zhang Q. 2017. The PMIP4 contribution to CMIP6 – Part 2: Two interglacials, scientific objective and experimental design for Holocene and Last Interglacial simulations. *Geoscientific Model Development*, **10** (11): 3979-4003.

Otto-Bliesner B.L., Brady E.C., Zhao A., Brierley C., Axford Y., Capron E., Govin A., Hoffman J., Isaacs E., Kageyama M., Scussolini P., Tzedakis P.C., Williams C., Wolff E., Abe-Ouchi A., Braconnot P., Ramos Buarque S., Cao J., de Vernal A., Guarino M.V., Guo C., LeGrande A.N., Lohmann G., Meissner K., Menviel L., Nisancioglu K., O'Ishi R., Salas Y Melia D., Shi X., Sicard M. et al. 2021. Large-scale features of Last Interglacial climate: results from evaluating the *lig127k* simulations for the Coupled Model Intercomparison Project (CMIP6)-Paleoclimate Modeling Intercomparison Project (PMIP4). *Climate of the Past*, **17**: 63-94.

Otto-Bliesner B.L., Rosenbloom N., Stone E.J., McKay N.P., Lunt D.J., Brady E.C. & Overpeck J.T. 2013. How warm was the last interglacial? New model-data comparisons. *Philos Trans A Math Phys Eng Sci*, **371** (2001): 20130097.

Pahnke K., Zahn R., Elderfield H. & Schulz M. 2003. 340,000-Year Centennial-Scale Marine Record of Southern Hemisphere Climatic Oscillation. *Science*, **301**: 948-952.

Paillard D., Labeyrie L. & Yiou P. 1996. Macintosh program performs time-series analysis. *Eos*, **77**: 379.

Parkinson C.L. 2019. A 40-y record reveals gradual Antarctic sea ice increases followed by decreases at rates far exceeding the rates seen in the Arctic. *Proc Natl Acad Sci USA*, **116** (29): 14414-14423.

Parrenin F., Barnola J.-M., Beer J., Blunier T., Castellano E., Chappellaz J., Dreyfus G., Fischer H., Fujita S., Jouzel J., Kawamura K., Lemieux-Dudon B., Loulergue L., Masson-Delmotte V., Narcisi B., Petit J.-R., Raisbeck G., Raynaud D., Ruth U., Schwander J., Severi M., Spahni R., Steffensen J.P., Svensson A., Udisti R., Waelbroeck C. & Wolff E. 2007. The EDC3 chronology for the EPICA Dome C ice core. *Climate of the Past*, **3**: 485-497.

Parrenin F., Masson-Delmotte V., Kohler P., Raynaud D., Paillard D., Schwander J., Barbante C., Landais A., Wegner A. & Jouzel J. 2013a. Antarctic Temperature Stack (ATS) from five different ice cores (EDC, Vostok, Dome Fuji, TALDICE, and EDML). *PANGAEA*.

Parrenin F., Masson-Delmotte V., Kohler P., Raynaud D., Paillard D., Schwander J., Barbante C., Landais A., Wegner A. & Jouzel J. 2013b. Synchronisation of the LR04 stack with EDC isotopic variations on the EDC3 age scale. *PANGAEA*.

Pattyn F. 2018. The paradigm shift in Antarctic ice sheet modelling. *Nat Commun*, **9** (1): 2728.

Pedro J.P., Jochum M., Buizert C., He F., Barker S. & Rasmussen S.O. 2018. Beyond the bipolar seesaw; Toward a process understanding of interhemispheric coupling. *Quaternary Science Reviews*, **192**: 27-46.

Pelejero C., Calvo E., Barrows T.T., Logan G.A. & De Deckker P. 2006. South Tasman Sea alkenone palaeothermometry over the last four glacial/interglacial cycles. *Marine Geology*, **230** (1-2): 73-86.

Pichon J.J., Labeyrie L.D., Bareille G., Labracherie M., Duprat J. & Jouzel J. 1992. Surface Water Temperature Changes in the High Latitudes of the Southern Hemisphere over the Last Glacial-Interglacial Cycle. *Paleoceanography*, **7** (3): 289-318.

Pollard D. & DeConto R.M. 2009. Modelling West Antarctic ice sheet growth and collapse through the past five million years. *Nature*, **458** (7236): 329-332.

Presti M., Barbara L., Denis D., Schmidt S., De Santis L. & Crosta X. 2011. Sediment delivery and depositional patterns off Adélie Land (East Antarctica) in relation to late Quaternary climatic cycles. *Marine Geology*, **284** (1-4): 96-113.

Pugh R.S., McCave I.N., Hillenbrand C.D. & Kuhn G. 2009. Circum-Antarctic age modelling of Quaternary marine cores under the Antarctic Circumpolar Current: Ice-core dust–magnetic correlation. *Earth and Planetary Science Letters*, **284** (1-2): 113-123.

Purich A., England M.H., Cai W., Chikamoto Y., Timmermann A., Fyfe J.C., Frankcombe L., Meehl G.A. & Arblaster J.M. 2016. Tropical Pacific SST Drivers of Recent Antarctic Sea Ice Trends. *Journal of Climate*, **29** (24): 8931-8948.

Rahmstorf S. 2002. Ocean circulation and climate during the past 120,000 years. *Nature*, **419**: 207-214.

Railsback L.B., Gibbard P.L., Head M.J., Voarintsoa N.R.G. & Toucanne S. 2015. An optimized scheme of lettered marine isotope substages for the last 1.0 million years, and the climatostratigraphic nature of isotope stages and substages. *Quaternary Science Reviews*, **111**: 94-106.

Rayner N.A., Parker D.E., Horton E.B., Folland C.K., Alexander L.V., Rowell D.P., Kent E.C. & Kaplan A. 2003. Global analyses of sea surface temperature, sea ice, and night marine air temperature since the late nineteenth century. *Journal of Geophysical Research*, **108** (D14): 4407.

Ridley J.K., Blockley E.W., Keen A.B., Rae J.G.L., West A.E. & Schroeder D. 2018. The sea ice model component of HadGEM3-GC3.1. *Geoscientific Model Development*, **11** (2): 713-723.

Rignot E., Mouginot J., Scheuchl B., van den Broeke M., van Wessem M.J. & Morlighem M. 2019. Four decades of Antarctic Ice Sheet mass balance from 1979-2017. *Proc Natl Acad Sci USA*, **116** (4): 1095-1103.

Rintoul S.R. 2018. The global influence of localized dynamics in the Southern Ocean. *Nature*, **558** (7709): 209-218.

Rintoul S.R., Hughes C. & Olbers D. 2001. The Antarctic Circumpolar Current System. In: *Ocean circulation and climate; observing and modelling the global ocean*, Siedler G., Church J. & Gould J. Eds. International Geophysics Series, Academic Press. **77:** 271-302.

Romero O.E., Armand L.K., Crosta X. & Pichon J.J. 2005. The biogeography of major diatom taxa in Southern Ocean surface sediments: 3. Tropical/Subtropical species. *Palaeogeography, Palaeoclimatology, Palaeoecology*, **223** (1-2): 49-65.

Rosenblum E. & Eisenman I. 2017. Sea Ice Trends in Climate Models Only Accurate in Runs with Biased Global Warming. *Journal of Climate*, **30** (16): 6265-6278.

Russell J.L., Dixon K.W., Gnanadesikan A., Stouffer R.J. & Toggweiler J.R. 2006. The Southern Hemisphere Westerlies in a Warming World: Propping Open the Door to the Deep Ocean. *Journal of Climate*, **19**: 6382-6390.

Rysgaard S., Bendtsen J., Delille B., Dieckmann G.S., Glud R.N., Kennedy H., Mortensen J., Papadimitriou S., Thomas D.N. & Tison J.-L. 2011. Sea ice contribution to the air–sea CO_2 exchange in the Arctic and Southern Oceans. *Tellus B: Chemical and Physical Meteorology*, **63** (5): 823-830.

Santoso A., England M.H. & Hirst A. 2006. Circumpolar Deep Water Circulation and Variability in a Coupled Climate Model. *Journal of Physical Oceanography*, **36**: 1523-1552.

Saunders K.M., Kamenik C., Hodgson D.A., Hunziker S., Siffert L., Fischer D., Fujak M., Gibson J.A.E. & Grosjean M. 2012. Late Holocene changes in precipitation in northwest Tasmania and their potential links to shifts in the Southern Hemisphere westerly winds. *Global and Planetary Change*, **92-93**: 82-91.

Scambos T.A., Bell R.E., Alley R.B., Anandakrishnan S., Bromwich D.H., Brunt K., Christianson K., Creyts T., Das S.B., DeConto R., Dutrieux P., Fricker H.A., Holland D., MacGregor J., Medley B., Nicolas J.P., Pollard D., Siegfried M.R., Smith A.M., Steig E.J., Trusel L.D., Vaughan D.G. & Yager P.L. 2017. How much, how fast?: A science review and outlook for research on the instability of Antarctica's Thwaites Glacier in the 21st century. *Global and Planetary Change*, **153**: 16-34.

Scherer R.P. 1994. A new method for the determination of absolute abundance of diatoms and other silt-sized sedimentary particles. *Journal of Paleolimnology*, **12** (2): 171-179.

Schmidtko S., Heywood K.J., Thompson A.F. & Aoki S. 2014. Multidecadal warming of Antarctic waters. *Science*, **346** (6214): 1227-1231.

Schneider Mor A., Yam R., Bianchi C., Kunz-Pirrung M., Gersonde R. & Shemesh A. 2012. Variable sequence of events during the past seven terminations in two deep-sea cores from the Southern Ocean. *Quaternary Research*, **77** (02): 317-325.

Schoof C. 2007. Ice sheet grounding line dynamics: Steady states, stability, and hysteresis. *Journal of Geophysical Research*, **112**: F03S28.

Schweitzer P.N. 1995. Monthly average polar sea-ice concentration 1978 through 1991. *U.S. Geological Survey, Reston, Virginia*.

Shackleton N.J. & Opdyke N.D. 1973. Oxygen Isotope and Palaeomagnetic Stratigraphy of Equatorial Pacific Core V28-238: Oxygen Isotope Temperatures and Ice Volumes on a 10^5 Year and 10^6 Year Scale. *Quaternary Research*, **3** (1): 39-55.

Shemesh A., Hodell D., Crosta X., Kanfoush S., Charles C. & Guilderson T. 2002. Sequence of events during the last deglaciation in Southern Ocean sediments and Antarctic ice cores. *Paleoceanography*, **17** (4): 8-1-8-7.

Shepherd A., Ivins E., Rignot E., Smith B., van den Broeke M., Velicogna I., Whitehouse P., Briggs K., Joughin I., Krinner G., Nowicki S., Payne T., Scambos T., Schlegel N., A G., Agosta C., Ahlstrom A., Babonis G., Barletta V., Blazquez A., Bonin J., Csatho B., Cullather R., Felikson D., Fettweis X., Forsberg R., Gallée H., Gardner A., Gilbert L., Groh A. et al. 2018. Mass balance of the Antarctic Ice Sheet from 1992 to 2017. *Nature*, **558** (7709): 219-222.

Siegel V. & Watkins J.L. 2016. Distribution, Biomass and Demography of Antarctic Krill, *Euphausia superba*. In: *Biology and Ecology of Antarctic krill*, Siegel V. Ed. Advances in Polar Ecology**:** 21-100.

Sikes E.L., Howard W.R., Neil H.A. & K. V.J. 2002. Glacial-interglacial sea surface temperature changes across the subtropical front east of New Zealand based on alkenone unsaturation ratios and foraminiferal assemblages. *Paleoceanography*, **17** (2): 1-13.

Silva T.A.M., Bigg G.R. & Nicholls K.W. 2006. Contribution of giant icebergs to the Southern Ocean freshwater flux. *Journal of Geophysical Research*, **111**: C03004.

Sime L.C., Carlson A.E. & Holloway M.D. 2019. On recovering Last Interglacial changes in the Antarctic ice sheet. *Past Global Changes Magazine*, **27** (1): 14-15.

Sime L.C., Wolff E.W., Oliver K.I. & Tindall J.C. 2009. Evidence for warmer interglacials in East Antarctic ice cores. *Nature*, **462** (7271): 342-345.

Simpson G. 2007. Analogue Methods in Palaeoecology: Using the analogue Package. *Journal of Statistical Software*, **22**: i02.

Sloyan B.M. & Rintoul S.R. 2001. Circulation, Renewal, and Modification of Antarctic Mode and Intermediate Water. *Journal of Physical Oceanography*, **31**: 1005-1030.

Sokolov S. & Rintoul S.R. 2009. Circumpolar structure and distribution of the Antarctic Circumpolar Current fronts: 1. Mean circumpolar paths. *Journal of Geophysical Research*, **114**: C11018.

Spence P., Holmes R.M., Hogg A.M., Griffies S.M., Stewart K.D. & England M.H. 2017. Localized rapid warming of West Antarctic subsurface waters by remote winds. *Nature Climate Change*, **7** (8): 595-603.

Stammerjohn S.E., Martinson D.G., Smith R.C. & Iannuzzi R.A. 2008a. Sea ice in the western Antarctic Peninsula region: Spatio-temporal variability from ecological and climate change perspectives. *Deep-Sea Research Part II: Topical Studies in Oceanography*, **55** (18-19): 2041-2058.

Stammerjohn S.E., Martinson D.G., Smith R.C., Yuan X. & Rind D. 2008b. Trends in Antarctic annual sea ice retreat and advance and their relation to El Niño–Southern Oscillation and Southern Annular Mode variability. *Journal of Geophysical Research*, **113** (C3): C03S90.

Stocker T.F. & Johnsen S.J. 2003. A minimum thermodynamic model for the bipolar seesaw. *Paleoceanography*, **18** (4): 1087.

Stone E.J., Capron E., Lunt D.J., Payne A.J., Singarayer J.S., Valdes P.J. & Wolff E.W. 2016. Impact of meltwater on high-latitude early Last Interglacial climate. *Climate of the Past*, **12** (9): 1919-1932.

Tamsitt V., Drake H.F., Morrison A.K., Talley L.D., Dufour C.O., Gray A.R., Griffies S.M., Mazloff M.R., Sarmiento J.L., Wang J. & Weijer W. 2017. Spiraling pathways of global deep waters to the surface of the Southern Ocean. *Nat Commun*, **8** (1): 172.

Taylor M.H., Losch M. & Bracher A. 2013. On the drivers of phytoplankton blooms in the Antarctic marginal ice zone: A modeling approach. *Journal of Geophysical Research: Oceans*, **118** (1): 63-75.

Thomas E.R., Allen C.S., Etourneau J., King A.C.F., Severi M., Winton V.H.L., Mueller J., Crosta X. & Peck V.L. 2019. Antarctic Sea Ice Proxies from Marine and Ice Core Archives Suitable for Reconstructing Sea Ice over the Past 2000 Years. *Geosciences*, **9** (12): 506.

Tierney J.E., Zhu J., King J., Malevich S.B., Hakim G.J. & Poulsen C.J. 2020. Glacial cooling and climate sensitivity revisited. *Nature*, **584** (7822): 569-573.

Tim N., Zorita E., Schwarzkopf F.U., Rühs S., Emeis K.C. & Biastoch A. 2018. The impact of Agulhas leakage on the central water masses in the Benguela upwelling system from a high-resolution ocean simulation. *Journal of Geophysical Research: Oceans*, **123**: 9416-9428.

Tournadre J., Bouhier N., Girard-Ardhuin F. & Rémy F. 2016. Antarctic icebergs distributions 1992–2014. *Journal of Geophysical Research: Oceans*, **121** (1): 327-349.

Trathan P.N., Brandon M.A., Murphy E.J. & Thorpe S.E. 2000. Transport and structure within the Antarctic Circumpolar Current to the north of South Georgia. *Geophysical Research Letters*, **27** (12): 1727-1730.

Turney C.S.M., Fogwill C.J., Golledge N.R., McKay N.P., van Sebille E., Jones R.T., Etheridge D., Rubino M., Thornton D.P., Davies S.M., Ramsey C.B., Thomas Z.A., Bird M.I., Munksgaard N.C., Kohno M., Woodward J., Winter K., Weyrich L.S., Rootes C.M., Millman H., Albert P.G., Rivera A., van Ommen T., Curran M., Moy A., Rahmstorf S., Kawamura K., Hillenbrand C.D., Weber M.E., Manning C.J. et al. 2020a. Early Last Interglacial ocean warming drove substantial ice mass loss from Antarctica. *Proc Natl Acad Sci USA*, **117** (8): 3996-4006.

Turney C.S.M., Jones R., McKay N.P., van Sebille E., Thomas Z.A., Hillenbrand C.-D. & Fogwill C.J. 2020b. A global mean sea-surface temperature dataset for the Last Interglacial (129-116 kyr) and contribution of thermal expansion to sea-level change. *Earth System Science Data Discussions*, **12** (4): 3341-3356.

Turney C.S.M. & Jones R.T. 2010. Does the Agulhas Current amplify global temperatures during super-interglacials? *Journal of Quaternary Science*, **25** (6): 839-843.

van Sebille E., Griffies S.M., Abernathey R., Adams T.P., Berloff P., Biastoch A., Blanke B., Chassignet E.P., Cheng Y., Cotter C.J., Deleersnijder E., Döös K., Drake H.F., Drijfhout S., Gary S.F., Heemink A.W., Kjellsson J., Koszalka I.M., Lange M., Lique C., MacGilchrist G.A., Marsh R., Mayorga Adame C.G., McAdam R., Nencioli F., Paris C.B., Piggott M.D., Polton J.A., Rühs S., Shah S.H.A.M. et al. 2018. Lagrangian ocean analysis: Fundamentals and practices. *Ocean Modelling*, **121**: 49-75.

Vaughan D.G., Comiso J.C., Allison I., Carrasco J., Kaser G., Kwok R., Mote P., Murray T., Paul F., Ren J., Rignot E., Solomina O., Steffen K. & Zhang T. 2013. Observations: Cryosphere. In: *Climate Change 2013: The Physical Science Basis, Contribution of Working Group I to the Fifth Assessment Report of the Intergovernmental Panel on Climate Change.*, Stocker T.F., Qin D., Plattner G.-K. et al. Eds. Cambridge University Press, Cambridge, United Kingdom and New York, NY, USA.**:** 317-382.

Vernet M., Geibert W., Hoppema M., Brown P.J., Haas C., Hellmer H.H., Jokat W., Jullion L., Mazloff M., Bakker D.C.E., Brearley J.A., Croot P., Hattermann T., Hauck J., Hillenbrand C.D., Hoppe C.J.M., Huhn O., Koch B.P., Lechtenfeld O.J., Meredith M.P., Naveira Garabato A.C., Nöthig E.M., Peeken I., Rutgers van der Loeff M.M., Schmidtko S., Schröder M., Strass V.H., Torres-Valdés S. & Verdy A. 2019. The Weddell Gyre, Southern Ocean: Present Knowledge and Future Challenges. *Reviews of Geophysics*, **57** (3): 623-708.

von Quillfeldt C. 2004. The diatom *Fragilariopsis cylindrus* and its potential as an indicator species for cold water rather than for sea ice. *Vie et Milieu / Life & Environment*, **54** (2-3): 137-143.

Waelbroeck C., Paul A., Kucera M., Rosell-Melé A., Weinelt M., Schneider R., Mix A.C., Abelmann A., Armand L., Bard E., Barker S., Barrows T.T., Benway H., Cacho I., Chen M.T., Cortijo E., Crosta X., de Vernal A., Dokken T., Duprat J., Elderfield H., Eynaud F., Gersonde R., Hayes A., Henry M., Hillaire-Marcel C., Huang C.C., Jansen E., Juggins S., Kallel N. et al. 2009. Constraints on the magnitude and patterns of ocean cooling at the Last Glacial Maximum. *Nature Geoscience*, **2** (2): 127-132.

Wahlin A.K., Graham A.G.C., Hogan K.A., Queste B.Y., Boehme L., Larter R.D., Pettit E.C., Wellner J. & Heywood K.J. 2021. Pathways and modification of warm water flowing beneath Thwaites Ice Shelf, West Antarctica. *Science Advances*, **7**: eabd7254.

Walter H.J., Hegner E., Diekmann B., Kuhn G. & Rutgers van der Loeff M.M. 2000. Provenance and transport of terrigenous sediment in the South Atlantic Ocean and their relations to glacial and interglacial cycles: Nd and Sr isotopic evidence. *Geochimica et Cosmochimica Acta*, **64** (22): 3813-3827.

Walter J.I., Box J.E., Tulaczyk S., Brodsky E.E., Howat I.M., Ahn Y. & Brown A. 2012. Oceanic mechanical forcing of a marine-terminating Greenland glacier. *Annals of Glaciology*, **53** (60): 181-192.

Walters D., Boutle I., Brooks M., Melvin T., Stratton R., Vosper S., Wells H., Williams K., Wood N., Allen T., Bushell A., Copsey D., Earnshaw P., Edwards J., Gross M., Hardiman S., Harris C., Heming J., Klingaman N., Levine R., Manners J., Martin G., Milton S., Mittermaier M., Morcrette C., Riddick T., Roberts M., Sanchez C., Selwood P., Stirling A. et al. 2017. The Met Office Unified Model Global Atmosphere 6.0/6.1 and JULES Global Land 6.0/6.1 configurations. *Geoscientific Model Development*, **10** (4): 1487-1520.

Wang Z. 2013. On the response of Southern Hemisphere subpolar gyres to climate change in coupled climate models. *Journal of Geophysical Research: Oceans*, **118** (3): 1070-1086.

Warnock J.P., Scherer R.P. & Konfirst M.A. 2015. A record of Pleistocene diatom preservation from the Amundsen Sea, West Antarctica with possible implications on silica leakage. *Marine Micropaleontology*, **117**: 40-46.

Weber M.E., Clark P.U., Kuhn G., Timmermann A., Sprenk D., Gladstone R., Zhang X., Lohmann G., Menviel L., Chikamoto M.O., Friedrich T. & Ohlwein C. 2014. Millennial-scale variability in Antarctic ice-sheet discharge during the last deglaciation. *Nature*, **510** (7503): 134-138.

Weber M.E., Kuhn G., Sprenk D., Rolf C., Ohlwein C. & Ricken W. 2012. Dust transport from Patagonia to Antarctica – A new stratigraphic approach from the Scotia Sea and its implications for the last glacial cycle. *Quaternary Science Reviews*, **36**: 177-188.

Weber M.E., Niessen F., Kuhn G. & Wiedicke M. 1997. Calibration and application of marine sedimentary physical properties using a multi-sensor core logger. *Marine Geology*, **136**: 151-172.

Williams T.J. 2018. Investigating the circulation of Southern Ocean deep water masses over the last 1.5 million years by geochemical fingerprinting of marine sediments. PhD thesis: *Department of Earth Sciences, University of Cambridge.*

Williams T.J., Martin E.E., Sikes E., Starr A., Umling N.E. & Glaubke R. 2021. Neodymium isotope evidence for coupled Southern Ocean circulation and Antarctic climate throughout the last 118,000 years. *Quaternary Science Reviews*, **260**: 106915.

Wilson D.J., Bertram R.A., Needham E.F., van de Flierdt T., Welsh K.J., McKay R.M., Mazumder A., Riesselman C.R., Jimenez-Espejo F.J. & Escutia C. 2018. Ice loss from the East Antarctic Ice Sheet during late Pleistocene interglacials. *Nature*, **561** (7723): 383-386.

Wolff E.W., Fischer H., Fundel F., Ruth U., Twarloh B., Littot G.C., Mulvaney R., Rothlisberger R., de Angelis M., Boutron C.F., Hansson M., Jonsell U., Hutterli M.A., Lambert F., Kaufmann P., Stauffer B., Stocker T.F., Steffensen J.P., Bigler M., Siggaard-Andersen M.L., Udisti R., Becagli S., Castellano E., Severi M., Wagenbach D., Barbante C., Gabrielli P. & Gaspari V. 2006. Southern Ocean sea-ice extent, productivity and iron flux over the past eight glacial cycles. *Nature*, **440** (7083): 491-496.

Xiao W., Esper O. & Gersonde R. 2016. Last Glacial - Holocene climate variability in the Atlantic sector of the Southern Ocean. *Quaternary Science Reviews*, **135**: 115-137.

Yin Q. & Berger A. 2015. Interglacial analogues of the Holocene and its natural near future. *Quaternary Science Reviews*, **120**: 28-46.

Zielinski U. 1993. *Quantitative estimation of palaeoenvironmental parameters of the Antarctic Surface Water in the Late Quaternary using transfer functions with diatoms*. Reports on Polar Research.

Zielinski U., Bianchi C., Gersonde R. & Kunz-Pirrung M. 2002. Last occurrence datums of the diatoms *Rouxia leventerae* and *Rouxia constricta*: indicators for marine isotope stages 6 and 8 in Southern Ocean sediments. *Marine Micropaleontology*, **46**: 127-137.

Zielinski U. & Gersonde R. 1997. Diatom distribution in Southern Ocean surface sediments (Atlantic sector): Implications for paleoenvironmental reconstructions. *Palaeogeography, Palaeoclimatology, Palaeoecology*, **129**: 213-250.

Zielinski U., Gersonde R., Sieger R. & Futterer D. 1998. Quaternary surface water temperature estimations: Calibration of a diatom transfer function for the Southern Ocean. *Paleoceanography*, **13** (4): 365-383.

Zwally H.J., Comiso J.C., Parkinson C.L., Cavalieri D.J. & Gloersen P. 2002. Variability of Antarctic sea ice 1979–1998. *Journal of Geophysical Research*, **107** (C5): 3041.